R-99-73

Simulations of the Scandinavian ice sheet and its subsurface conditions

G S Boulton, P Caban, N Hulton

Department of Geology and Geophysics
The University of Edinburgh

December 1999

ISSN 1402-3091
SKB Rapport R-99-73

Simulations of the Scandinavian ice sheet and its subsurface conditions

G S Boulton, P Caban and N Hulton

Department of Geology and Geophysics
The University of Edinburgh

December 1999

Abstract (English)

An ice sheet model has been applied to an approximate flow line through the area of the Fennoscandian ice sheet. The modelled ice sheet fluctuations have been matched with stratigraphic evidence of Weichselian ice sheet fluctuation in order to simulate ice sheet attributes through time along the flowline. The model predicts extensive melting at the base of the ice sheet. This output has been used as an input to a simplified model of hydrogeology along the southern flank of the ice sheet so as to reconstruct patterns of subglacial groundwater flow. The output from the model is also used to estimate patterns of subglacial stress and strain. Results suggest that large scale subglacial groundwater catchments are formed which were quite different in extent from modern catchments; that fossil subglacial groundwaters should be found at sampling depths; and much fracturing in shallow bedrock in Sweden could be glacially generated.

Abstract (Swedish)

En glaciationsmodell har upprättats för en approximativ isflödeslinje genom det område som har täckts av Fennoskandiska inlandsisar. Modellerade fluktuationer hos istäcket har passats mot stratigrafiska bevis för Weichsel-istidens fluktuationer för att härigenom simulera istäckets tidsberoende egenskaper längs flödeslinjen. Modellen förutsäger att omfattande smältning skedde vid istäckets botten. Dessa utdata har sedan använts som indata till en förenklad modell av hydrogeologin längs den södra flanken av istäcket för att rekonstruera mönstret hos det subglaciala grundvattenflödet. Utdata från glaciations-modellen används också för att uppskatta spänningar och töjningar under isen. Modell-resultaten visar sammanfattningsvis att storskaliga subglaciala inströmningsområden, vilka hade en helt annorlunda utbredning än moderna inströmningsområden, bör ha uppkommit. Vidare tyder resultaten på att fossilt subglacialt grundvatten bör finnas på de djup där vattenprov tas och att en del av den uppsprickning som observeras inom den övre delen av berggrunden i Sverige kan vara orsakad av glaciationen.

Summary

The report presents work done as part of a programme designed to simulate the physical conditions during the last glacial cycle in Sweden and, by developing models of past climate and environment, to devise means of testing (validating) simulations and to extrapolate tested behaviour into the future as a means of evaluating potential consequences for the safety of underground waste repositories.

An ice sheet model was developed as part of an earlier project in this programme. The model has now been simplified, improved, and rationalised. The improved model has been applied to a standard simulation flowline of an ice sheet in Sweden, along which it is used both in the forward mode, to explore the consequences for ice sheet development of different patterns of climatic forcing, and the inverse mode, in which we explore the climates compatible with a given glacier history. The most valuable simulations are inverse ones in which we examine the pattern of climatic change which causes a model ice sheet to fluctuate along the flowline in a way which is consistent with the geological evidence of ice sheet behaviour during the last glacial cycle. This inferred climatic drive is compared with independent records of climatic change through the last glacial cycle in Europe. It is found that the frequency of inferred change agrees well with the geological record, but that the amplitude of change required is greater than that suggested by the record. It is inferred that the greater amplitude of change over the ice sheet surface reflects a positive feedback over that surface, and that the frequency match gives strong support for the simulation.

Ultimately we hope to find geochemical evidence of past climatic impacts on groundwater changes at Äspö / Laxemar which will help to reconstruct the behaviour of the groundwater system over long time periods. The climatic impacts which may have been important may date from much longer than a single climatic cycle. As a result, we have developed a hindcast technique which permits us to back-extrapolate the climate of the last glacial cycle to 700 ka, by using correlations with Milankovitch forcing and the deep ocean record. These palaeoclimatic hindcasts are used to drive the ice sheet model along the transect through the last two climatic cycles.

The model has been applied to an approximate ice sheet flow line stretching from the western continental shelf of Norway, through western Sweden, southern Sweden and northern Germany into central Holland. It simulates ice sheet fluctuation in time and space along this flow line together with a variation of ice load, crustal deflection, basal temperature, basal and surface melt rates and the isotopic composition of melt water.

The ice sheet model is then used to drive a groundwater flow model along the standard transect through the last two glacial cycles. Groundwater fluxes, heads, trajectories are calculated, as are subglacial effective pressures. The important role of permafrost in influencing the pressure distribution is established.

This simulation is used to reconstruct the pattern of groundwater flow at Äspö / Laxemar, and suggest that glacial waters should be found at sampling depths, and demonstrate the potential importance of palaeohydrogeochemistry as a tool for establishing the long term behaviour of groundwater and the conductive properties of rocks.

The computation of water pressures beneath the ice sheet is a basis for computation of stresses and the resultant patterns of failure. It is concluded that hydrofracturing and shear fracture are likely to have been widespread beneath the ice sheet and that even intact granitic rocks could have been fractured beneath the divide zone. It demonstrates, however, that coupling must occur between ice sheet dynamics and permeability, which should clearly be an important subject for research in relation to the long term evolution of conductivity magnitude and geometry in Sweden.

Contents

1 Introduction

The programme of which this project forms a part is a collaborative exercise between the University of Edinburgh and Chalmers University of Technology. The programme has the following general objectives:

- to simulate the physical conditions during the last glacial cycle in Sweden by developing models of past climate and environment;
- to devise means of testing the simulation;
- to extrapolate the validated behaviour into the future as a means of evaluating potential futures which may impact on the safety of underground waste repositories;
- to publish the results in the open literature and expose them to peer review.

The Edinburgh components of this programme have been as follows:

1. Simulation of the last glacial cycle along a transect through Sweden and through the Äspö site.

   Reported as:

   - Boulton G S and Payne A, 1992a. Simulation of the European ice sheet through the last glacial cycle and the prediction of future glaciation. *SKB TR 93–14, 138 pp.*

   Published as:

   - Boulton G S and Payne A, 1992b. Reconstructing past and predicting future regional components of global change: the case of glaciation in Europe. In: *Waste Disposal and Geology*. International Geological Congress Proceedings Workshop 21, Tokyo, pp 51–134.
   - Boulton G S and Payne A, 1994. Northern hemisphere ice sheets through the last glacial cycle: glaciological and geological reconstructions. In: Duplessy J-C, and Spyridakis, (eds.) *Long-term climatic change: data and modelling*. Springer-Verlag, Stuttgart.

2. Investigation of the impact of glaciation on groundwater flow in Sweden and scoping calculations to establish the sensitivity of the system to different parameter values and to undertake validation tests.

Reported as:

- Boulton G S, Caban P and Punkari M, 1995. Sub-surface conditions produced by climate change, including glaciation: Project 2, Sensitivity tests and model testing. *SKB Arbetsrapport 95–42*.

Published as:

- Boulton G S, Slot T, Blessing K, Glasbergen P, Leijnse T and van Gijssel K, 1993. Deep circulation of groundwater in overpressured subglacial aquifers and its geological consequences. *Quaternary Science Reviews*, 12, 739–745.

Current project

To produce a complete time-dependent sequence of groundwater flux and pressure for the Äspö site through the last glacial cycle; to investigate the relation between glaciation and bedrock fracturing; to evaluate variations in the geochemistry of groundwater recharge produced during a glacial cycle as a preparation for possible hydrogeochemical testing; to simplify the ice sheet model.

Publications:

- Boulton G S, Hulton N and Vautravers M, 1995. Ice-sheet models as tools for palaeoclimatic analysis: the example of the European ice sheet through the last glacial cycle. *Annals of Glaciology*, 21, 103–110.

- Boulton G S, Caban P E and van Gijssel K, 1995. Groundwater flow beneath ice sheets: Part I – Large scale patterns. *Quaternary Science Reviews*, 14, 545–562.

- Boulton G S and Caban P E, 1995. Groundwater flow beneath ice sheets: Part II – Its impact on glacier tectonic structures and moraine formation. *Quaternary Science Reviews*, 14, 563–587.

2 Simplification of the ice sheet model

2.1 Introduction

The ice sheet model as originally developed /Boulton and Payne, 1992a, 1992b/ was a relatively complex research model and not accessible to users other than the originators. A flow-line model has been developed from this and the code simplified and rationalised in a way compatible with the sensitivity tests undertaken in Project 2. The following description is designed to give practical information about the operation of the simplified model rather than an in-depth discussion of the physics, numerical methods and software engineering employed, such as contained in Boulton and Payne /1992a/. A summary of the code is contained in the appendix.

2.2 Description of the model

Ice sheet modelling relies on being able to represent the physical state and thermo-mechanical properties of an ice sheet in numerical form. A schematic view of the ice sheet model is shown in Figure 2-1, and a diagram of the functional components of the model is given in Figure 2-2. An ice sheet consists of a large ice mass which flows because the ice deforms under its own weight. In this model we represent the ice sheet by ice surface and bedrock elevations at a given point in time. Ice temperature at set depths within the ice sheet is also calculated because the rate of ice deformation is itself dependent on ice temperature. Warm ice deforms more readily. We calculate what is happening in the ice sheet across a grid of regularly spaced points in the horizontal

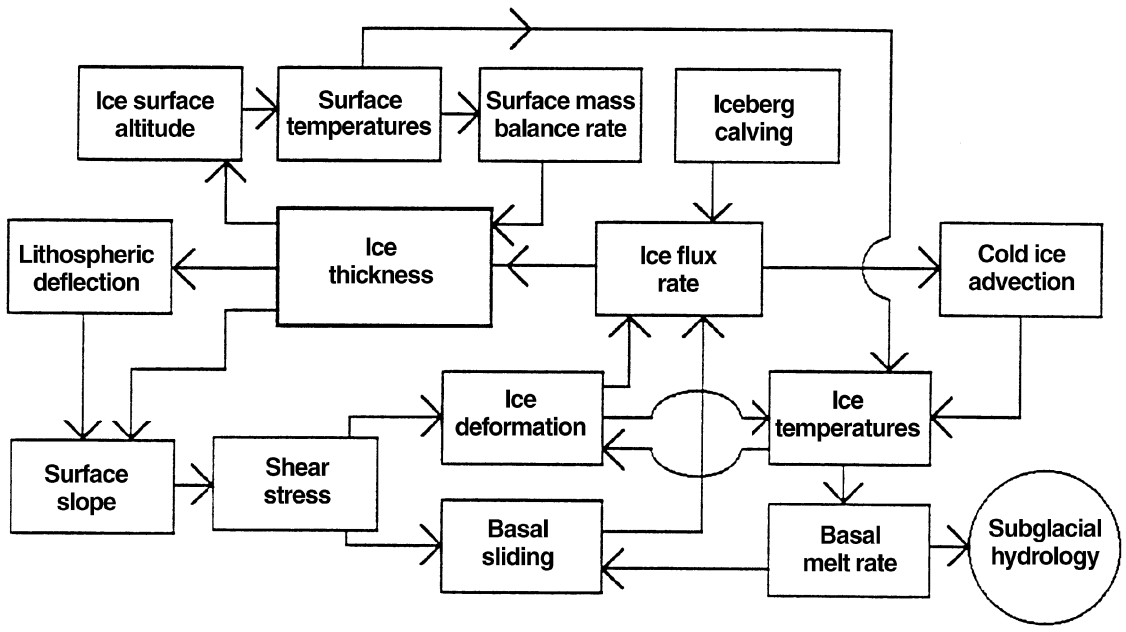

Figure 2-1. Scheme showing the way in which different components of the ice sheet system operate and which are simulated by the model.

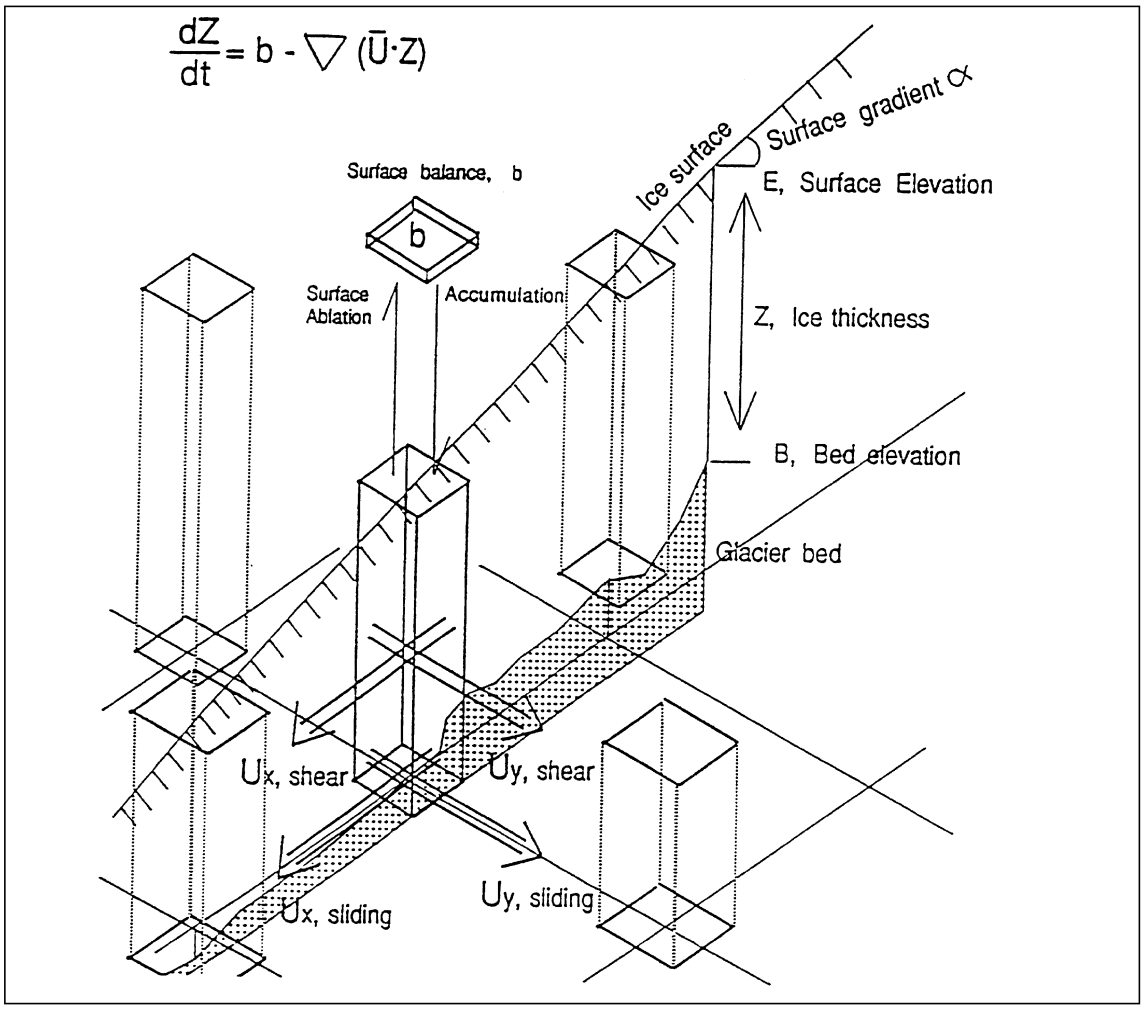

Figure 2-2. *Illustration showing the principal elements in the mass continuity balance for the ice sheet model along a flow line.*

(usually about 20 km). In the vertical the ice sheet is represented by ten ice layers, whose thicknesses vary but which are constant proportions of the total ice thickness at that point. The spacing of the points decreases with depth to resolve better the greater strain rates and temperature gradients towards the base of the ice sheet.

We simulate the evolution of the ice sheet by estimating for each represented point on the ice sheet, both the amount of snowfall or melt on the surface and also the amount of ice flowing to other areas. In other words, we apply a vertically integrated ice mass continuity equation to our modelled ice sheet of the form:

$$\frac{dZ}{dt} = \nabla \bar{u} Z + b \qquad 2.1$$

where: Z is ice thickness, t is time, $\bar{u}$ is the vertically averaged ice velocity and b is the external ice mass balance.

This equation is at the heart of the model. The distribution of ice mass exchange throughout the whole system provides the driving force for the ice sheet. Internal flow is the ice sheet's reaction to the changing pattern of external mass exchange. We calculate the separate external balance and flow components successively for discrete time steps (usually about 20 years). For each point, at each time step, any surface gains or losses are added to any gains or losses caused by ice flow to or from other points. A new surface elevation is calculated to take account of the total gain or loss of ice at that point at that time step. The model proceeds from time step to time step constantly updating the internal flow, external mass exchange and surface elevations. By this process the ice sheet dimensions and physical characteristics evolve over time. We will consider ice flow and external mass balance separately.

2.3 Ice flow calculations

Ice flow is calculated by applying the physics of ice deformation and, in some cases, a component which describes how much the ice is sliding at its bed. A discussion of the theory of ice flow is beyond the scope of this report but a good overview is provided by Paterson /1984/. Theory relating to ice deformation is well established both from experimental evidence and comparison of predicted rates of ice flow with measured rates on present-day ice sheets.

It is worth noting that a simple mechanical feedback helps to maintain the ice sheet form. The rate of ice flow is a non-linear function of ice thickness and the slope of the surface. Strain rates increase with steeper and thicker ice. The faster the ice flows, the more its thickness and gradient are reduced. A dynamic equilibrium between these two effects governs the ice sheet profile. The dependence of deformation on thickness tends to concentrate ice deformation towards the base of the ice sheet.

It is also important to note that the ice model forms a thermo-mechanically coupled system of the ice flow regime and the evolving temperature field within the ice. The temperature of the ice is determined by heat conduction from other regions within and at the boundaries of the ice sheet, heat advection from ice mass flowing between regions, and strain heating within the ice produced by the deformation process. This last heat source creates a positive feedback since faster flowing ice produces more heat and the consequent warming tends to make the ice deform more rapidly. This positive feedback is checked in part by the mechanical feedback previously described. However, it is also checked because cold ice tends to be advected from the surface into the centre of the ice sheet. This process accelerates if the ice flows more rapidly, thus cooling the ice sheet.

From the calculation of the temperature field we can calculate when and if the temperature of the ice rises sufficiently that melting will occur at the base of the ice sheet. Melting tends to occur here because pressures are greatest, which reduces the pressure melting point. In addition, most of the strain occurs here and the input of geothermal heat is largest. The model thus yields estimates of basal melt rate as output. The distribution of melting also controls the basal sliding regime. We assume that sliding will only occur if melt water is being produced. Sliding processes are in reality very complex but are known to be strongly dependent on the presence of water. If ice temperatures at the bed are below zero, the ice is rigidly frozen at the ice-bed interface and the ice only moves by deformation within the ice above. If water is present, it provides, in effect, a reduced friction layer that will decouple the ice from its bed, permitting it to slide. Theory gives us few clues about general relationships between sliding rates and other ice sheet properties. However, based on some theory and empirical evidence we assume the

sliding rate to be proportional to the ice thickness and the square of the ice sheet surface slope, but only allow it to occur if there is melting at the bed. The rate of sliding as a function of slope and thickness can be altered by the user. In certain cases we choose to allow no sliding at all. This allows us to experiment with the consequences of possible sliding situations in the absence of firmly based theory.

2.4 Driving the model with mass balance

Ice sheets will only be established if there is sufficient input of ice mass to the system. In reality this occurs if, over the long term, snowfall accumulation exceeds any melting or other loss of ice. We estimate the net balance of snowfall and melt as a single quantity, the net surface mass balance rate. This is assumed to be a simple function of the altitude of the ice sheet surface relative to a vertical position called the Equilibrium Line Altitude (ELA). This relationship is shown in Figure 2-3 and holds fairly well for real glaciers. The ELA is the notional altitude for any given sector of the glacier where the surface mass balance is zero. Below this altitude there is net negative surface balance, in other words there is more melting than snowfall over the course of year. Above the ELA, a net positive balance occurs when snowfall accumulation are greater than total melt. The slope of the mass balance curve with altitude is not constant. On real ice sheets it tends to be steeper in wetter-warmer climates and shallower in drier-colder ones. The steeper gradients in wetter areas reflect higher potential maximum snowfall rates combined with more rapidly increasing melt rates at lower elevations because of larger latent heat inputs compared with drier locations. The gradient of the mass balance altitude curve can be altered between model runs, but as yet must be held constant through a model run.

We define an initial ELA at each point in the model. In addition we define at each predetermined time step in the model a global ELA perturbation away from the starting values at each point. If the ELA is lowered this brings positive mass balance to lower elevations and causes the ice sheet to grow and the opposite if it is raised. By changing these ELA values through the model run we control its growth and evolution.

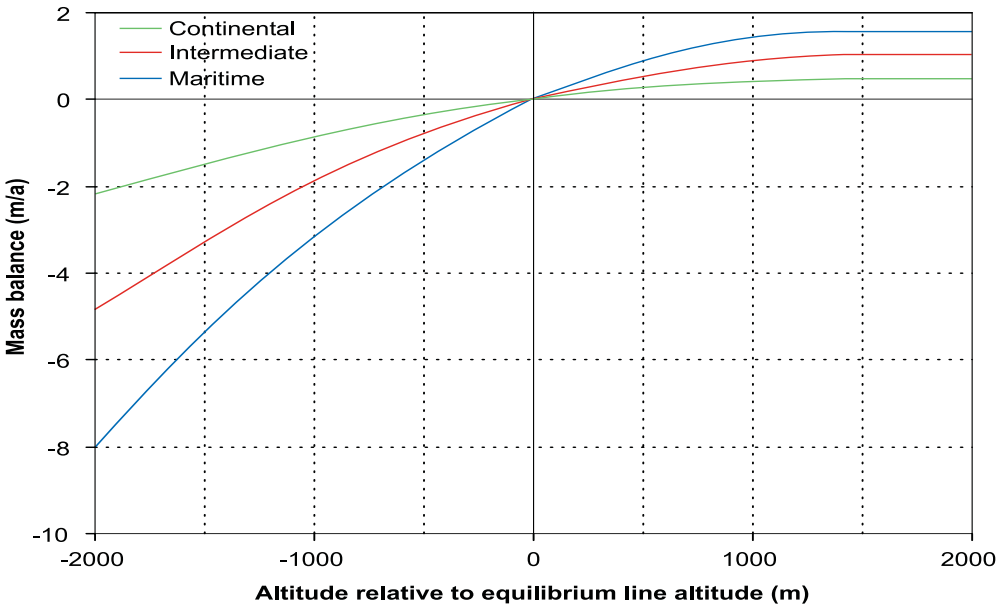

Figure 2-3. *Empirically-based mass-balance patterns used in simulations, showing continental and maritime extremes.*

We also define starting equivalent sea-level surface temperatures for each point in the model domain. These are extrapolated using a vertical lapse rate of 10°C/km to apply to the relevant surface altitude of the ice sheet. In the same manner as the ELA departures, we define global variations of sea-level temperature through time. Temperature and ELA are usually related when driving the model such that their concurrent changes are proportionally scaled.

2.5 Modelling along a flowline

We have produced some versions of the model in 3-dimensions but this document relates to an abstraction into a 2-D flowline model. The discussion above applies for both 2 or 3 dimensions. We make the initial assumption that by characterising a limited sector of the ice sheet this can provide us with sufficient information to extrapolate ideas regarding the nature of the entire ice sheet. If the ice flow direction does not change much through time then this is a reasonable first-order assumption. The simplified model can be used to explain the behaviour of the whole ice sheet. It represents the flow perpendicular to the ice surface contours and assumes that flow transverse to this direction will be minimal. The benefits of using the simplified model are that the computer resources and model return speed are significantly reduced allowing a greater variety of experiments to be performed. When the main interest is to examine the general dynamical characteristics of an ice sheet system, then this simplification is beneficial and justified.

2.6 Other calculations

Iceberg calving is estimated implicitly in the model by assuming that the ice is unable to progress beyond the 200 m bathymetric contour. This limits the expansion of the model over marine margins and is a reasonable assumption given that real ice sheets seldom extend into deep open water.

The model also calculates what bedrock adjustment, caused by the overlying weight of ice, takes place. We assume a perfectly elastic lithosphere which has no strength, and calculate its rate of response when subject to changing loading, based on the diffusivity of the underlying asthenosphere. The adjustment is always calculated from some assumed known 'relaxed' bedrock condition, usually taken to be the present-day ice free condition.

2.7 Model inputs

Inputs to the model are basal elevations and in some cases an existing ice sheet with its temperature field. The model also needs a description of the 'relaxed' bedrock condition in order to make the correct lithospheric adjustment calculations. The model needs a description of the ELA positions at each grid point along the transect. Two time series are needed, one of ELA variation and one of equivalent sea-level temperature variation. In addition, the model needs input for all the variables relating to the physical behaviour of the ice and bedrock adjustment. The model is described further in Appendix I.

2.8 Model outputs

The output of the model is selectable by the user. As a minimum the model produces output describing the basal and surface elevation of the ice sheet along the transect at specified time intervals. However, it can also produce values of the internal temperature,

basal temperature, basal melt rate and balance flux. In addition the model will record a number of integrated values for the whole ice sheet such as flowline length, total volume, melt rates and also the isotopic composition of the melt water.

3 Time dependent environmental sequence through the last glacial along the standard transect

3.1 Introduction

A reconstruction of palaeoenvironmental events in the Äspö / Laxemar region is necessary in order to understand the time-dependent loading to which the lithosphere is subjected, the recharge rate of groundwater, the chemistry of groundwater recharge and the time-dependent change of permeability.

In an earlier report /Boulton and Payne, 1992a/, a first simulation of glacial and permafrost events along a flowline transect from the western continental shelf of Norway, through western Sweden, through the Äspö / Laxemar area and into northern Germany and the Netherlands was constructed. The section of this transect from western Sweden is shown in Figure 3-1 (note that modelling is done in a longitudinal swathe so that it can

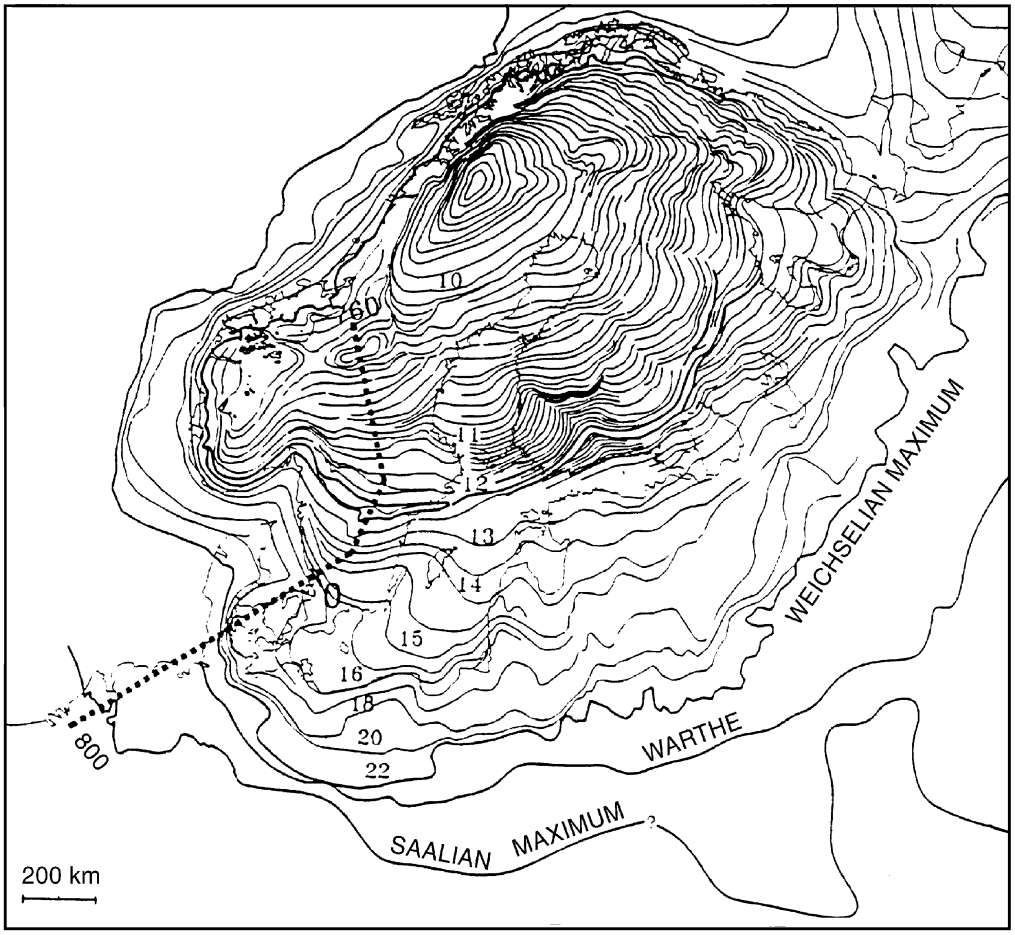

Figure 3-1. *European Ice Sheet margins for the Saalian maximum, the late Saalian, Warthe stage, the Weichselian maximum and the successive ice margins during retreat from the Weichselian maximum. Numbers on the isochrons for retreat refer to thousands of years before present in sidereal time. The dotted line shows the location of the transect along which modelling has been conducted, from -800 to 760 km.*

be applied to a three dimensional bed, Figure 3-1 shows the western boundary of the swathe.) It was accepted that this model probably overestimated ice thicknesses, did not simulate well the geological evidence of glacier fluctuation in the early part of the glacial cycle, and lagged the real glacial curve by about 5–10,000 years.

We have improved the model as indicated above, and the approach. We now have a more robust simulation of ice sheet events along the transect through the last glacial cycle.

3.2 Ice sheet / climate relations

We expect the long-term evolution of the landward margins of the Pleistocene mid-latitude ice sheets over Europe and North America to have been a reflection of climate change, whilst the marine margins may well have been strongly influenced by internal dynamics, at least on short timescales. Given the capacity of large, slowly varying ice sheets to buffer high frequency climate oscillations, we might expect fluctuations of the landward margins of ice sheets to be a smoothed, long term proxy record of atmospheric climate.

The response of ice sheets to climatic change is relatively complex, if only because of long ice sheet response times. It is difficult to use their patterns of fluctuation as a direct proxy for climate which can be readily compared with other palaeoclimate proxy data. However, numerical models of ice sheet dynamics are capable of simulating the response of ice sheets to climatic change, and it is therefore possible that they can be used to translate the geological evidence of ice sheet fluctuation into more useful indices of palaeoclimate. Conversely, it should be possible to use such models to investigate whether proxy climate sequences derived from other palaeoclimate indicators are compatible with evidence of contemporary ice sheet fluctuation. We therefore distinguish between a *forward approach* in which a climate change function is prescribed and the ice sheet response is computed, and an *inverse approach*, in which ice sheet behaviour is prescribed and the model is used to infer characteristics of the climate which could have driven the ice sheet. We then ask whether the inferred climate drive is compatible with contemporary palaeoclimatic records. If it is, we regard both the geological evidence and the model to have been relatively rigorously tested.

3.3 The climate drive

The climate drive for ice sheet fluctuation is provided by independent variation of temperature and mass balance. A prescribed variation in mean annual sea level air temperature (SLAT) is derived by assuming a linear correlation between this temperature and selected European and north eastern Atlantic palaeotemperature records for the glacial cycle /Boulton and Payne, 1992a, 1992b/. The vertical variation in air temperature is then derived from an assumed lapse rate of 10 °C km^{-1} /Orvig, 1970/, typical of rates over modern ice sheets. Sensitivity tests /Boulton, Caban and Punkari, 1995/ showed that ice sheet fluctuations were relatively insensitive to the absolute values of SLAT within reasonable limits suggested by palaeotemperature reconstructions, but they were sensitive to major departures of the lapse rate from modern values.

The vertical variation of mass balance, above and below the equilibrium line altitude (ELA) has a distinctive form in modern glaciers /Boulton and others, 1984/. We prescribe the form of the mass balance/altitude curve (Figure 2-3), which, for different model runs, vary between continental (low accumulation and ablation) and maritime conditions.

The model is forced by deviating the intercept of the ELA slope from the modern values. This alters the altitude at which local mass balance curves intersect the ice surface at each point along the transect. A linear correlation is assumed between and palaeotemperatures inferred from selected palaeoclimatic sequences through the last climatic cycle. Parallel variations in ELA and SLAT are therefore produced.

We have modelled along a transect through the area occupied by the European ice sheet during the last (Weichselian) glacial cycle, extending from the western continental shelf of Norway to northern Poland (Figure 3-1). This was an approximate flowline through much of the last glacial cycle, apart from during short episodes when Baltic ice streams crossed the transect.

3.4 Palaeoglacial and atmospheric palaeoclimate proxy records

We have summarised ice sheet fluctuation in Europe through the last glacial cycle by projecting Mangerud's reconstruction onto our line of transect (Figure 3-2). We recognise that the extent of decay between the glacial maxima is uncertain, the errors of dating may be significant, and that there is an implicit assumption that the most extensive glacial phases are contemporary with the isotopic peaks in the deep ocean isotopic record.

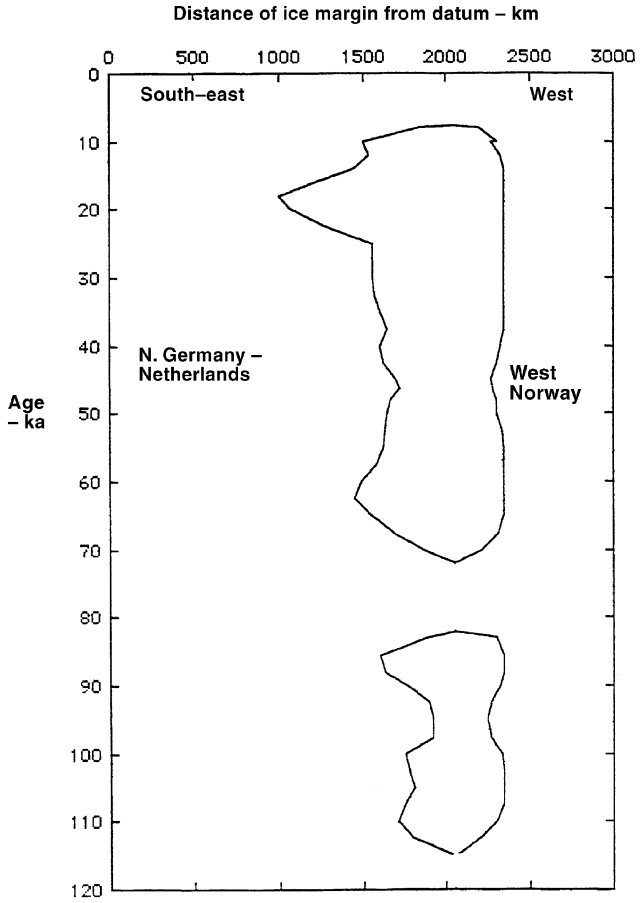

Figure 3-2. *Pattern of ice sheet fluctuation during the last, Weichselian, glacial cycle, constructed by projecting the geologically-inferred pattern of ice sheet fluctuation in Scandinavia by Mangerud /1991/ onto the transect.*

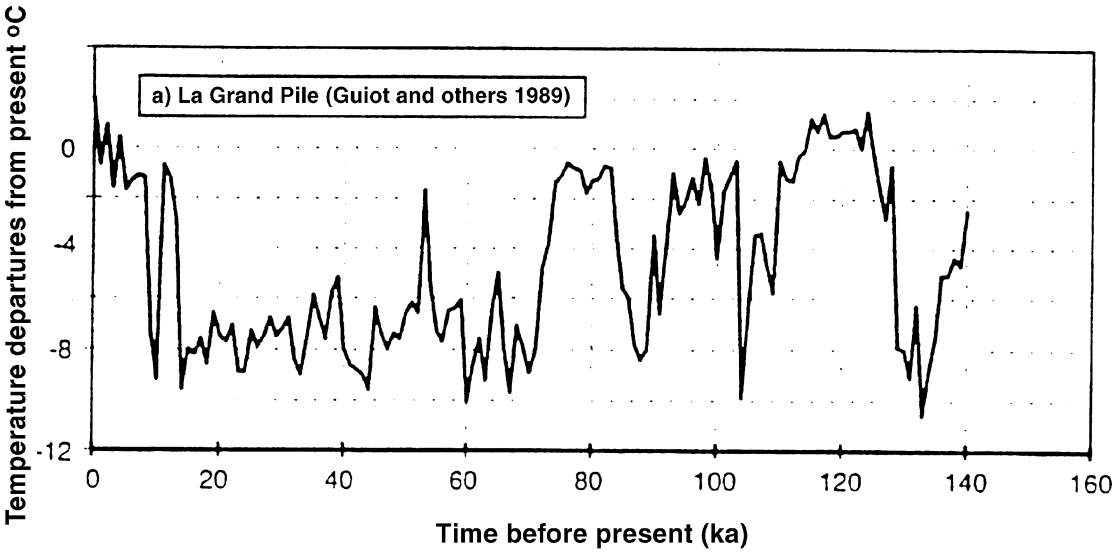

Figure 3-3. Palaeotemperatures inferred from the palynological record from La Grande Pile /Guiot and others, 1989/ for the last glacial cycle.

We have used two sources of information about atmospheric conditions in Europe through the last glacial cycle from the European area. Figure 3-3 shows palaeo-temperatures throughout the last glacial cycle from La Grande Pile in north-east France, inferred from a long pollen record /Guiot and others, 1989; Guiot, 1990/. Figure 3-4 shows a new sea surface temperature (SST) from core SU90-39 at latitude N52°30', longitude W22°0' in the Atlantic. A transfer function relating modern species distributions to sea surface temperatures estimates August SST's and is constructed using the modern analogue reference method /Prell, 1985/ from planktonic foraminifera /Labeyrie and others, 1987/.

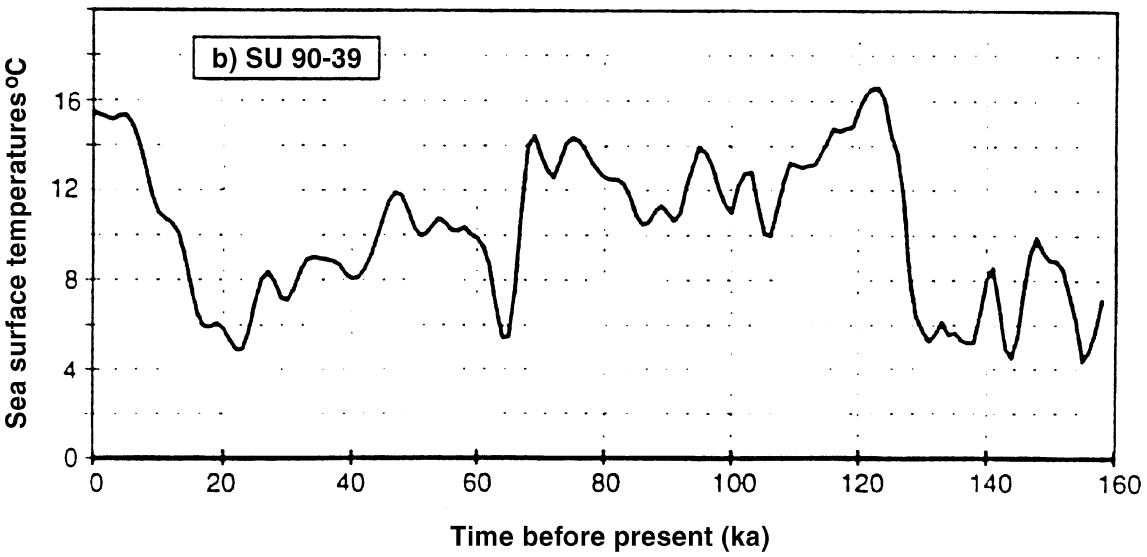

Figure 3-4. August sea-surface temperatures inferred from planktonic foraminifera in North Atlantic core SU90-39.

3.5 Forward experiments – the ice sheet response to a given climate series

We now test whether the pattern of ice sheet fluctuation in Europe through the last glacial cycle suggested by Mangerud /1991/ is compatible with contemporary terrestrial and marine palaeoclimate reconstructions.

It is assumed that ELA and SLAT for our ice sheet are linearly related to inferred palaeotemperature in each experiment, so that:

$$D\lambda = f_1 (T - f_2) \qquad (3.1)$$

where f_1 and f_2 are constants, $D\lambda$ is the change in ELA and T is the deviation from modern values of the independent palaeotemperature estimate. We have used a value of SLAT at the glacial maximum of approximately -10 °C, as suggested by the work of Frenzel et al /1992/ for the area of north-western Europe adjacent to the ice sheet margin, although the model is relatively insensitive to the precise value. The proportionality constant (f_1) in the ELA/palaeotemperature relationship is chosen as one which will drive the ice sheet as far as the maximum observed glacial extent along our transect at the time of the last glacial maximum (LGM).

3.5.1 Forward simulations driven by Atlantic SST reconstructions

In the initial simulation we assume that sliding does not occur at the ice/bed interface, even though the bed may be at the melting point. Values of $f_1 = f_1 a = 88.4$ m °C^{-1} and $f_2 = 15.5$ °C were used. This produces a maximum ice thickness along the transect at the LGM of about 3.4 km and a surface elevation of over 2.5 km. The profile along the transect of the ice sheet surface and isostatically-depressed bed, together with the internal temperature distribution is shown in Figure 3-5. The coldest temperatures lie in an enclosed area beneath the divide because the ice sheet continues to grow after the temperature minimum.

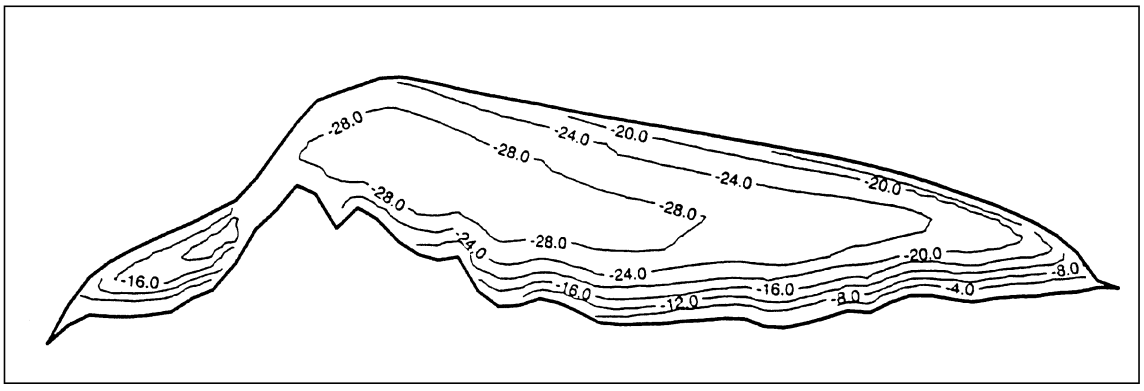

Figure 3-5. *Ice sheet profile along the transect from the western continental shelf of Norway to northern Germany during the last glacial maximum. The simulation is generated by using a north Atlantic sea-surface temperature as a driving signal. It shows the internal temperature distribution. The completely enclosed low-temperature ice mass beneath the ice divide is a reflection of the fact that the ice sheet growth continued for some time after the start of climatic warming following the coldest part of the glacial period. The Scandinavian mountain mass is shown beneath and just to the left of the ice divide. The bed shows isostatic flecturing.*

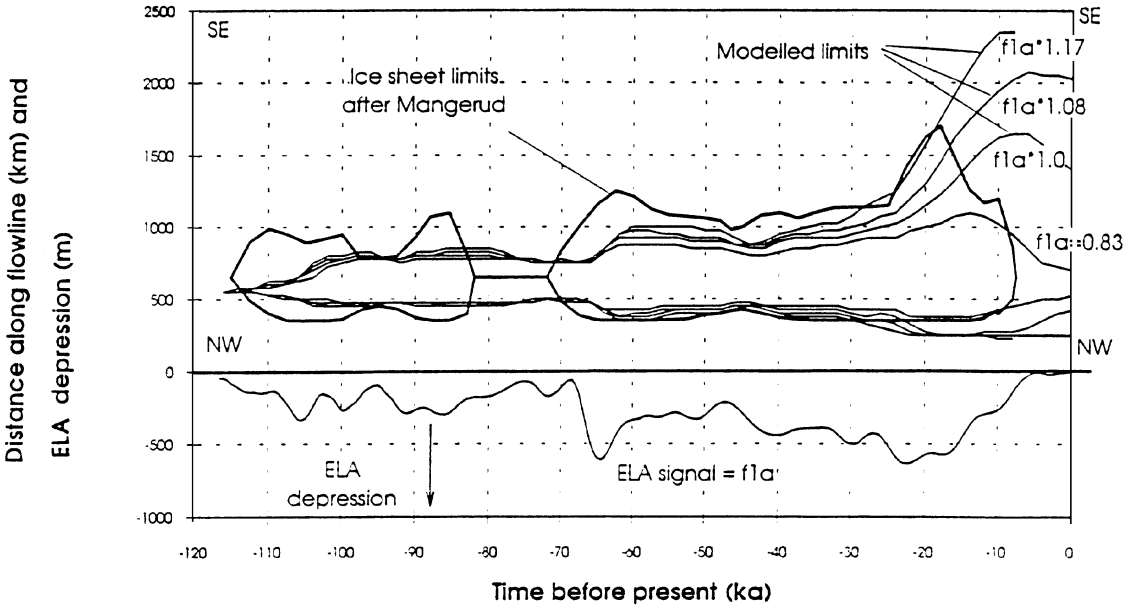

Figure 3-6. *Evolution of the European ice sheet along the transect during the last glacial cycle when forced by an ELA signal derived from a north-east Atlantic sea surface temperature model. The upper part of the diagram shows the time-dependent location of the ice sheet margin along the transect (plotted on the vertical axis), from western Norway at the bottom to northern Germany at the top. The horizontal axis shows time before present in 1000s of years. The heavy line shows the geological evidence of ice sheet fluctuation along the transect inferred from the reconstruction of Mangerud and the lighter lines show model simulations. The lower diagram shows the inferred ELA signal. In this simulation, no sliding is permitted to occur at the ice sheet bed.*

The time-dependent simulation of ice sheet margin fluctuation is shown in Figure 3-6, and compared with the geological reconstruction. The simulated ice sheet has not responded to the assumed climatic forcing as rapidly as the real ice sheet appears to have done; the simulated glacial maxima show large lags, it shows little or no retreat during periods of interstadial warming, and it fails to decay completely during the Holocene. These features are relatively insensitive to variations from maritime to more continental conditions.

Further simulations were then driven by values of f_1 0.83, 1.08 and 1.17 times the first simulation. The results (Figure 3-6), when f_1 is 0.83 times larger, are essentially similar to the previous simulations, but a small glacial peak is achieved at about 60 ka in response to the strong forcing peak at 68 ka. The analogous peak in the earlier simulation was just after 40 ka. There is then a long phase of reduced ice extent before the simulated build up at about 30 ka. It is clear that the position of the simulated margin at about 30 ka is very sensitive to small increases in forcing. The eventual LGM peak falls short of the real glacial maximum extent at some 10 ka after the geological evidence suggests that it occurred.

The simulations in Figure 3-6 for the larger values of f_1 show a more rapid response to the LGM forcing, but overshoot the glacial maximum position. The prescribed mass-balance altitude feedback is sufficiently strong with this level of forcing that once the modelled ice sheet reaches a critical size its growth is unchecked. The model halts when the domain size is exceeded. Again, none of the simulations succeed in causing the ice sheet to disappear completely during the Holocene.

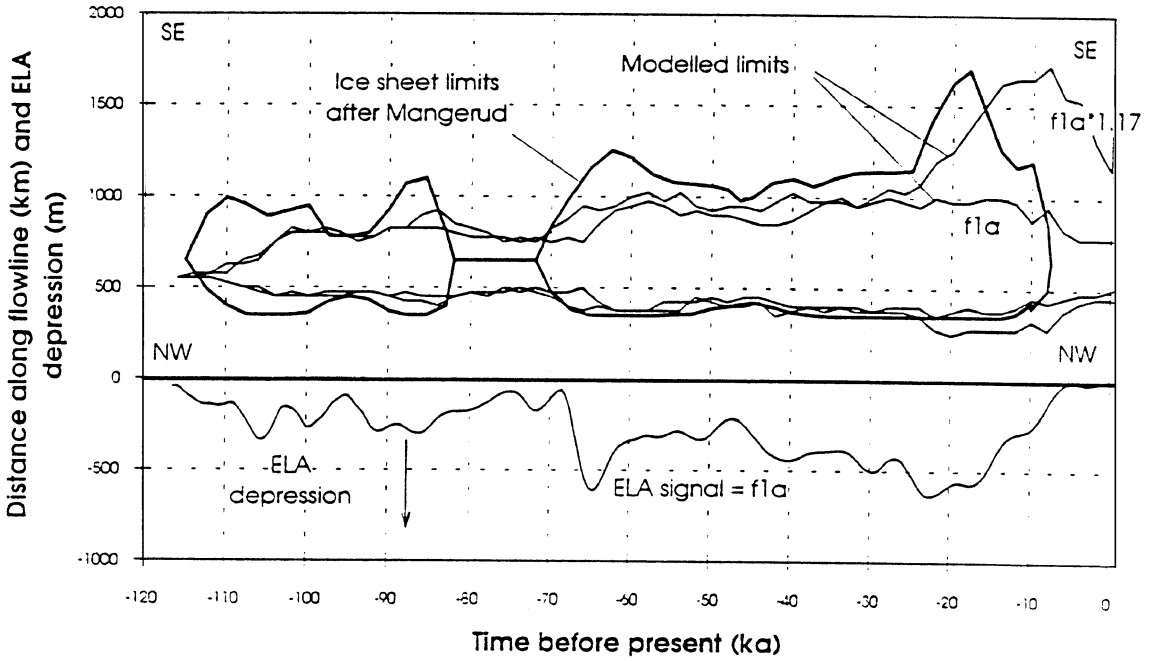

Figure 3-7. *A simulation similar to that of Figure 3-6 but in which sliding is permitted when the ice bed interface is at the melting point.*

We have then introduced sliding at the ice/bed interface into the simulation. We prescribe a basal sliding velocity to be a linear function of the shear stress. Results are shown in Figure 3-7 for values of $f_1 = f_1a$ and $f_1 = f_1a \times 1.17$. The former value is that used to produce the non-sliding response in Figure 3-6. It generates a much smaller ice sheet and is less responsive to forcing. This is because the lower profile of an ice sheet with sliding generates a smaller mass balance compared with a lower slope, non-sliding ice sheet for the same ELA. Using a value of f_1 of 1.17 times larger, however, drives the ice sheet to simulate the LGM extent, but again with a lag of 10 ka. The subsequent retreat is greater than in the non-sliding case because of the lower surface profile.

3.5.2 Forward simulation driven by palaeotemperature reconstructions from Les Echets, France

This record is given as temperature departures from the present, we therefore use a value of $f_2 = 0.0$ to equate it with the other signals. We have initially used the same value of f_1 as in the first simulation (f_1a). Two extreme basal boundary conditions have been used. In one, no basal sliding occurs irrespective of basal temperature In the other, sliding occurs wherever the basal temperature is at the melting point. The sliding rate is maximised such that is the highest the ice sheet will support before the model tends to become unstable.

Figures 3-8, 3-9 show the simulated ice sheet response to ELA forcing based on the Grande Pile data for the no sliding condition and the most extreme value of the sliding parameter. The forcing signal produced when $f_1 = f_1a*1.08$ is the maximum the model will support before it simulates an unstable ice sheet. When using the initial value of $f_1 = f_1a$ a much reduced ice volume results.

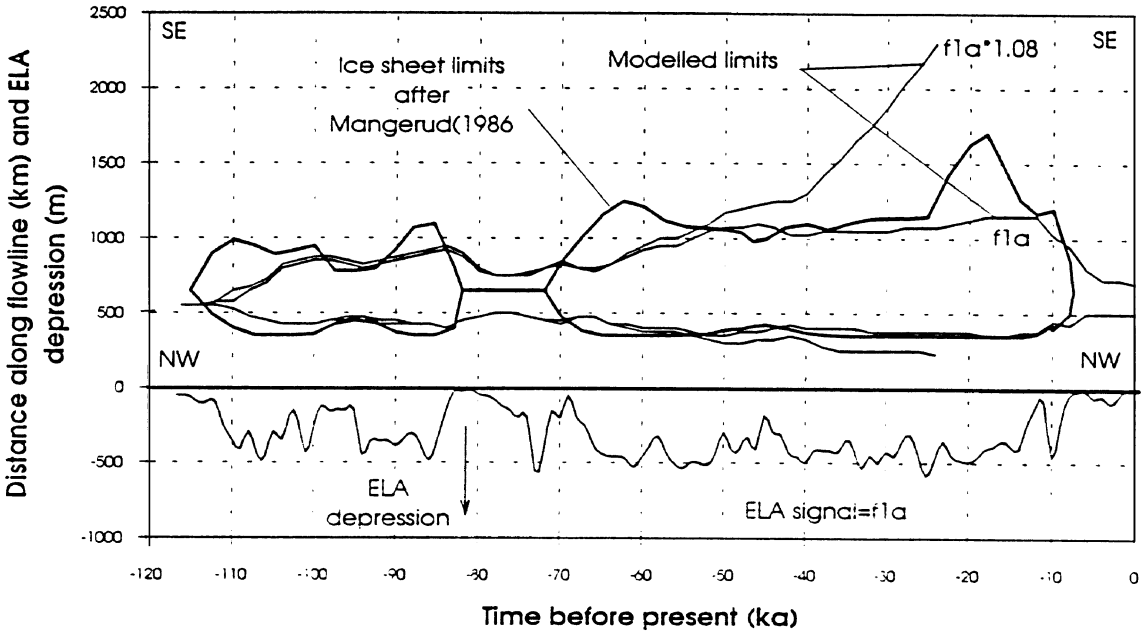

Figure 3-8. A simulation similar to those of Figures 3-6 and 3-7 but in which the ELA signal is derived from the Grande Pile palaeotemperature reconstruction /Guiot, 1990/. No sliding is permitted at the ice bed interface.

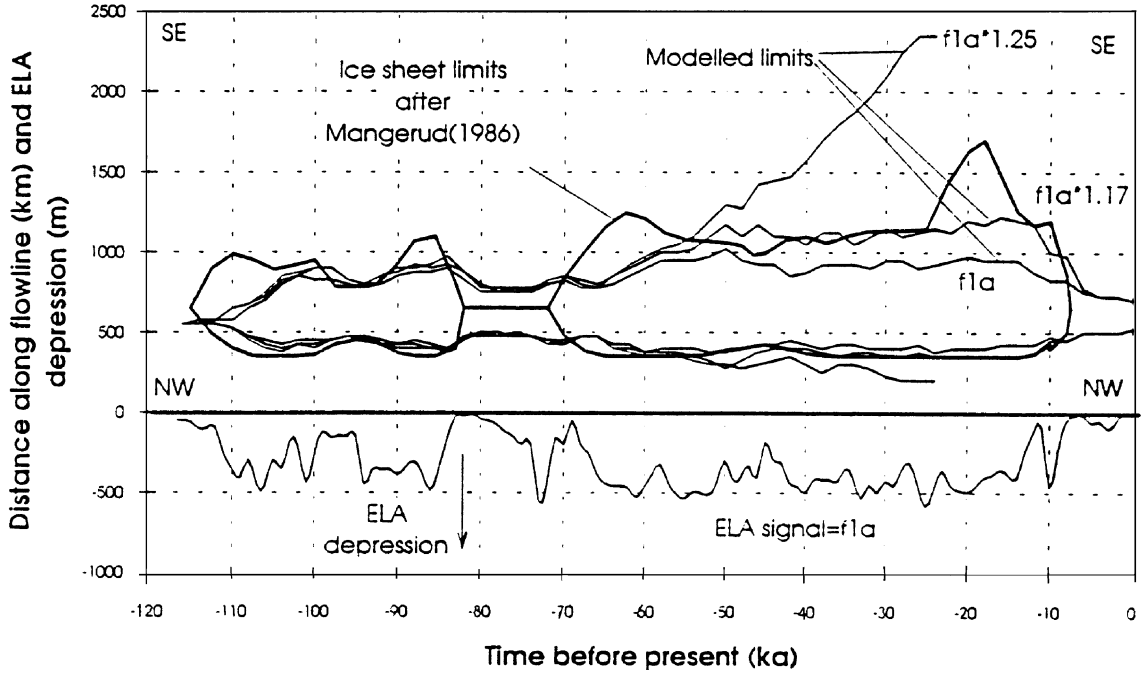

Figure 3-9. Simulation similar to Figure 3-8 but in which sliding is permitted to occur at the ice bed interface when the temperature rises to the melting point.

Figure 3-9 shows the response of the ice sheet to forcing when maximal basal sliding is included. With a value of $f_l = f_l a$, the ice sheet again remains relatively small and of roughly constant size through the glacial cycle. If f_l is increased to $f_l a*1.17$ (Figure 3-9) there is a relatively good fit to average size maintained by the ice sheet during the period 100–80 ka and 50–12 ka, although the peaks at 60 ka and 18 ka are not simulated. Moreover there is a substantial decay during the early Holocene. Even under conditions of the softest bed compatible with dynamic stability, the ice sheet does not decay as much as geological evidence suggests at 80 ka, and does not decay completely in the early part of the present interglacial. Moreover, there is not a sufficiently dramatic reduction in ELA at 70 ka to produce the 70–60 ka glacial maximum, nor after 30 ka to produce the LGM peak. Overall, although the Grande Pile temperature record between 115 ka and 85 ka produces a reasonable fit with the geological record, there is not sufficient variability in the forcing after 85 ka to reproduce the principle features of the ice sheet response to climate.

Our interim conclusion is that the greater variance in the SST records compared with the French pollen sites and the more differentiated forcing it produces are a better guide to the ice sheet surface climate required to generate the geological record of ice sheet fluctuation. None of these records, however, are able to generate a forcing able to destroy the ice sheets if we assume a linear relation between palaeotemperature records away from the ice sheets and ice sheet surface climate.

3.6 Inverse experiments to establish the climates compatible with a given pattern of ice sheet fluctuation

In these experiments, we have sought to establish, through the medium of the model, the nature of the ELA forcing functions which would be compatible with the geological evidence of ice sheet fluctuation. We have not employed a formal inverse technique, but have run multiple forward simulations so as to match the geological record.

We used both non-sliding and a maximally sliding models in these experiments. The match between model simulations and geological data together with the ELA forcings required to generate the simulations are shown in Figure 3-10 and 3-11. These ELA forcings and the ELA variations derived from palaeotemperature records are compared in Figure 3-12.

3.7 Conclusions

a) When the ice sheet model is driven by continental pollen palaeotemperatures, the ice sheet responds slowly to forcing and does not exhibit the strongly varying behaviour of Mangerud's geologically-based reconstruction. We suggest that this reflects greater climatic variance over the ice sheet than in extra-glacial areas. It is important to note, however, that although the amplitude of change required to make the ice sheet behaved as it did, the frequency of change required produces an ice sheet response in phase with the pollen record.

b) Early Holocene ELAs must have been significantly higher than modern values in order to produce complete deglaciation. The conventional view of Holocene palaeotemperatures /e.g. Mörner, 1980/ suggests a thermal optimum at about 6ka. However, a recent detailed reconstruction by Seret and others /1992/ suggests that the Holocene thermal optimum may indeed have been reached between 7 ka and 8 ka.

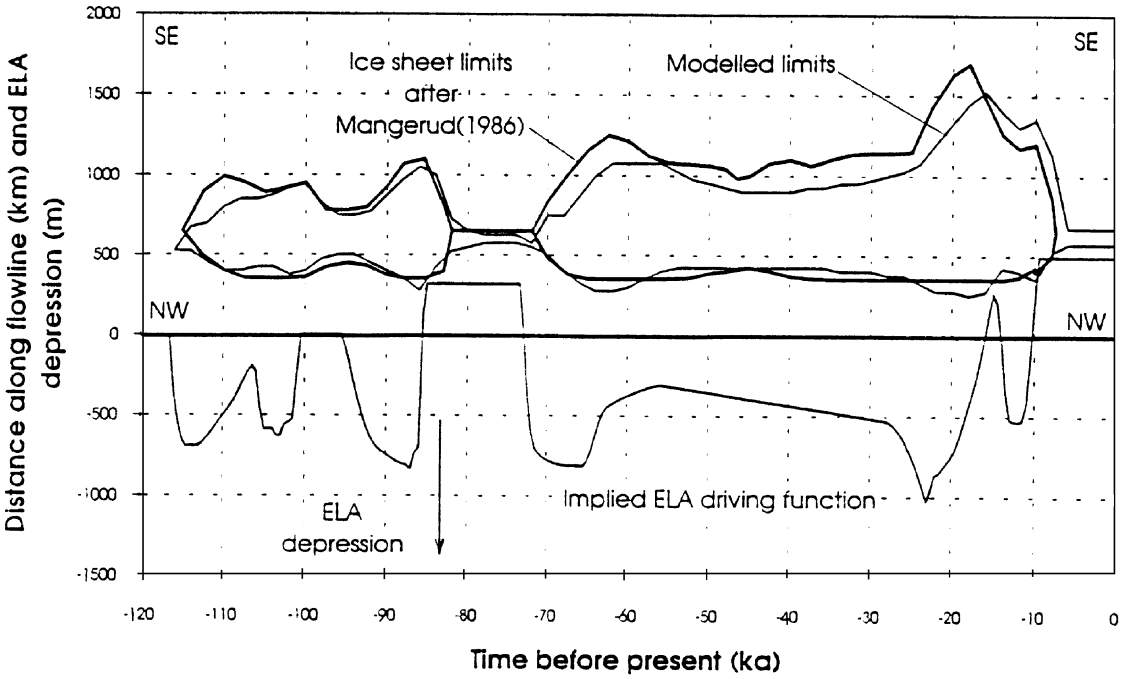

Figure 3-10. *Result of an inverse model in which the ELA fluctuation is inferred which is able to drive the model along the flow line transect such that the modelled ice sheet margins are similar to the geologically inferred margins. No sliding is permitted at the ice bed interface.*

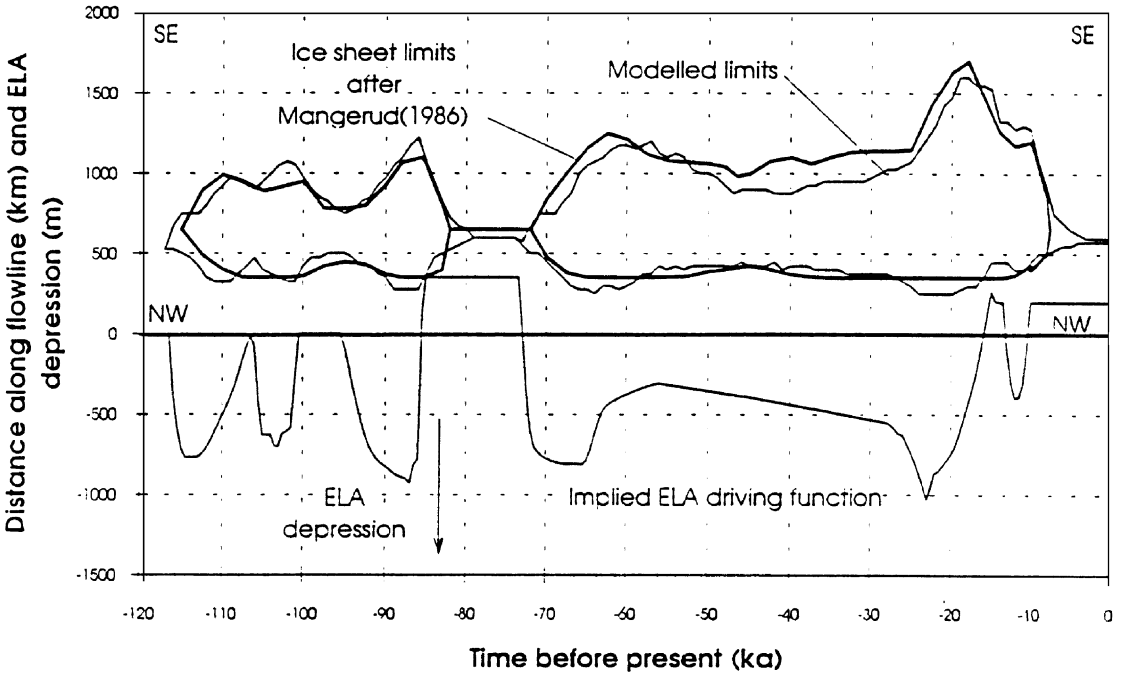

Figure 3-11. *Similar to the simulation of Figure 3-10 but in which sliding is permitted to occur at the ice bed interface when the temperature there rises to the melting point. Note the relative irregularity of the simulated ice margin compared with the non-sliding case. This reflects a dynamic instability produced by a sliding regime.*

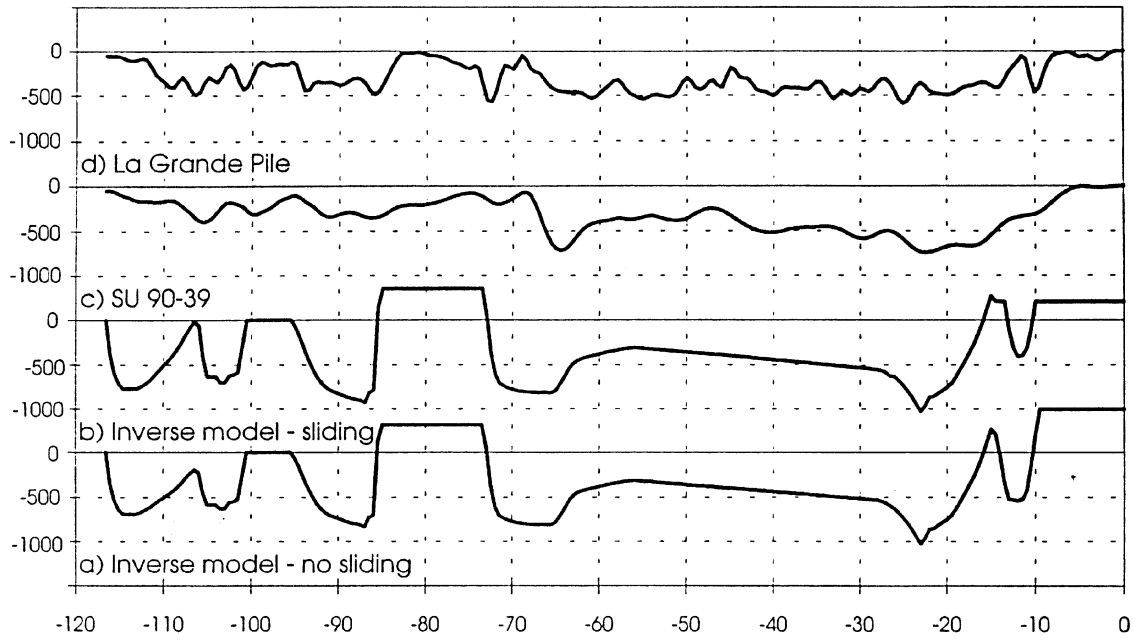

Figure 3-12. *ELA forcing used in various runs. The inverse signals (a and b) are those required to drive the model to achieve a reasonable match with the geological evidence. The others (c and d) are the ELAs used to drive the model derived by applying the temperature / ELA relationships to the palaeotemperature curves. In each case they show the ELAs used in no-sliding cases such that the ice sheet achieves a maximum size but does not become unstable. This means that each forcing signal produces a roughly comparable ice volume at maximum, but other features differ. The palaeo-signal from core SU 90-39 is much closer to the derived 'inverse' signals than the pollen record from La Grande Pile. Horizontal scale in thousands of years before present. Vertical scale is the ELA change (m) compared with present.*

c) The poor match in amplitude variation between simulations driven by palaeotemperature/ELA forcings and the geological record implies that the amplitude of temperature change beyond the ice sheet is much smaller than on the ice sheet surface and that there may be a non-linear relationship between ice sheet climate and extra-glacial climate. Such a non-linearity is likely to be derived from feedback processes between the ice sheet and atmosphere. However, the depleted continental faunas and floras of cold periods are probably much less effective as palaeoclimate indicators than those of warm periods. It may therefore be that extra-glacial climates were more severe than currently recognised.

d) The periods of strong deglaciation at 85–80 ka, 15 ka and 10–7 ka indicate anomalies between the glacial and palaeotemperature records. The glacial record requires an abrupt rise in the ELA to above modern values. It is possible that the 85–80 ka deglaciation could be explained by shifts in the three-dimensional geometry of the ice sheet which our two-dimensional simulation cannot match, rather than dramatic warming. The known geometry of the ice sheet after 15ka makes this unlikely for the two latter periods. It is possible that there was very strong warming at these times, which the inertia of oceanic and floral response failed to record. Indeed, palaeotemperature reconstructions by Coope /1977/ based on fossil coleoptera suggest that this is possible. The other possible explanation for these apparent anomalies is that the ice sheet underwent dynamically-driven collapse at these periods.

e) Ice sheet surface climate shifts must lead the glacial maxima by several 1000 years. Geological reconstructions in which the precise timing of glacial events is largely tuned by correlations with records elsewhere should take this into account.

f) Easy sliding does not produce high rates of ice sheet build up. Compared with a non-sliding ice sheet, easy sliding is associated with a lower ice sheet profile, which produces a smaller net positive mass balance and therefore a smaller build up rate. Stronger climate forcing is therefore needed to maintain the same rate of build-up for a sliding ice sheet. The converse occurs during decay, however. A lower profile gives rise to a greater negative mass balance, a greater rate of decay and an earlier final deglaciation.

g) The good match between the frequency of ELA change in the inverse model and the terrestrial record of palaeoclimate, is compatible with the geological record of ice sheet change and its simulation. We believe the amptitude contrasts to reflect positive feedback over ice sheet surfaces.

3.8 Up-dated model along the standard transect

The results of the inverse exercise carried out above are very satisfactory, and we now wish to replace the version of the glacial simulation along the transect derived by Boulton and Payne /1992a/ with these results, as a better estimate of transect conditions. The results are more fully represented in Figures 3-13–3-15 which show simulated ice sheet surface elevation, ice sheet thickness and ice sheet basal temperature in time and space along the transect through the last glacial cycle.

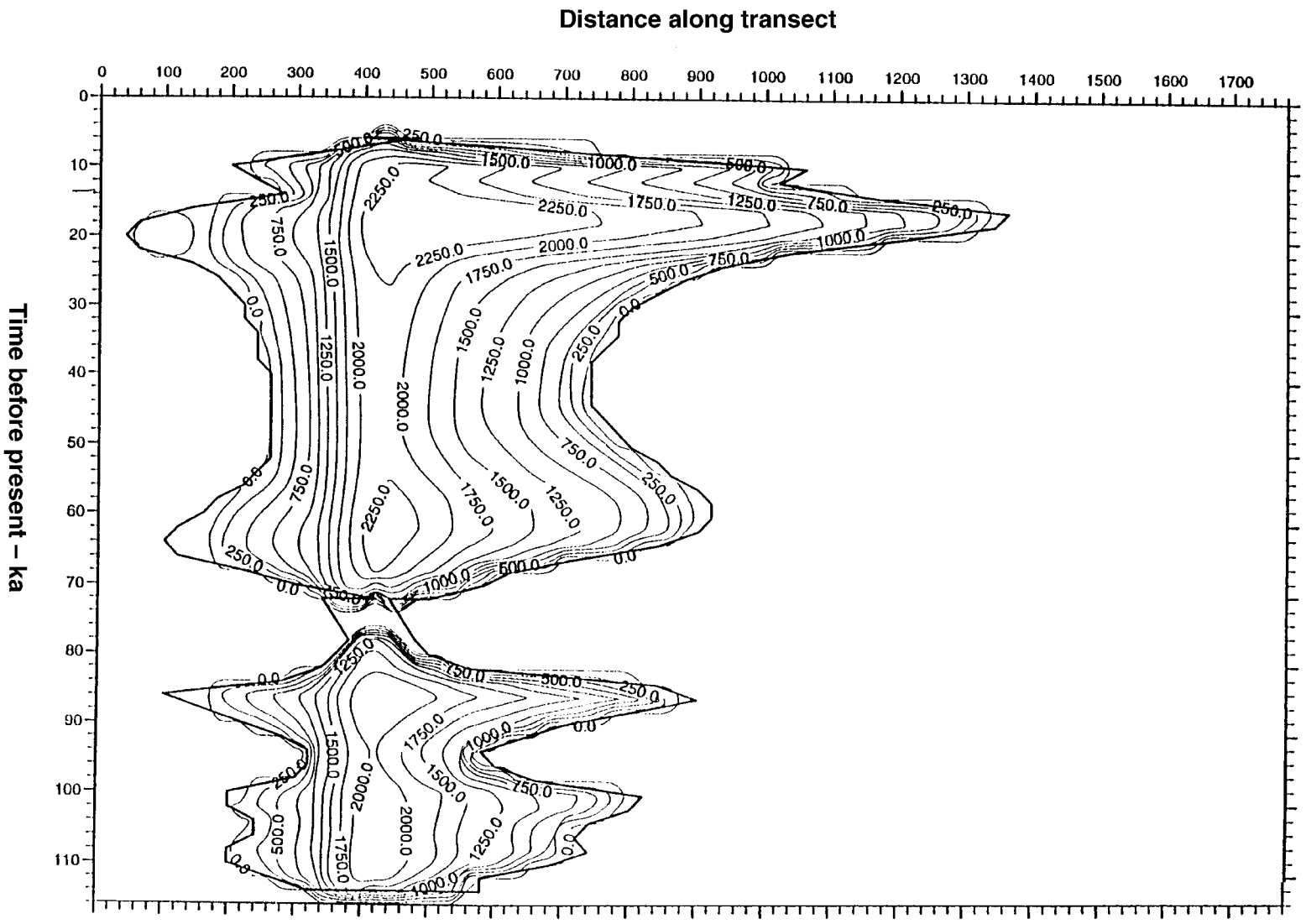

Figure 3-13. *Simulated surface elevation in metres above sea level of the western European ice sheet along the transect through the last glacial cycle derived from the inverse model. The horizontal scale shows a distance in kilometres along the transect from the western continental shelf of Norway to the left and northern Germany to the right. The vertical scale shows time in thousands of years before present. (Note that the contouring package for elevations produces smoothing contours beyond the maximum ice extent).*

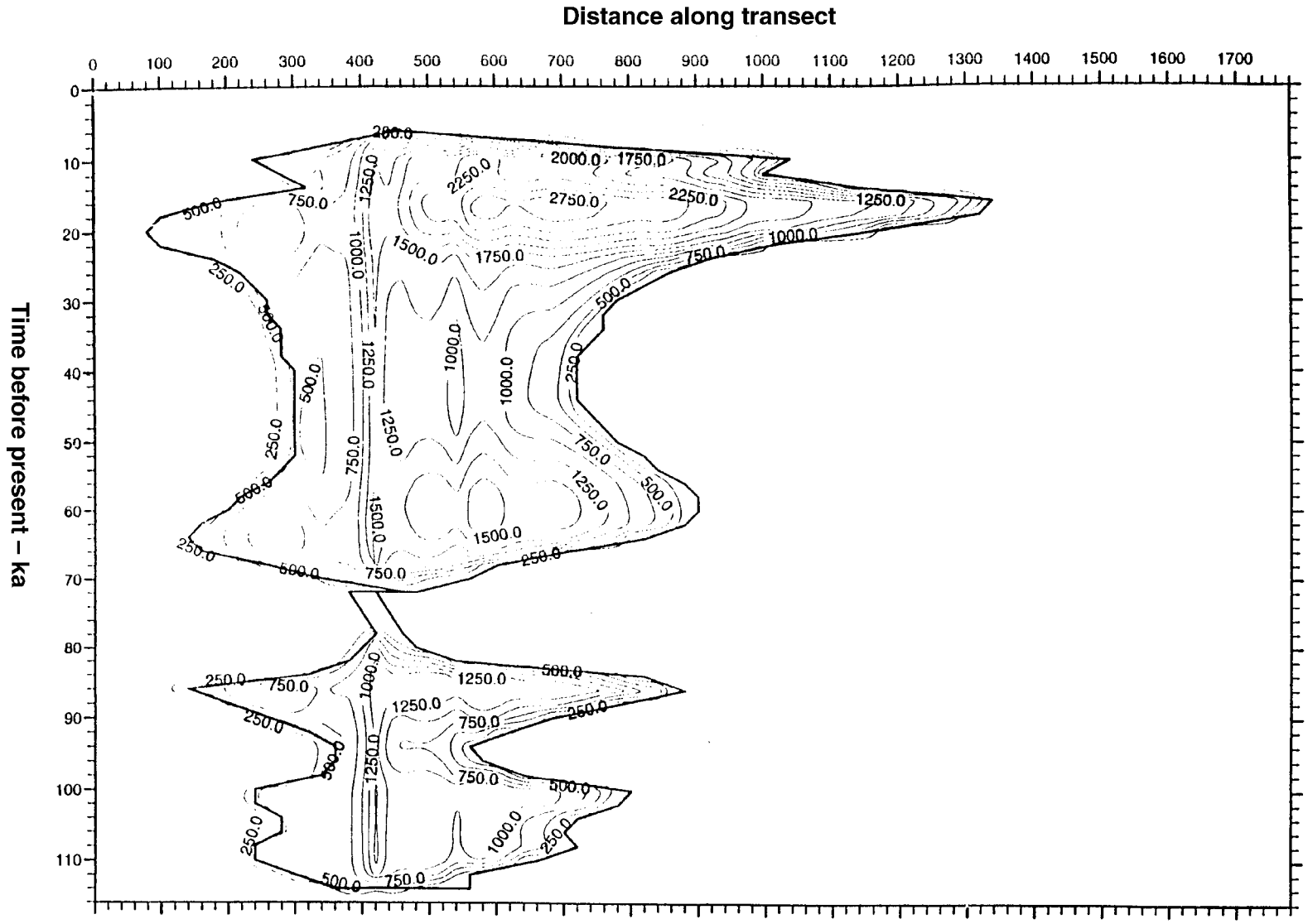

Figure 3-14. *As Figure 3-13, but showing the variation in ice sheet thickness in metres through the last glacial cycle.*

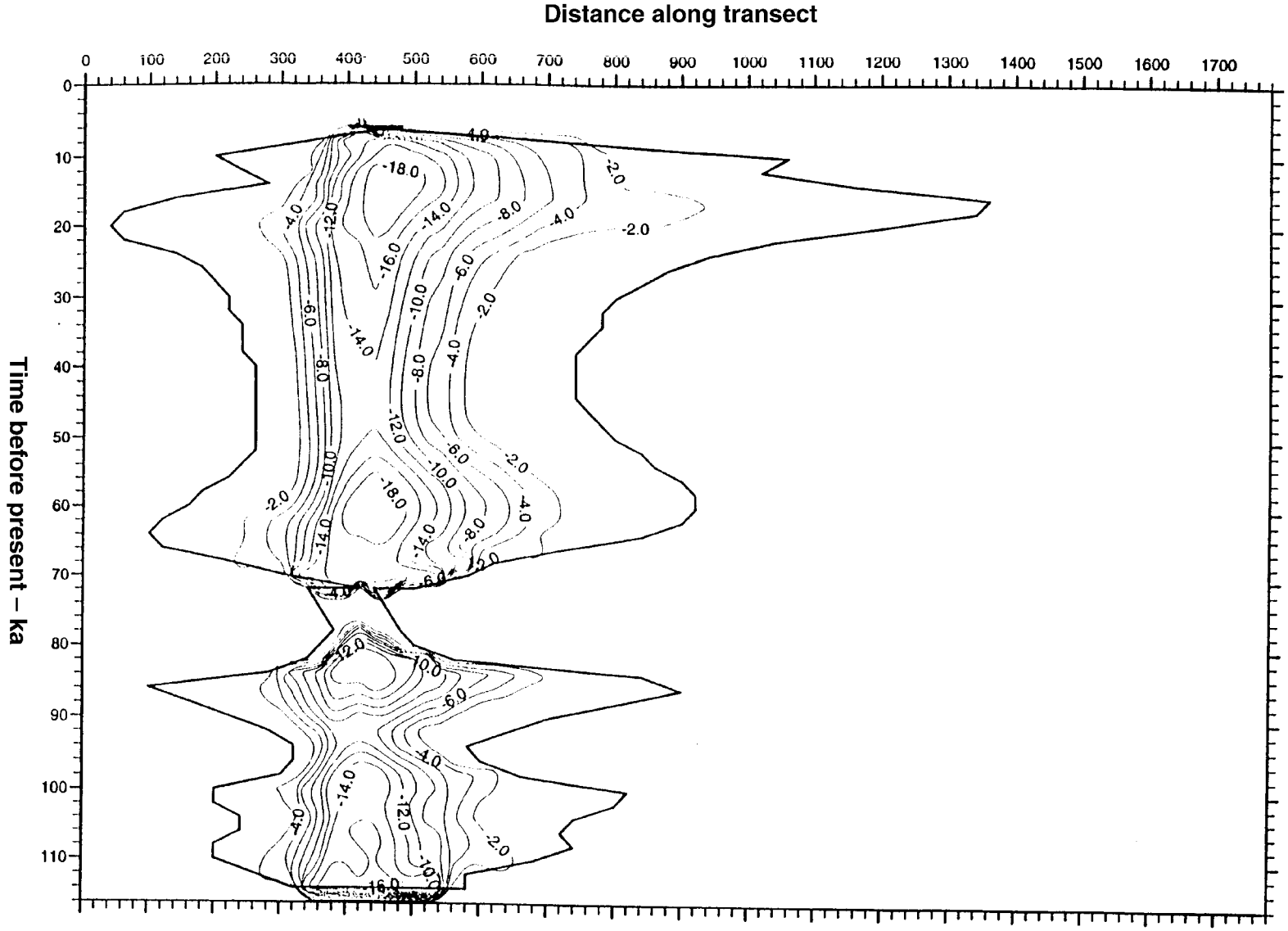

Figure 3-15. *As Figures 3-13 and 3-14, but showing the variation in basal temperature (°C) through the last glacial cycle. The ice sheet areas beyond the heavily contoured zones are zones of basal melting. The central zone of the ice sheet is largely a zone of basal freezing.*

4 Hindcasting climate records and extending the glacial simulation

4.1 Introduction

Simulation of the last glacial cycle may not give a long enough time frame within which to capture some of the significant climatic events which have had an important impact on groundwater flow at the Äspö / Laxemar site. Unfortunately, we do not yet have continuous records of terrestrial palaeoclimate in Europe beyond the last whole climatic cycle. We have, however, developed a technique whereby a simulated record can be developed beyond the last cycle.

4.2 An approach to hindcasting

Imbrie and others /1984/ (SPECMAP group) have generated a signal of global ice sheet fluctuation for the last 0.75Ma. Whilst no continental sequences in Europe have yet been found which cover a similar time-span, a number of Maar lakes reveal continuous pollen-rich sequences from at least the last 140,000 years. Guiot and others /Guiot and others, 1989, de Beaulieu and others, 1991, Guiot and others, 1992/ have developed transfer functions relating modern pollen distributions to climatic indices (temperature and precipitation) which have permitted them to reconstruct proxy climate records over this period for three Maar lake sites in central and eastern France: Lac du Bouchet, Les Echets and La Grande Pile.

We have used the pollen-derived temperature and precipitation records from these three sites to construct average, regional patterns of change which are smoother than site-specific patterns, and therefore easier to model. We then construct a linear correlation between the shorter continental records and the longer marine record using the Milankovitch theory that climate on timescales of 10^3–10^6 years is orbitally forced. The SPECMAP record and Earth's orbital variations /Berger and Loutre, 1991/ are system inputs and the European climate is the system output. By using the longer record in this way, as the spine for our prediction, we can produce reasonable linear hindcasts of the non-linear climate system.

The methodology for the hindcasts is based on a combination of the ACLIN /Kukla and others, 1981/ and INCLIN /Berger and others, 1981/ models. The three orbital variables, eccentricity, obliquity and precession /data from Berger and Loutre, 1991/ are modified according to the ACLIN model, and isolation included as in INCLIN. The three SPECMAP terms provide the general behaviour of the model and the hindcast. The seven regression variables are then as follows:

- x_1- Precession term: $\left|\frac{(\omega-180)}{90}\right|$ where (ω) is the longitude of the perihelion from the moving vernal equinox.
- x_2- Obliquity term (ε-22), lagged by 6 ka, where (ε) is the axial tilt.
- x_3- Eccenricity term ($e^{2)}$, where (e) is eccentricity.

x_4 - July insolation at 65°N (in Wm^{-2}).

x_5, x_6, x_7 - SPECMAP and SPECMAP lagged by 1000 and 2000 years.

A backwards elimination technique is used to eliminate unnecessary variables. It gives the following models:

Temperature = $1.13+0.258x_1+159x_2+0.125x_3-0.00394x_4-0.589x_5$

Precipitation = $6.79+0.32x_1+0.106x_3-0.0166x_4-1.94x_5+1.34x_6$

where temperature and precipitation are both in standard deviation units.

Both temperature and precipitation results are good, with R^2 values greater than 70%. The modelling technique produces estimates that are smoother than the actual data and do not capture short lived changes such as the Younger Dryas event. However, the transition between the penultimate glaciation and the last interglacial (isotope stages 6 and 5e of the deep ocean record), the sequence from the last interglacial through the early glacial (stages 5e–5a) and the end of the last glacial period are well captured. The main problem arises in the amplitudes of stages 5a–5d, where their relative magnitudes compared with the glacial maximum (stage 2) in the continental sites are larger than for the SPECMAP record. Although Les Echets shows a lesser temperature magnitude for 5a and 5c compared with 5e, they are all very similar in the Grande Pile and Lac du Bouchet sequences. In general, however, we are able to model the temperature and precipitation records of the last 140 ka very well.

4.3 Reconstruction of a 700 ka hindcast climate record for Europe

Having deduced the linear transformations between the French climate data and the SPECMAP / orbital variable combination for this period, we can now use the latter to hindcast the continental climate back to 700 ka. Figures 4-1 and 4-2 show the hindcasts of temperature and precipitation for the three sites separately. If we attempt to subdivide the curves, they can be described as showing peaks and troughs at a series of temperature levels, each one of which is associated with a particular level of precipitation. The colder the temperature the lower the precipitation. The temporal location and duration of the peaks and troughs and the precipitation levels associated with them are shown in Figure 4-2. We stress these hindcast peaks and troughs because the stratigraphic record can be very effective in demonstrating turning points in climate, represented by cold periods in otherwise warm phases or warm in cold phases /e.g. West, 1988/, and it is through these correlations that the hindcast reconstruction can prove a useful framework for a poorly dated stratigraphy. The amplitude of change in the hindcast reconstruction is constant through the last four cycles, back to 400 ka, but between 400 and 700 ka the amplitude is less. Although the depths of the cold troughs is maintained, the warm peaks appear to be very significantly cooler than subsequently, not rising above the thermal levels of stages 5a and 5c of the early part of the last climate cycle.

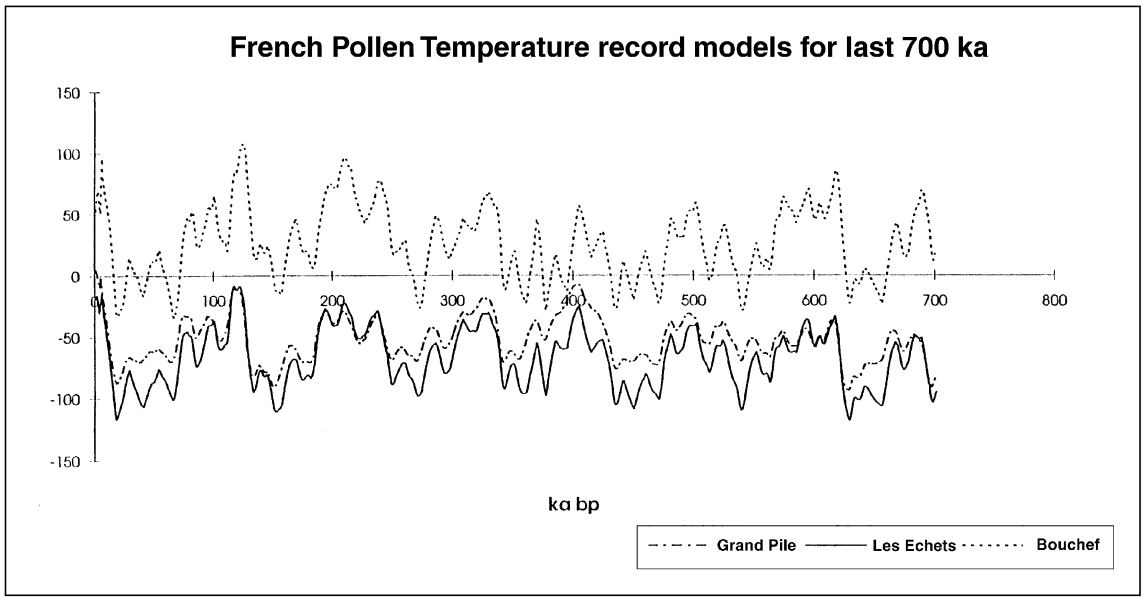

Figure 4-1. *Hindcast palaeotemperature curves based on the pollen-temperatures inferred by Guiot and others /1989/ from Grande Pile, Les Echets and Lac de Bouchet. The geological record extends through the last 120,000 years. The hindcast record extends to 700,000 years before present.*

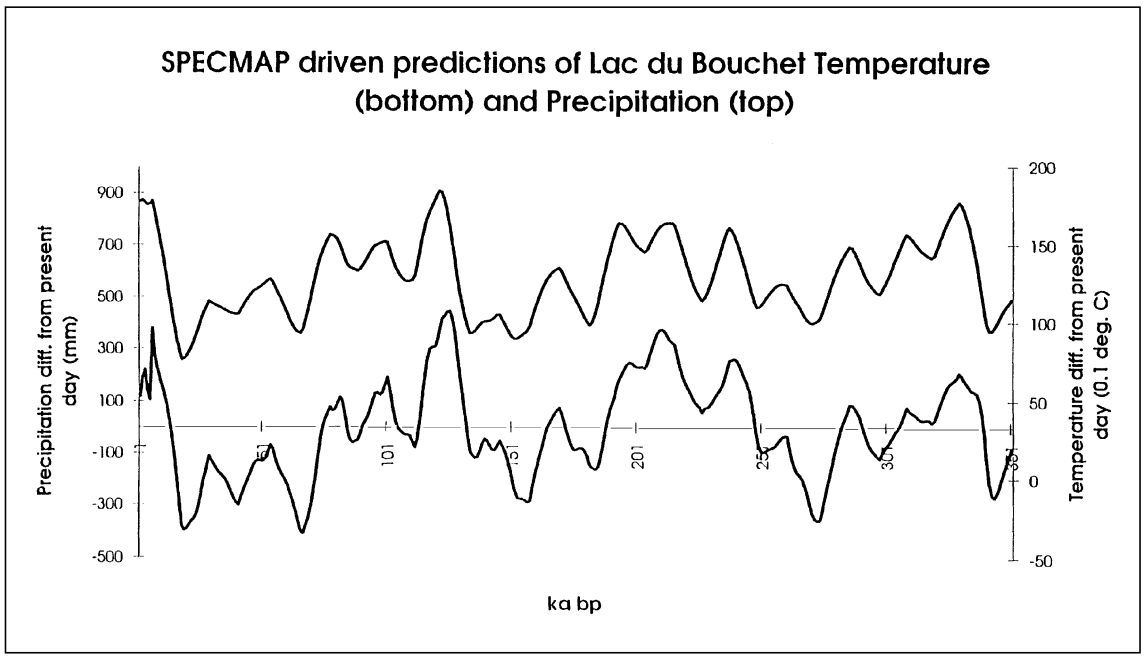

Figure 4-2. *Hindcast temperatures and precipitations derived from the Lac de Bouchet record.*

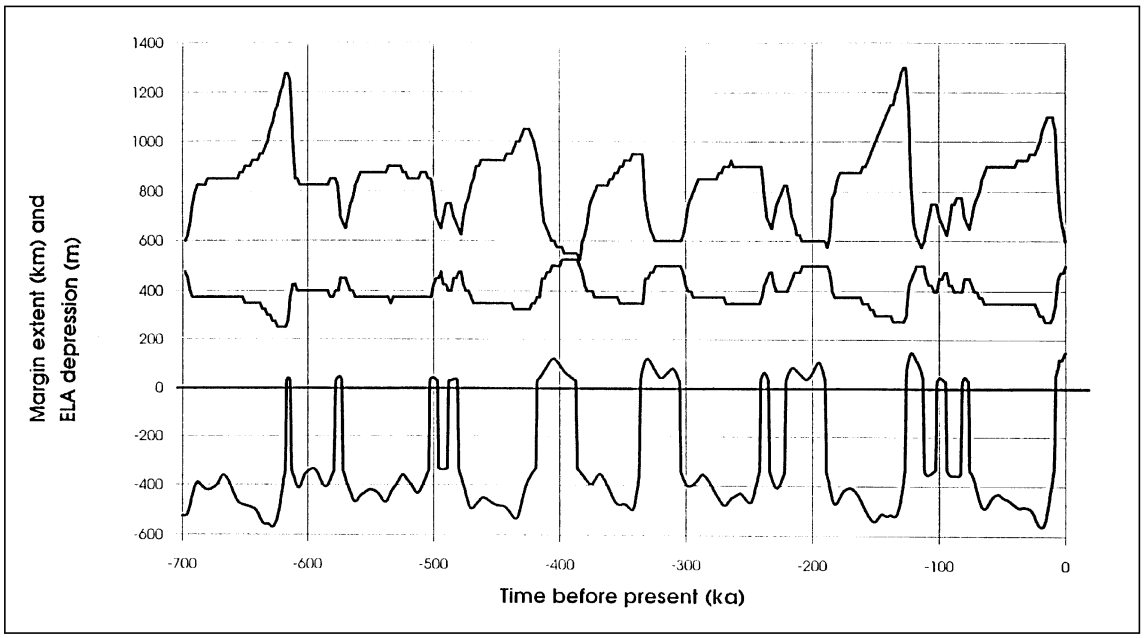

Figure 4-3. *The lower part of the diagram shows a hindcast of the change in ELA values compared with present values. The upper diagram shows the ice response which this would produce along the transect. It shows the simulated extent of the north-western (lower) and southern margins (upper) of the ice sheet through the last 700 ka. This simulation uses larger time steps, which accounts for the detailed discrepancies between this and the more detailed simulations shown in Figures 3-13–3-15 and 4-4.*

We can now use the correlation between climate and ELA from the inverse model of the last climatic to generate an ELA function and ice sheet response for earlier cycles (Figure 4-3). Figure 4-4 shows output from a relatively high resolution model for ice sheet extent and basal melting driven by the hindcast ELA record along the standard transect for the last two climate cycles.

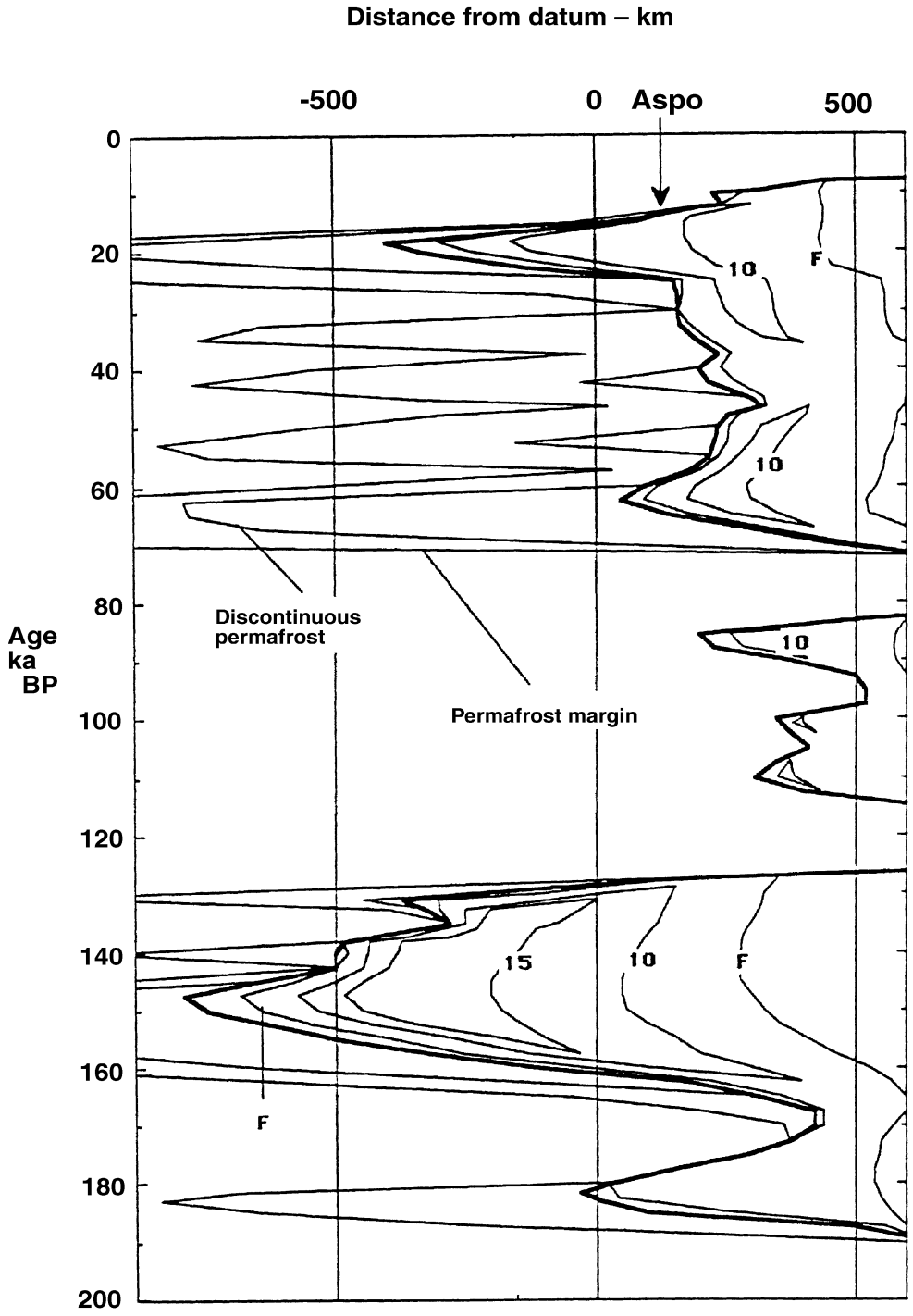

Figure 4-4. *Model fluctuation of the European ice sheet through the last two glacial cycles along the transect driven by the hindcast climate record. The heavy line shows the fluctuation of the southern margin of the European ice sheet in time and space from the Scandinavian ice divide, to the right, to the central Netherlands at the extreme left. Within the ice sheet area, contour lines showing melting rates are in millimetres per year. The contour marked 'F shows the areas within which the ice sheet is frozen to its bed. The simulation also shows the margin of permafrost. The relatively minor contrasts between this simulation and those shown in Figures 3-13–3-15 and 4-3 reflect differences in time steps and other scaling approximations. (Note that a different datum is used for this extended section along the transect shown in 3.1 and its transect to the SW).*

5 Large scale groundwater responses to ice sheet fluctuations through the last glacial cycle

5.1 Introduction

The development of a large scale groundwater model was introduced in Boulton et al /1995/. We now report on developments in the application of the model using the new ice sheet / climate sequence.

5.2 The groundwater flow model

Groundwater flow beneath ice sheets will be driven by two processes:

a) Consolidation of subglacial rocks due to the ice sheet load, resulting in the expulsion of water from the sediments and consequent groundwater flow. This will occur whether or not melting occurs at the ice sheet sole, but it is a transient feature. If a steady state ice sheet were resident for a long enough period of time, the underlying rocks would consolidate to equilibrium, and groundwater flow would cease.

b) Recharge of subglacial rocks by basal meltwater will generate a potential gradient and cause groundwater flow. Flow will continue as long as melting continues.

Here we restrict ourselves to analysis of the effect of meltwater recharge by assuming an incompressible aquifer matrix.

A finite-element model of Darcian groundwater flow /Sauter and others, 1990; Boulton and others, 1995/ has been used to examine the nature of the groundwater flow along the transect. This code permits us to examine two- or three-dimensional flow in steady or transient mode. For steady state flow in a saturated, rigid, porous medium, the total mass balance is given by:

$$\frac{\partial(n\rho)}{\partial t} + \nabla(\rho q) = \rho I \tag{5.1}$$

where n is porosity, ρ is density, t is time, q is discharge, ∇ is potential gradient and I is velocity.

For fluid of a constant density and a medium of constant porosity, this reduces to:

$$\nabla q = I \tag{5.2}$$

The momentum balance for a low velocity fluid, typical of groundwater motion (Darcy's law) is given by

$$q = -K\nabla h \tag{5.3}$$

where K is permeability.

This assumption ignores inertial effects associated with the flow, and will be valid providing that velocity and velocity variations are small, and has been used successfully by Hassanizadeh and Gray /1980/ and Bear and Verruit /1987/.

Substituting equation 2 into equation 3 yields

$$-\nabla K \nabla h = I \tag{5.4}$$

The equivalent equation for transient flow in an incompressible matrix is given by

$$S_s \frac{dh}{dt} = \nabla K \nabla h = I \tag{5.5}$$

where S_S is specific storage, defined as the volume of water that a unit volume of aquifer loses from storage as a result of a unit decline in hydraulic head.

Either of these two equations can be readily recast into finite-element form, and form the basis for the numerical modelling.

5.3 Hydrogeology of the transect

The transect has been chosen so that it lies approximately parallel to the principal ice flow directions during the Weichselian and Saalian glacial cycles, and hence that any glacially-driven groundwater flow is likely to have been parallel to the transect. We accept that this assumption is not true during interglacial periods. For example, present day groundwater flow is predominantly topographically driven, and hence perpendicular to the transect in the Netherlands /Glasbergen, 1990/. However, we argue that a glacially driven groundwater pulse will be the dominant feature in the groundwater signal, and that on the scale studied in this paper, flow lateral to the plane of the transect in response to conductivity anisotropy can be ignored.

The transect can be divided into two principal, geologically distinct provinces (Figure 5-1). To the north, the fractured Precambrian igneous and metamorphic rocks of the Fennoscandian Shield and, overlapping onto it in the south, a broad basin containing large Mesozoic and Cenozoic aquifers. The regional hydrogeology in both provinces has been greatly simplified to concentrate on the large scale pattern of glacially-driven groundwater flow. Groundwater flow in the northern, Scandinavian province is likely to occur predominantly along fissures. However, given the large scale on which we compute groundwater flows, a Darcian permeability can be as appropriate to a fissured, jointed rock mass as it is to a rock mass in which intergranular flow occurs, provided that large scale conductivity values can be obtained. Although the Darcian assumption inevitably produce small scale errors in predicting groundwater trajectories, we believe that bedrock transmissivities will be accurately reflected.

An analysis of hydraulic test data by Wallroth and Gustafson /1993/ is used as a means of producing a conductivity model along the transect across the Fennoscandian Shield. The analysis suggests that their hydrogeological properties can be approximated as a series of strata, with the hydraulic conductivity of each (K_i) given by an equation of the form /cf. Gustafson and others, 1989/:

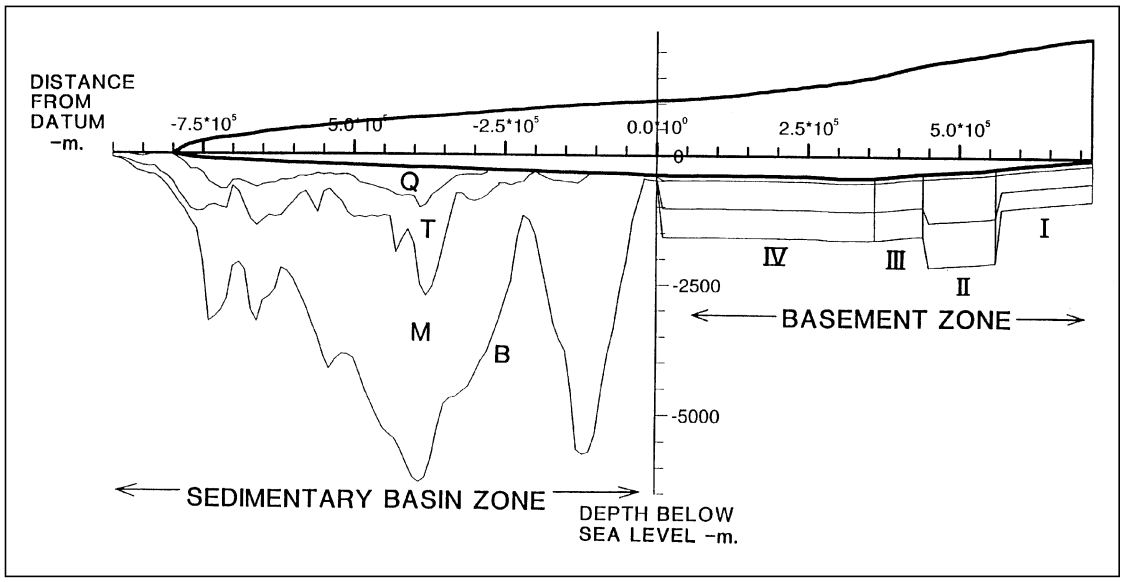

Figure 5-1. *Hydrogeology along the transect from the Scandinavian ice divide area to the central Netherlands. The hydrogeological units (I to IV) in the basement zone to the right have properties which are shown in Table 5-1. The basin zone to the left comprises an upper, Quaternary, aquifer (marked Q); a Tertiary aquitard (marked T); and a low, Mesozoic, aquifer (marked M). Hydrological basement in the zone of basins is marked B. A simulated Saalian ice sheet is shown above the transect.*

$$K_i = K_{0,i} 10^{\frac{z}{C_i}} \tag{5.6}$$

where C_i is constant, and K_0 a reference conductivity. Furthermore Gustafson and others /1989/, suggest that on the kilometre scale, a single value of conductivity can be assigned to each layer. We have subdivided the sequence in any one zone into three hydrological units (0,1,2), with conductivities K_0, K_1 and K_2 respectively. The assigned values are summarised in Table 5-1.

Table 5-1.

Zone	Extent km		K_0 ms^{-1}	Depth km	K_1 ms^{-1}	Depth km	K_2 ms^{-1}	Depth km
I	720	560	1E-6	< 0.1	5E-8	0.1-0.8	5E-10	>0.8–
II	560	440	1E-7	< 0.1	5E-9	0.1-1.5	5E-11	>1.5
III	440	360	5E-8	< 0.1	3E-9	0.1-1.2	5E-12	>1.2
IV	360	0	3E-7	< 0.1	1E-8	0.1-1.2	5E-12	>1.2

Conductivity is notoriously difficult to estimate with precision, particularly in fractured rocks. Data from Wikberg and others /1991/ suggest a two standard deviation error of an order of magnitude on both sides of the mean.

The deep basin in the southern province has been modelled as an upper, Quaternary aquifer, and a lower, Mesozoic aquifer, separated by a Tertiary clay-rich aquitard, and underlain by an aquiclude of Permian evaporites, which forms hydrological basement.

Single hydraulic conductivity values have been established for each of these three layers from the databases of the Netherlands and German Geological Surveys. This data is summarised in Table 5-2.

Table 5-2.

Zone	Lithology	Age	Conductivity ms^{-1}
Upper aquifer	Sand	Quaternary	3E-4
Aquitard	Clay	Tertiary	1E-10
Lower aquifer	Chalk	Mesozoic	1E-6

In southernmost Sweden, Mesozoic and Cenozoic aquifers develop above Precambrian basement and a Palaeozoic aquiclude (predominantly the Permian Zechstein salt deposits). The aquifer system thickens progressively to 3.5 km depth in the Netherlands (Figure 5-1) with a concomitant increase in transmissivity. Between -200 and -300 km along the transect, in Denmark, there is a narrow zone in which transmissivity is reduced because the surface of the Palaeozoic aquiclude rises. The transmissivity of the distal province (10^5–10^8 m^2yr^{-1}) is typically 2–4 orders of magnitude greater than that of the proximal province. We suggest that the errors of estimation of transmissivity in the distal zone are, as in the proximal zone, an order of magnitude on either side of the central estimate.

5.3.1 Boundaries of the model

The lower boundary of the model is taken as the Permian evaporites in the southern aquifer zone, and the base of unit 2 in the northern, basement area. The southern boundary of the model is at 900 km, where hydrological basement comes to within 800 m of surface, and which, for the purposes of modelling, is presumed to come to surface. Although the modelled ice divide oscillates within a zone 200 km wide during the two glacial cycles, we have arbitrarily fixed the up-glacier limit of the groundwater model. This has little effect on groundwater flow as it lies within a zone of basal freezing for most of the period. Our results show that potential gradients are negligible near the ice divide, and thus that this region is hydraulically stagnant. The fixed ice divide therefore imposes a vertical no-flow boundary in the hydrogeological model.

The ice sheet sole is taken to be an impermeable upper boundary for groundwater flow. Where basal melting occurs, the melt flux is prescribed. Where the total subglacial meltwater discharge is larger than the capacity of groundwater to discharge it, the excess water is presumed to be removed at the ice/bed interface by a combination of conduit flow and flow in a thin layer.

Our reconstructions show that the maximum permafrost thickness in zones beyond the ice sheet is about 100m. As this is much smaller than the thickness of the upper aquifer, the presence of permafrost is not likely to alter groundwater flow radically (for example by pinching out the upper aquifer and driving water into the clay layer or the lower aquifer).

Permafrost has been modelled as a no-flow boundary. However, the transect is crossed by several major rivers, such as the Rhine and the Elbe, and an arm of the southern Baltic, which are likely to have had a sufficiently large thermal impact as to have melted through the permafrost. Rivers have been modelled as a one node 'hole' though the no-flow zone where the applied surface head is equal to the applied topographic head (0 m). For models where the ice sheet has advanced over the course of the Elbe, it is assumed that the river ceased to flow and that its discharge was diverted elsewhere. The Rhine, however, lay very close to the maximum of Saalian glaciation, and is assumed to have been a proglacial river at this time.

Finally, the upper boundary beyond the ice sheet and the permafrost has a prescribed head equal to the topographic head.

5.4 Reconstruction of groundwater flow beneath the European Ice Sheet

5.4.1 Time-dependent simulation of a simple glacial cycle

The model generates the distribution of hydraulic head and the velocity field, from which groundwater trajectories can be determined through the model domain. Effective pressures (p') in subglacial beds may be calculated from:

$$p' = (\rho_s - \rho_w)dg - \Psi \tag{5.7}$$

where ρ_s and ρ_w are the density of solid and water components respectively, d is depth and ψ the water pressure potential.

Application of the full time-dependent model of groundwater flow to the glacial sequence shown in Figure 4-4 would be computationally demanding in relation to the resources available to us. A test was therefore undertaken to establish whether time-dependence could be simulated adequately using a succession of steady states.

The ice sheet model was used to generate a simple cycle of glacier growth and decay, and the pattern and magnitude of ice loading, crustal flexure and basal melting were calculated. These were then used as boundary conditions for a time-dependent computation of groundwater flow along the transect and another series of computations in which time-dependent flow was approximated by a series of steady states for specific time slices.

In the low transmissivity zone, where there is a meltwater excess and the glacier surface is the determinant of the head, heads, head gradients and groundwater velocities are the same in both transient and steady state models. However, in zones of high transmissivity, where groundwater flow can discharge all the melt, heads build up more slowly in the transient model compared with the steady state sequence, and clearly do not reach an equilibrium with the pattern of ice loading and melting. Even here, however, because of the small differences between the head gradients in the two models, groundwater velocities, trajectories and residence times are very similar.

We conclude therefore, that a sequence of steady states can give a reasonable approximation of the time dependent distribution of groundwater heads, head gradients and flow vectors.

5.4.2 Simulation of the last two glacial cycles using a succession of steady states

The impact of glaciation on groundwater flow during the last two glacial cycles was then simulated for the ice sheet time/distance history shown in Figure 4-4 and for a maximum melting rate of 25 mm/yr, using output from the time-dependent glacier model to determine inputs for a sequence of steady state simulations of the groundwater system for specific time-slices. The whole sequence was characterised by 42 time slices.

In the upper, Quaternary aquifer (Figure 5-2) there is a strong upward flow and very high velocities at the ice sheet margin. These are largely a consequence of thinning of the aquifer because of the rising surface of the underlying Tertiary aquitard. Velocities of up to 20 m per year are achieved in this aquifer (Figure 5-3).

In the lower, Mesozoic aquifer (Figure 5-4) flow patterns are again largely determined by aquifer geometry. High effective velocities of up to 0.05 m per year are achieved in the ice marginal zone, where the lower aquifer is pinched out between the Tertiary aquitard and the rising surface of hydrological basement. However, in view of the poor knowledge of permeability geometry at depth in the Mesozoic basin, and the tendency of values derived from single boreholes to overestimate connectivity and large scale permeability, we are sceptical of the details of reconstruction in the lower aquifer.

Velocity vectors in the aquitard are largely a response to changes in transmissivity in the aquifers. When this is reduced in one aquifer, water is driven into the other through the aquitard. Flow in the aquitard is almost invariably vertical.

Figure 5-5 a-b shows instantaneous groundwater trajectories and heads for the Saalian maximum ice sheet and a stage of advance towards it. They show how water draining in the upper aquifer remains in it until discharged at the ice margin. However, because of the very restricted exit from the lower aquifer, between the Tertiary and hydrological basement, much water from the lower aquifer tends to drain upwards through the Tertiary into the upper aquifer between -300 and -750 km along the transect.

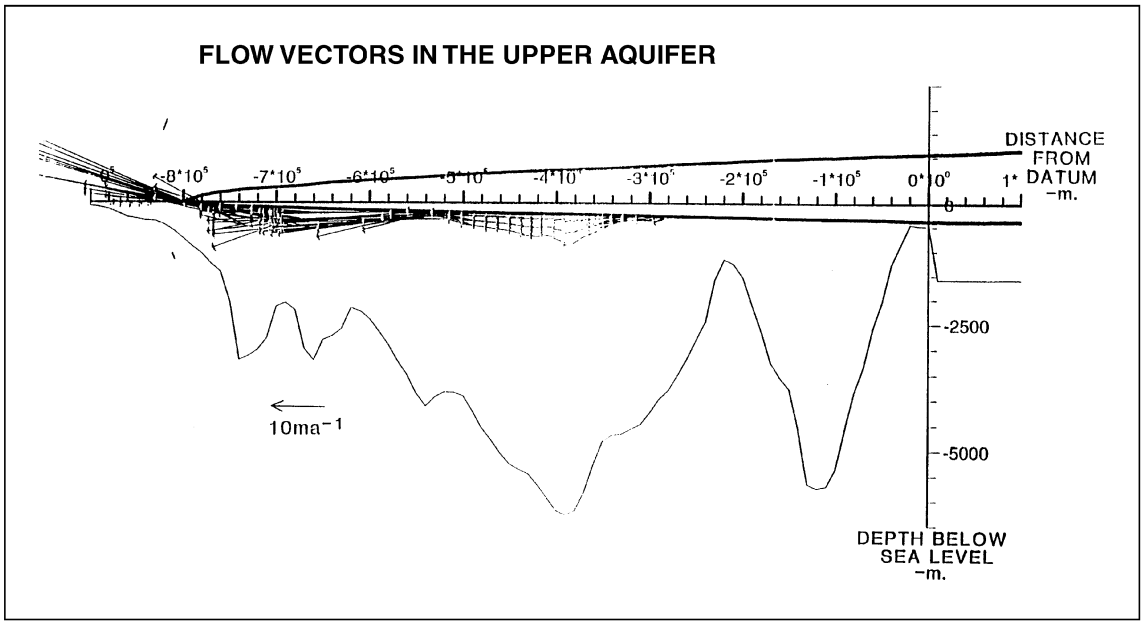

Figure 5-2. *Simulated flow vectors in the upper aquifer during the Saalian maximum.*

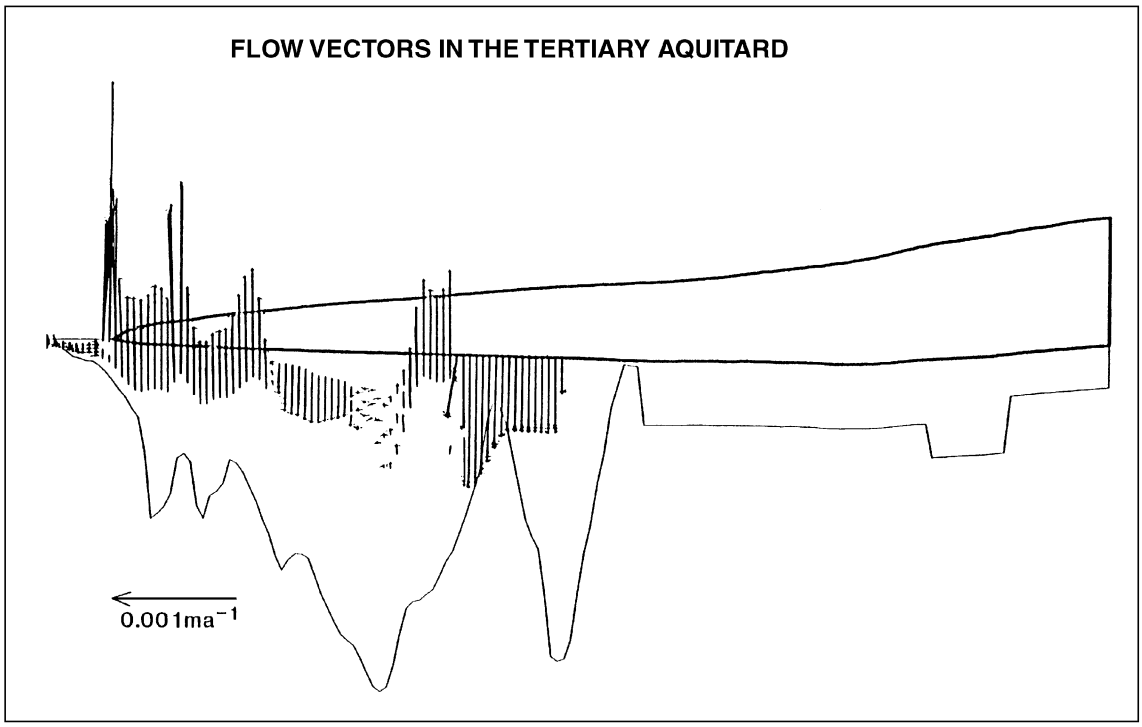

Figure 5-3. Simulated flow vectors in the Tertiary aquitard during the Saalian maximum.

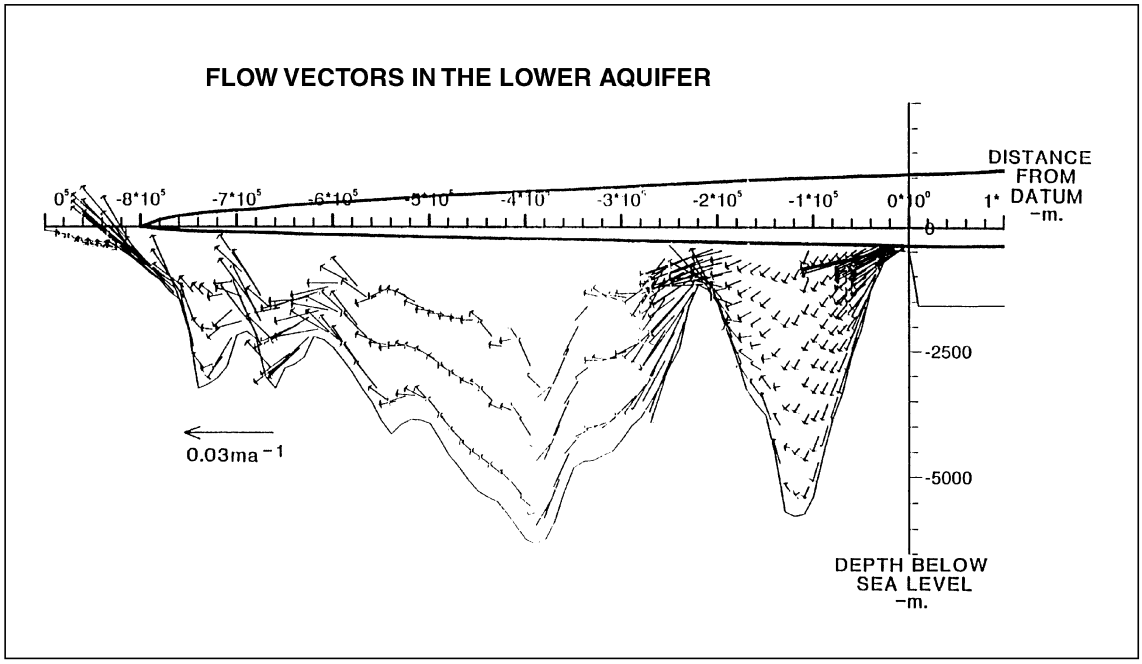

Figure 5-4. Simulated flow vectors in the lower aquifer during the Saalian maximum.

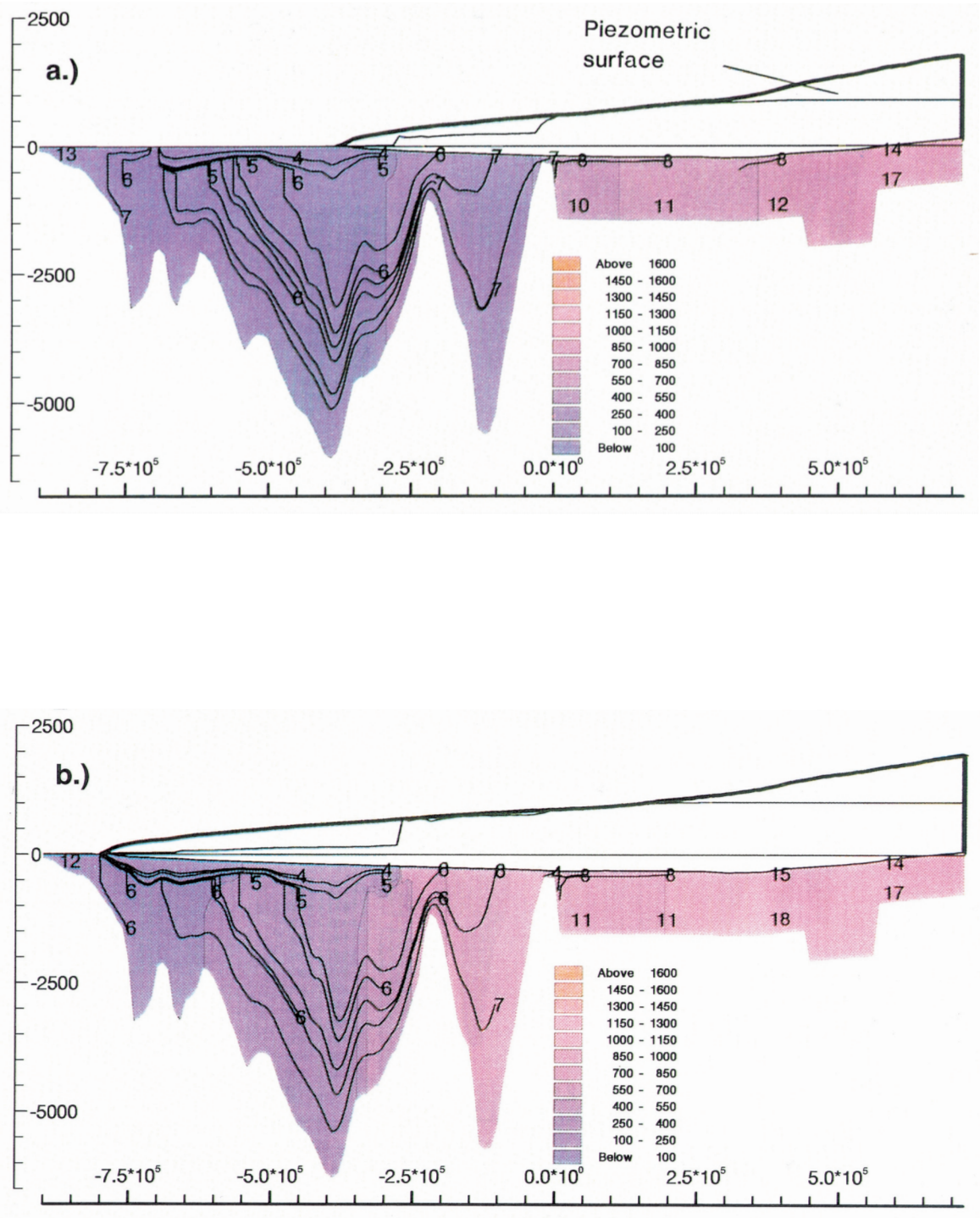

Figure 5-5 a–b. *Simulations showing the groundwater response to an ice sheet advancing along the transect for time-slices during the main phase of the Saalian glacial cycle. Colours in the sub-surface show groundwater heads in metres. The head at the ice bed interface is shown by the thin line beneath the ice sheet surface. Note that in (a) the Tertiary aquitard inhibits water in the lower aquifer from lowing to surface in the proglacial zone, so that much of it is ultimately discharged beyond the Tertiary outcrop in the southern Netherlands (-700 km). Strong vertical head gradients develop between the aquifers and the Tertiary aquitard, reflecting downward flow where the aquifer system thickens and upward flow where the system thins. Lines normal to head contour lines in the sub-surface show groundwater trajectories, with steady state travel times to surface from their starting points indicated by numbers which refer to the travel time in years in powers of 10.*

In the inner part of the transect, beyond 200 km, the ice bed interface is frozen. There is thus no drainage from the ice sheet sole, no water movement below the zone of freezing, and the potential surface is horizontal. Between about 200 and -270 km along the transect, the potential surface is coincident with the ice sheet surface, which reflects the incapacity of shield rocks or the lower aquifer to drain all the basal meltwater. Beyond 200 km, however, the development of the upper aquifer increases the total transmissivity sufficiently to enable groundwater flow alone to discharge all the melt and draw down heads.

Simulations of the vectors heads and trajectories on the Scandinavian basement did not show results significantly different from those reported earlier /Boulton, Caban and Punkari, 1995/. The particular situation at Äspö will be dealt with later.

Figure 5-5 shows the case in which there is no proglacial permafrost. Here, water can escape relatively readily into the proglacial zone and groundwater heads are drawn down below the ice pressure for the whole distance between -270 km and the ice sheet margin. In Figure 5-6 we investigate the role of permafrost, for a case in which the ice sheet terminates above the marine limit in southern Sweden. In this case, apart from in the zone of stagnant groundwater, groundwater heads are the same as ice pressures, as transmissivities are inadequate to discharge the total melt by groundwater flow alone. Beyond the ice sheet margin, permafrost extends as far as the Baltic, where glacially-driven groundwater flowing from beneath the permafrost to the north, can be discharged. As a consequence of the effect of proglacial permafrost in preventing discharge at the ice sheet margin, groundwater heads exceed the overburden pressure beneath the permafrost and for some 50 km within the ice sheet margin.

The relatively high permeability zone within the topmost 100 m of bedrock (see Table 5-1) carries the dominant proportion of groundwater flow. Transit times for water from beneath the ice sheet to the proglacial zone are 5 orders of magnitude greater from the topmost 100m than from a depth of 1000 m.

Figure 5-7 a-d shows effective pressures beneath the ice sheet during build up to the Saalian maximum for the transient. At the maximum extent, groundwater heads are drawn

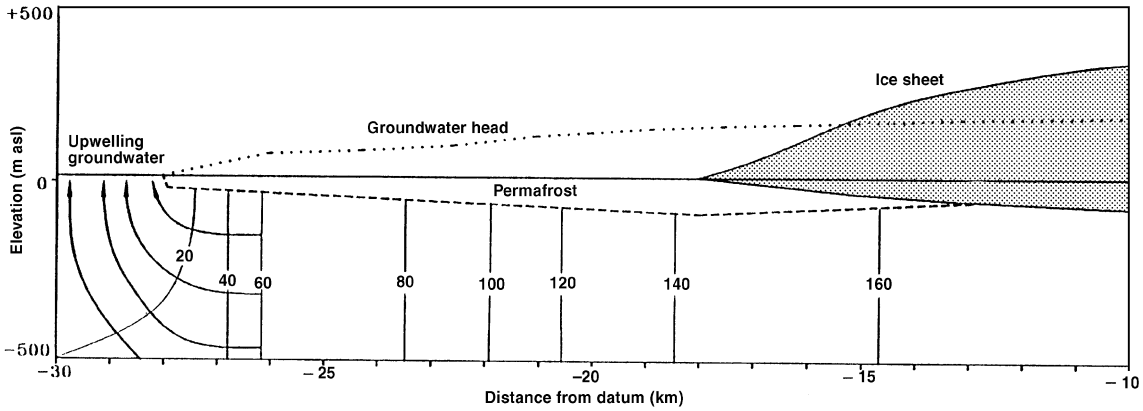

Figure 5-6. *Simulation of the ice sheet marginal zone above the marine limit in southern Sweden. Permafrost extends from beneath the glacier margin as far as the marine limit, where permafrost terminates. A groundwater head gradient must be maintained beneath the permafrost in order to sustain the flow from beneath the ice sheet. As a consequence, the head will lie above the permafrost surface and there will be a buoyant force on the base of the permafrost. There is zero head at the point where permafrost ends, where there will be strong upwelling of groundwater.*

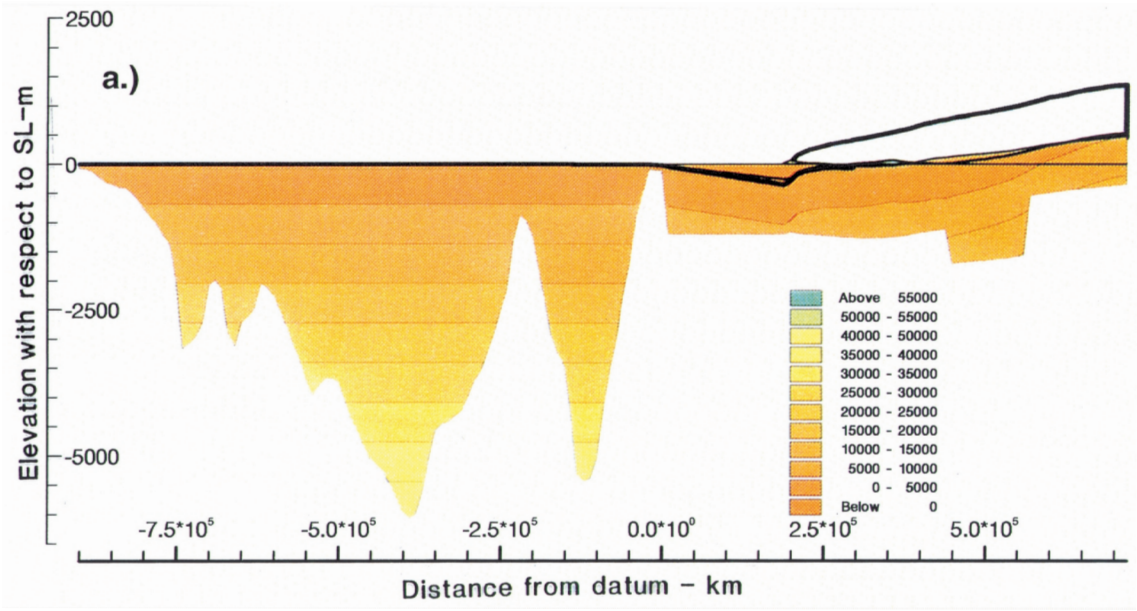
a.)
2500
0
-2500
-5000
Elevation with respect to SL-m
-7.5*10^5
-5.0*10^5
-2.5*10^5
0.0*10^0
2.5*10^5
5.0*10^5
Distance from datum - km
Above 55000
50000 - 55000
40000 - 50000
35000 - 40000
30000 - 35000
25000 - 30000
20000 - 25000
15000 - 20000
10000 - 15000
5000 - 10000
0 - 5000
Below 0

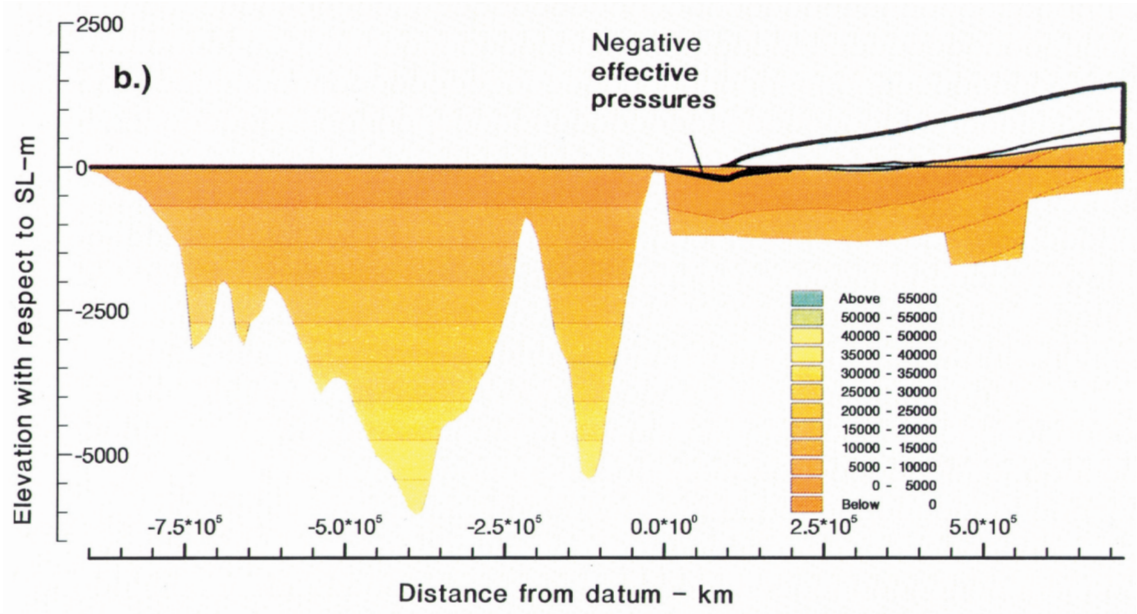
b.)
Negative effective pressures
2500
0
-2500
-5000
Elevation with respect to SL-m
-7.5*10^5
-5.0*10^5
-2.5*10^5
0.0*10^0
2.5*10^5
5.0*10^5
Distance from datum - km
Above 55000
50000 - 55000
40000 - 50000
35000 - 40000
30000 - 35000
25000 - 30000
20000 - 25000
15000 - 20000
10000 - 15000
5000 - 10000
0 - 5000
Below 0

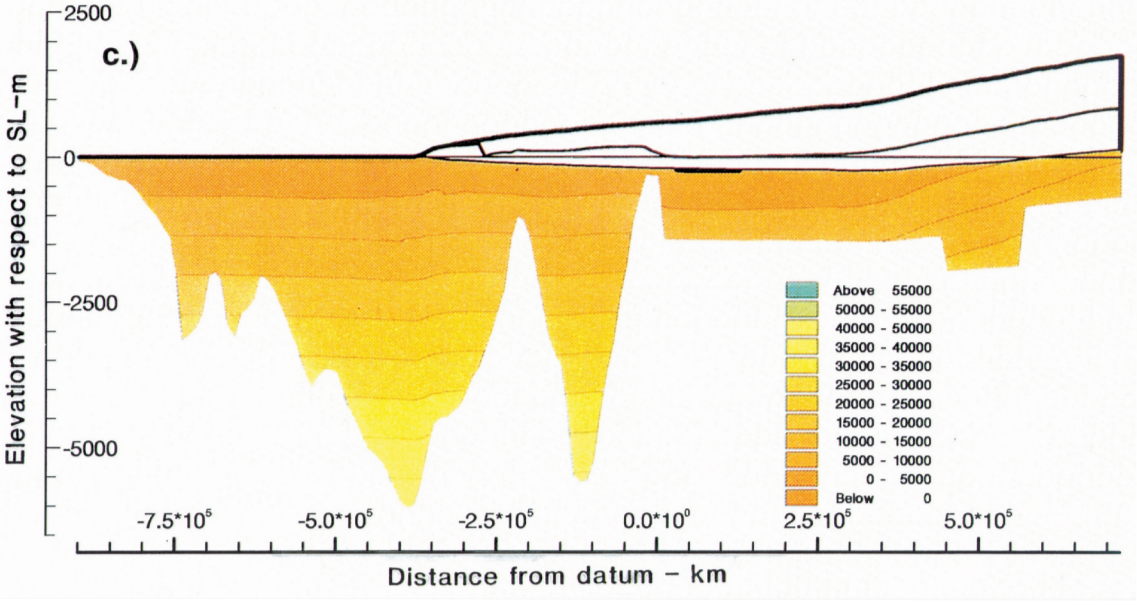
c.)
2500
0
-2500
-5000
Elevation with respect to SL-m
-7.5*10^5
-5.0*10^5
-2.5*10^5
0.0*10^0
2.5*10^5
5.0*10^5
Distance from datum - km
Above 55000
50000 - 55000
40000 - 50000
35000 - 40000
30000 - 35000
25000 - 30000
20000 - 25000
15000 - 20000
10000 - 15000
5000 - 10000
0 - 5000
Below 0

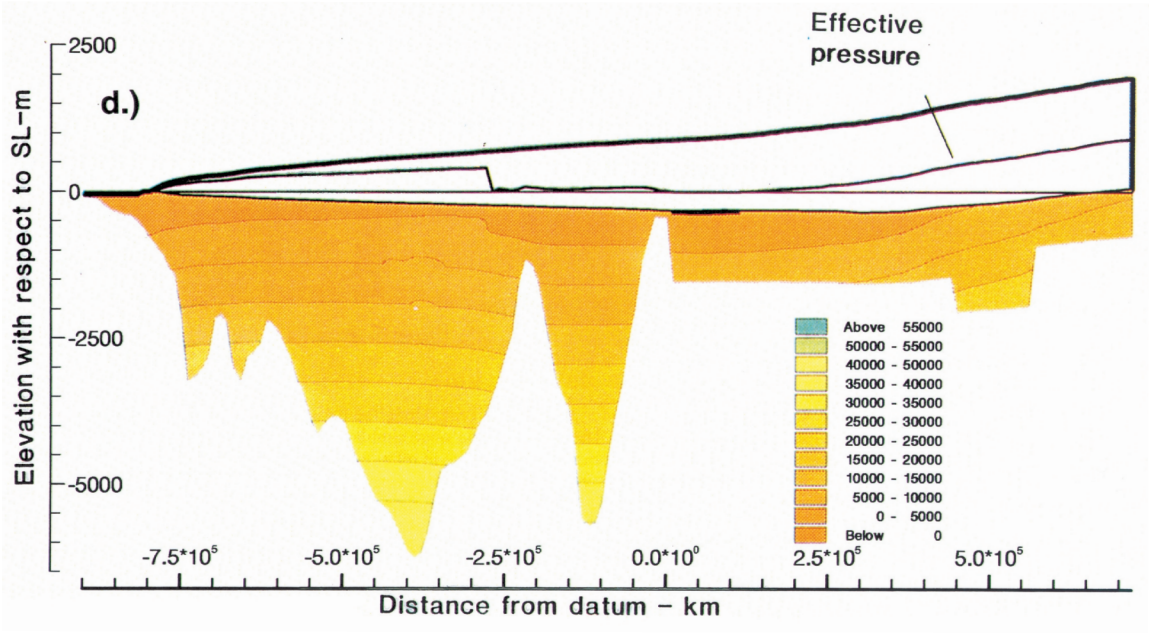

Figure 5-7 a–d. *Effective pressure distribution in the sub-surface for the simulation shown in Figure 5-5. Effective pressure at the ice bed interface is shown by the thin line beneath the ice sheet surface and is equivalent to an ice pressure in metres. In the sub-surface, effective pressures are shown by shading, the key is in Pascals. Note the zone of very high effective pressure in the zone of no melting beneath the ice divide.*

down strongly in a very broad terminal zone. Effective pressures are high in the divide region and in terminal zone, and low or zero in the intermediate zone. The maximum effective pressure at the ice sheet sole of about $8x10^6$ Pa occurs beneath the ice divide. Effective pressures of $4x10^6$ Pa occur at the sole at about -300 km, just beyond the point at which strong drawdown occurs (Figure 5-5) as the upper, Quaternary aquifer thickens. These changes have a major transient effect on effective pressures at depth within the aquifer systems.

It should be noted, however, the model ignores the drawdown of the groundwater table which would be produced by the development of conduits at the ice bed interface.

5.5 Conclusions

a) Maximum groundwater velocities and discharges occur beneath the terminal zone of the ice sheet (driven by the maximum potential gradient) when it reaches its maximum extent. Comparisons of velocity and the horizontal component of discharge in the vertical plane of the transect, between the upper and lower aquifers and the Tertiary aquitard in the aquifer zone are shown below, (other than in the terminal zone, where special conditions apply):

	Maximum velocity	Maximum discharge
Upper aquifer	20 ma^{-1}	5000 m^2a^{-1}
Aquitard	0.002 ma^{-1}	0.01 m^2a^{-1}
Lower aquifer	0.04 ma^{-1}	10 m^2a^{-1}

Velocities in the upper aquifer are 2–3 orders of magnitude larger than in the lower aquifer, and 2–3 orders of magnitude larger than modern values in the upper aquifer. Bulk discharge in the upper aquifer is about 5000 m^2a^{-1} at the period of maximum glaciation, which is about 500 times larger than that through the lower aquifer. It would require about 100,000 years for the northern basin of the upper aquifer (-250 to -500 km) to be completely flushed out by glacial meltwater, and about 13,000 years for the southern basin (-550 to -750 km) to be flushed out.

b) If we are concerned primarily with the fate of glacial meltwater and its role in ice sheet dynamics, the lower aquifer can be ignored. This is fortunate, as we are much less confident about the conductivity representation of the lower aquifer compared with the upper. The upper aquifer comprises a series of thick, relatively continuous sand units which dominate transmissivity, and intervening fine-grained units which contribute very little to transmissivity. In the former we do not expect permeability to vary strongly with effective pressure and therefore suggest that groundwater flow within it will be dominated by meltwater recharge. Within the fine-grained units, initial groundwater flow is likely to reflect sediment consolidation. The lower aquifer is lithologically more complex, connectivity is more difficult to evaluate, and the loading effect of the ice sheet is most likely to dominate the groundwater flow field, at least in the early stages of ice sheet loading.

c) Transit times to surface from within the upper aquifer in the southern basin and the uppermost geohydrological unit on the Shield are relatively short. Transit times to surface for groundwater emanating from any depth within the upper aquifer (to 1000 m depth) and for the whole horizontal extent of the aquifer of 600 km, are up to a maximum of 10,000 years.

d) The irregularity of the Permian evaporite surface causes groundwater to be drawn down through the Tertiary aquitard into the lower aquifer when the Permian surface descends, and to be forced back through the Tertiary into the upper aquifer when the Permian surface ascends. The transit times of groundwater to the surface from any point within the lower aquifer is of the order of 10^5–10^6 years.

e) The time-dependent head and effective pressure (ice head minus water head) distributions show clearly defined patterns. Beneath the ice divide zone of basal freezing, the potential gradient is zero and effective pressures can be large; up to 10,000 kPa in the case of the Saalian maximum condition. Where there is melting over the zone of low transmissivity basement, effective pressures are zero, and we expect widespread subglacial tunnels to develop.

f) In the outer, aquifer zone, high transmissivities tend to draw down water pressure heads to give relatively large effective pressures. Measurements of preconsolidation pressures in surficial clay rich sediments at about -600 km in this zone give values at the base of the clays (the top of the Quaternary aquifer) in the range

2000–3000 kPa /Boulton and Dobbie, 1993/ which agree well with typical values of 2000–4000 kPa simulated in our models.

g) The zone of permafrost extension beyond the ice sheet is of great importance in controlling hydraulic behaviour in the terminal and proglacial zone.

h) Glacial cycles produce cyclical pulses of pressure and groundwater flow through the European sub-surface which are the strongest impacts which European groundwaters have suffered during recent geological time.

i) Evidence for large scale energetic patterns of former subglacial groundwater flow will be found in distinctive groundwater geochemistry. The geochemical signature of glacial meltwater is distinctive. For instance, in comparison with meteoric recharge, we expect it to have a very light O-isotope signature. Smellie and Laaksoharju /1992/ have found such water dating from the latter part of the last glacial period in low permeability rocks at 300 m depth at Äspö, Sweden.

6 Time dependent changes at Äspö / Laxemar

The glacially-driven flow trajectories at Äspö / Laxemar have been modelled through the last two glacial cycles. Once the glacial influence has withdrawn, we assume no further flow, as an analysis of non-glacial conditions, to have any value, would need to take into account detailed topographic features, which can be assumed to have a second order influence when glacial forcing dominates the flow but which become important when groundwater flow is again topographically controlled. Moreover, the large scale of modelling required to simulate glacial forcing, because of the large scale integration of glacial processes, cannot take small scale topography into account. We anticipate that the large scale model will generate boundary conditions for a more detailed local model.

The improved model confirms the analysis of flow vectors for different phases of ice sheet extension reported in detail in an earlier report /Boulton, Caban and Punkari, 1995/. Figure 6-1 shows the general distribution of groundwater flow vectors associated with an

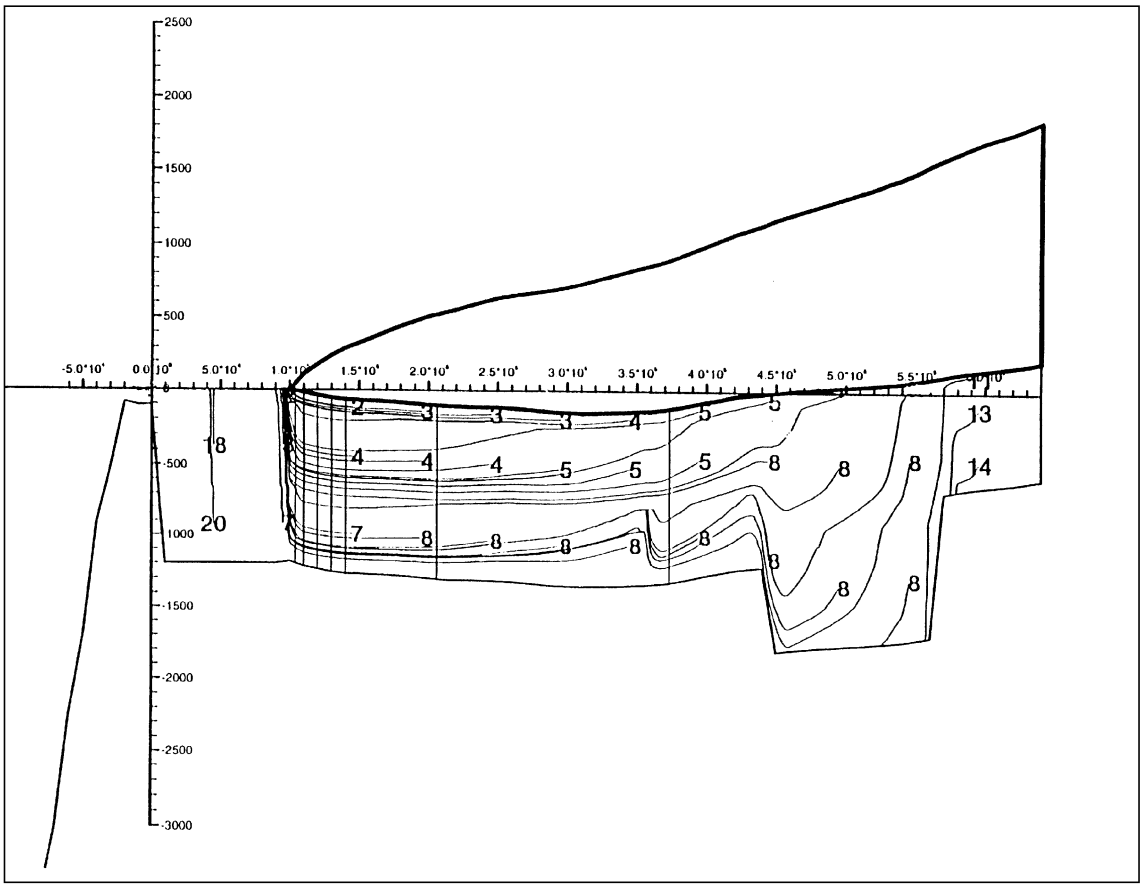

Figure 6-1. *Simulation of groundwater flow beneath an ice sheet flowing along the transect and terminating on the shield in a position equivalent to that of the Younger Dryas ice sheet margin. The sub-surface hydrogeology is as show in Figure 5-1 and Table 5-1. Groundwater flow trajectories are shown to be generally downwards beneath the ice sheet and strongly upwards immediately beyond the ice sheet margin. Numbers at the initial points of the trajectories show the time in years (given in powers of ten) which would be taken for water to reach the surface at the ice sheet terminus if a steady state were maintained. No permafrost is shown beyond the ice sheet margin as it is assumed that the ice sheet terminated in a Baltic ice lake.*

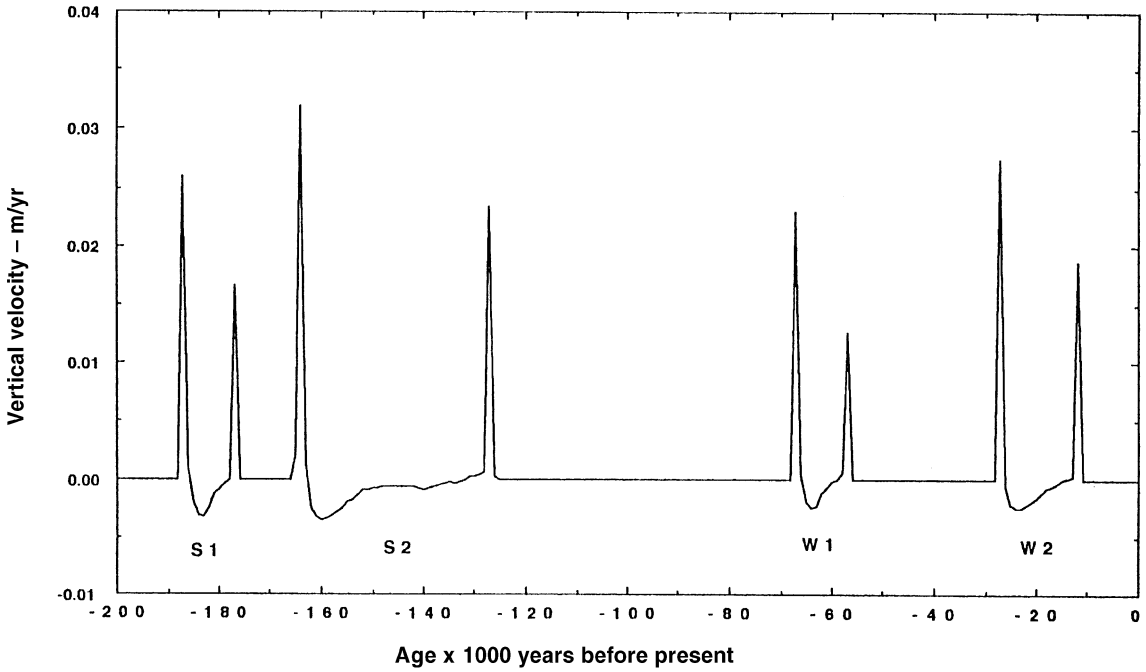

Figure 6-2. *Simulated variation in the vertical velocity of groundwater at Äspö / Laxemar through the last two glacial cycles. Beneath the ice sheet, movement is predominantly downwards as the ice sheet expands and is almost parallel to the ice / bed interface during the glacial maximum and during decay. There is strong upward movement just beyond the ice sheet margin. Early and late Saalian and Weichselian phases of glacier recharge to groundwater are shown as S1, S2, W1 and W2.*

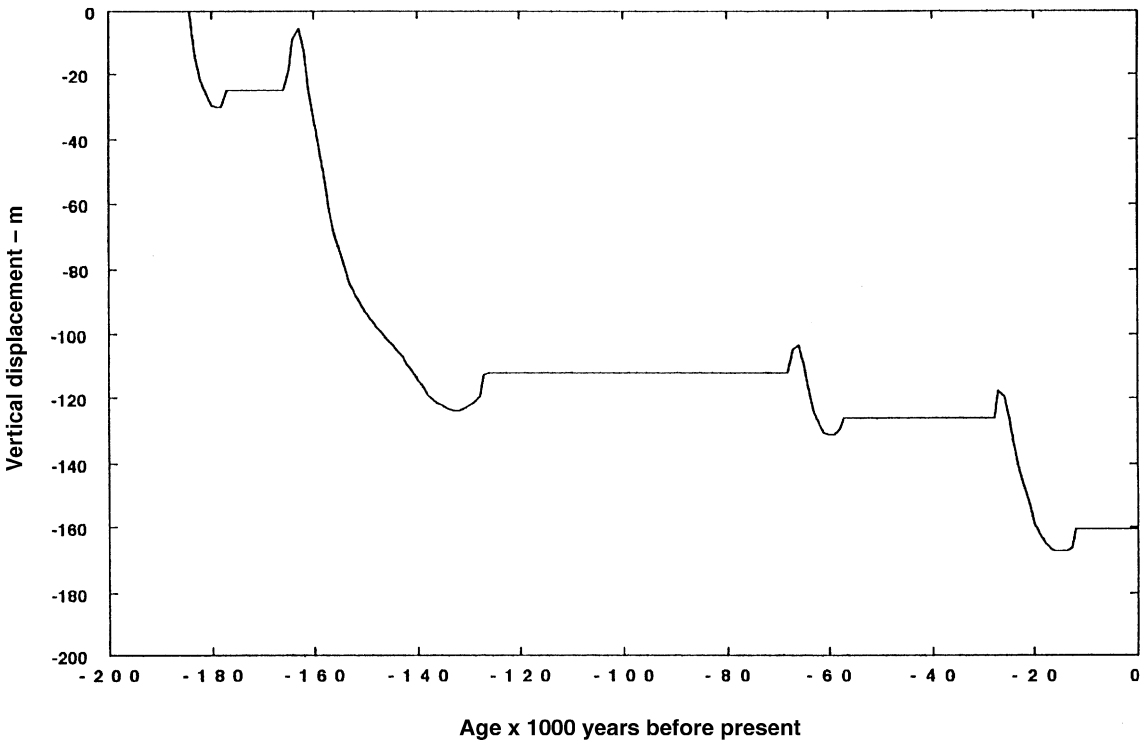

Figure 6-3. *The cumulative vertical displacement of groundwater at Äspö / Laxemar from its original recharge position through the last two glacial cycles.*

ice sheet in Sweden. We have now computed, however, the time dependent displacement of groundwater parcels at the location of the Äspö / Laxemar site through the last two glacial cycles. Figure 6-2 shows the vertical velocity of water parcels in the topmost 100 m of the subglacial bed through the last two cycles. Note that groundwater movement is downwards during the early parts of glacial cycles, when the site lies deep beneath the ice sheet, but that it moves upward at relatively high velocity at and beyond the glacier margin when the site lies in this zone. The resultant time dependant displacement of groundwater recharge from the beginning of the penultimate (Saalian = isotope stage 6) glacial cycle is shown in Figure 6-3.

These results can be used to predict the present location of recharge of different age. Figure 6-4 shows the predicted location of groundwater parcels injected subglacially into the groundwater system during glacial phases since the early Saalian.

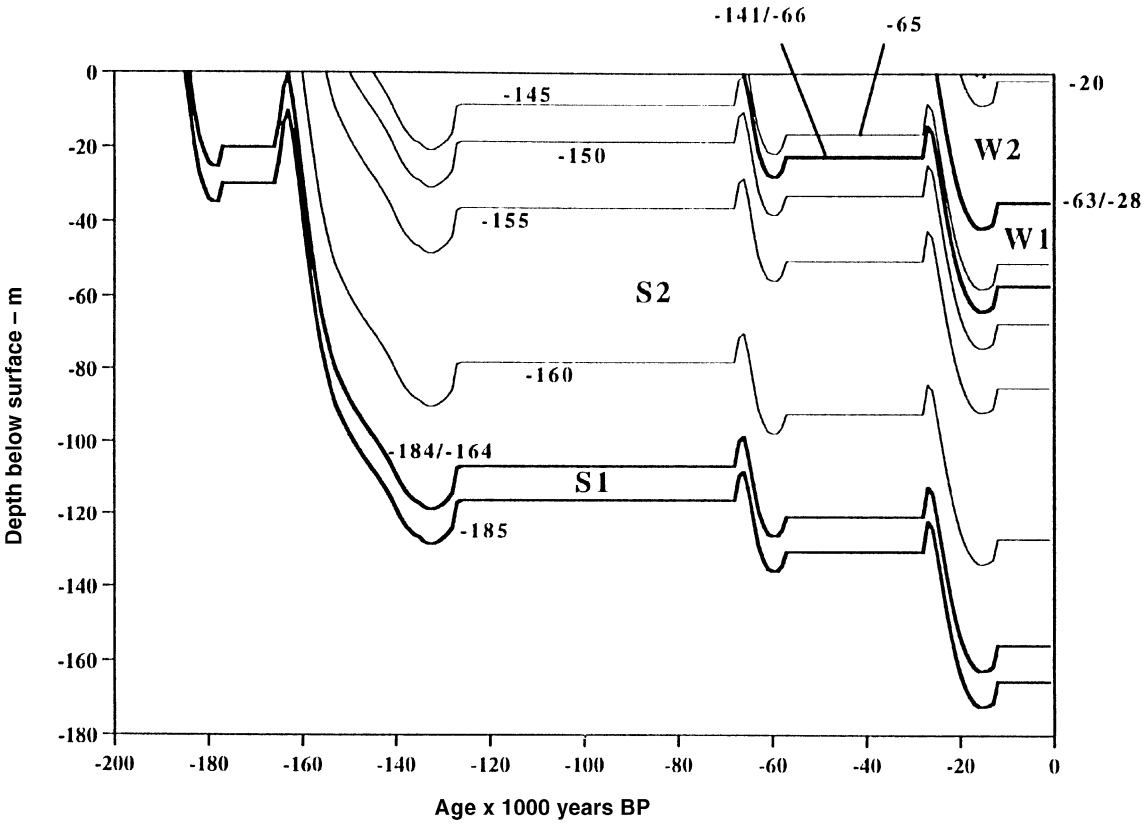

Figure 6-4. *An age model for groundwater at Äspö/Laxemar. It assumes that recharge and groundwater flow only occur during glacial cycles, and that there is no diffusion or mixing. It uses the simple, vertically-layered Darcian permeability distribution produced by Wallroth and Gustafson /1993/. It shows the cumulative vertical displacement of parcels of water which are injected subglacially into the groundwater system at given times. The numbers on individual fine lines show the age of recharge in 1000 s of years before present. The heavy lines show discontinuities in groundwater stratigraphy. The time gaps represented by them are shown on the line (-184/-164 means that there has been no recharge between 184 ka and 164 ka). There are two reasons for this lack of recharge. Firstly because of the assumption of only glacial recharge, and secondly because of strong upward water movement at the ice sheet margin, which not only prevents recharge during that phase, but also sucks up older water, which is therefore not represented in the groundwater stratigraphy. The movement of the water packages deriving from the Saalian and Weichselian events shown as S1, S2, W1 and W2 in Figure 6-1 are shown.*

These predictions suggest that glacial waters should be found at sampling depths at Äspö / Laxemar. It should be remembered, however, that the model is not appropriate for site specific predictions, it merely suggests that a search for geochemically distinctive groundwater spikes as a means of understanding the long term behaviour of groundwater at this site is a sensible objective which could yield very important results. Such a search requires prior site specific modelling utilising a more appropriate fracture-permeability model, with a detailed description of the rock mass, the local topography, a more detailed description of palaeoenvironmental sequences and density and temperature dependent groundwater modelling. The current model uses a simplified description of hydrogeology and assumes no diffusion or mixing in subglacial groundwaters.

7 Distribution of stress and strain beneath an ice sheet

In section 5, we discussed the distribution of effective pressure beneath an ice sheet. We now use this to help determine the distribution of stress.

7.1 Stresses

The stress distribution in the earth, is the superposition of several stress components. These include gravitational stresses (self weight), pore water pressure, tectonic (background) stresses, flexural isostatic stresses and concentrated loading stresses. The later are often neglected when considering the state of stress in the earth, and although concentrated loading stresses have only a very short penetration range, they are of critical importance in considering the state of stress near the surface, where other stress components are often much smaller in magnitude. For example, in glacial hydrology problems, the near surface concentrated loading stresses caused by an ice-sheet will be of much greater magnitude than the overburden or the head, and may be large enough to fracture the subsurface. Thus there exists the possibility that ice-sheet loading stresses will radically alter hydrological parameters, such as permeability, and hence alter groundwater pathways.

The glacial case also includes a component of shear stress due to the drag of the ice sheet over its bed as a result of sliding over the bed.

A simple theory of concentrated loading is summarised in Appendix II.

Instantaneous stresses in response to a prescribed ice sheet load have been computed for a series of time-slices through the time-dependent history of ice sheet advance and decay shown in Figure 4-4. The results are shown as follows:

Figure 7-1 shows the orientation of the principal stress axes (σ_1) in the ice-marginal zone, assuming the absence of tectonic stresses. Only the ice marginal zone is shown as it represents a transition between a vertical principal stress regime beneath the ice sheet and a horizontal principal stress regime beyond the ice sheet. This is computed for the Saalian maximum simulation, but can be regarded as a generic description.

Figure 7-2 shows the groundwater heads and maximum and minimum effective stresses for the ice sheet marginal zone in a position equivalent to the late Younger Dryas stage. Permafrost extends beyond the ice sheet and is responsible for a broad proglacial zone in which (σ_1 and σ_3) are both tensile and a zone beneath the ice sheet where only (σ_3) is tensile. The principal tensile stress beyond the ice sheet has only a small negative value.

Figure 7-3 shows the maximum and minimum effective stresses for the same simulation as in Figure 7-2, but for the whole ice sheet as far as the ice divide.

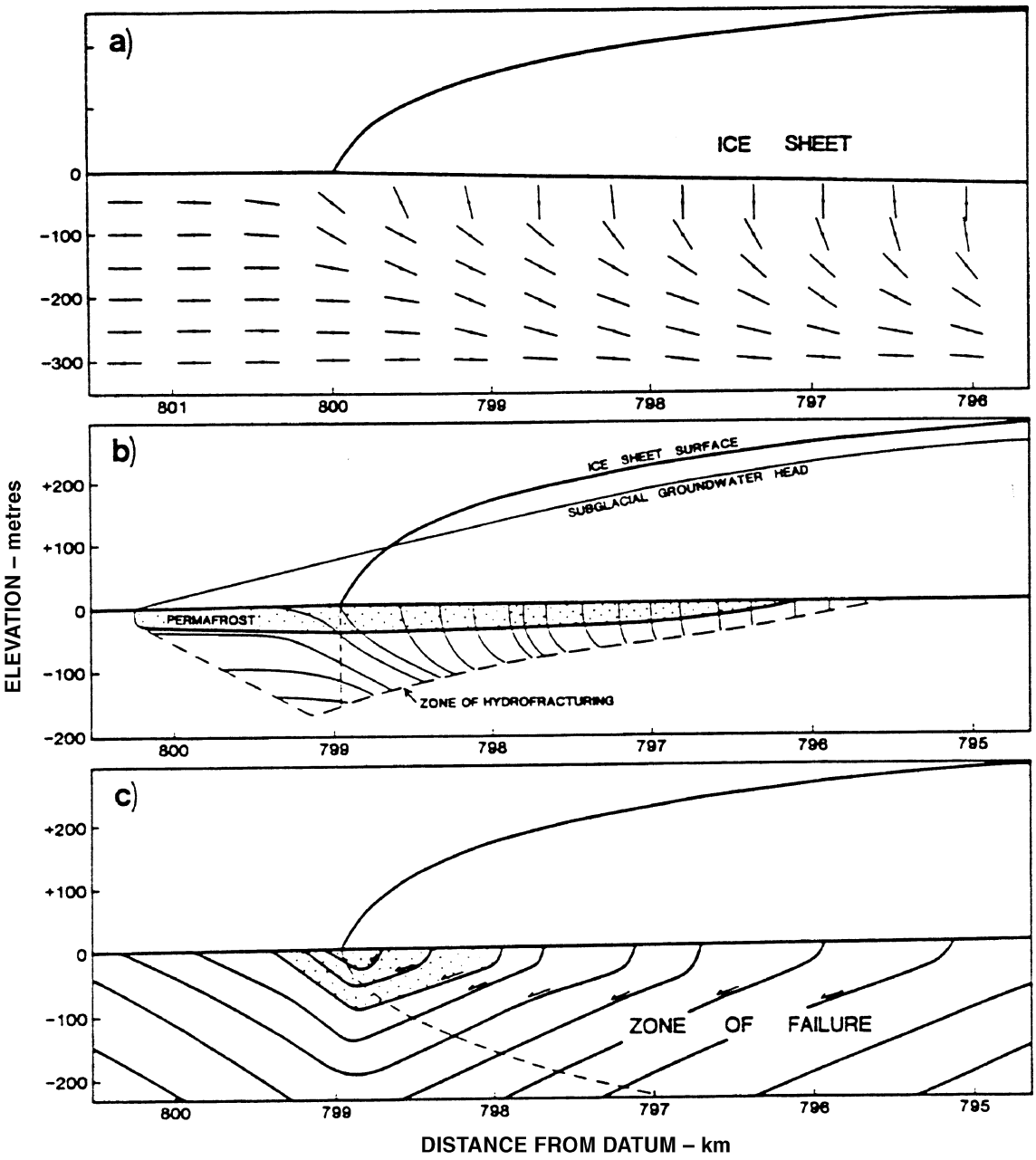

Figure 7-1. *(a) Ice sheet terminating at 800 km along the flowline /as in Figures 1 and 2, Boulton et al, 1995/ showing the calculated orientations of sub-surface principal stresses. (b) The modelled distribution of permafrost, the subglacial groundwater head and the zone within which major hydro-fracturing would be developed. The greatest tendency to hydrofracturing will occur to the right of the vertical line drawn in the zone of hydrofracturing. (c) The sliplines for shear failure in response to ice sheet loading. They are the lines along which safety factors are at a minimum. The dashed line shows the zone within which failure is predicated at all locations. Failure is predicted along the proximal parts but not the distal parts of all planes. If the shear stress and shear resistance are summed along all continuous sliplines, failure could occur along all planes within the shaded area. It is suggested that the existence of permafrost will also play a role in determining whether long-distance movement will occur along a given plane.*

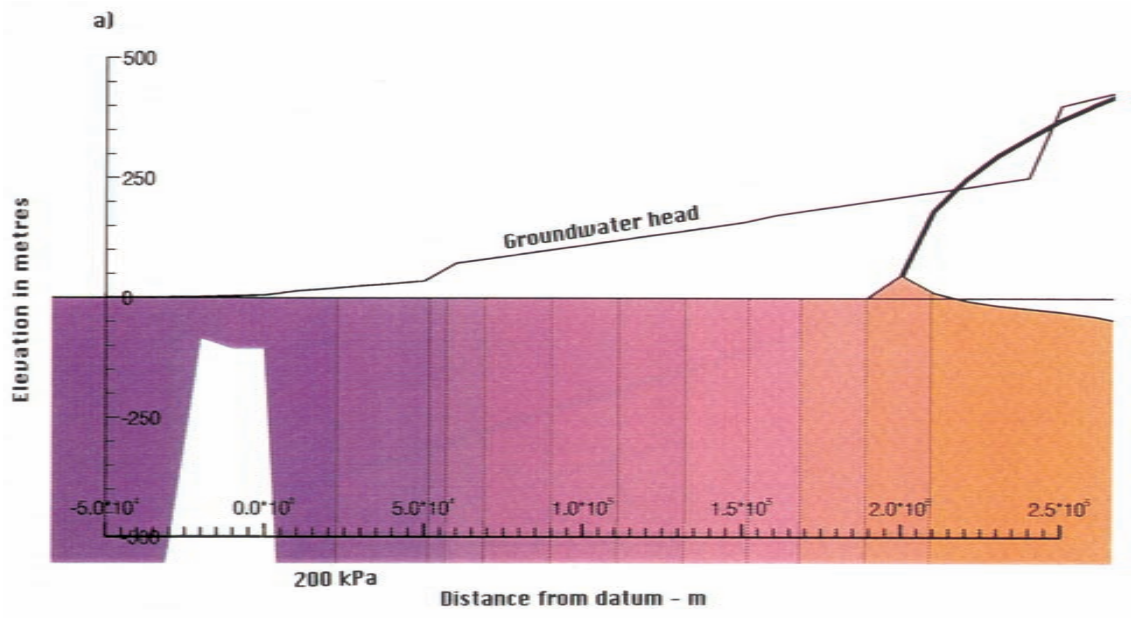

Figure 7-2 a. *Sub-surface potentials (heads) for an ice sheet flowing along the transect /see Boulton* et al, *1995, Figure 1/ and terminating above the marine limit at the Younger Dryas ice margin in Sweden. There is extensive permafrost beyond its margin.*

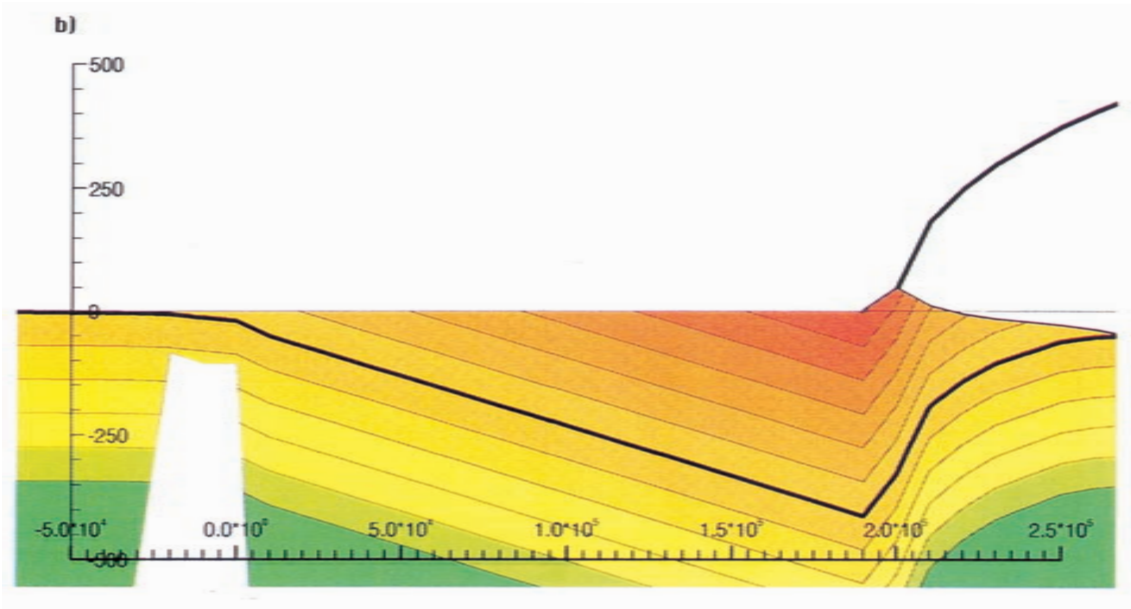

Figure 7-2 b. *Sub-surface effective minimum stresses in the terminal and proglacial zone. The heavy line shows zero minimum stress. Stresses above it are tensile and below it compressive. The tensile zone is one of potential hydrofracturing. Contours are plotted at 500 kPa intervals.*

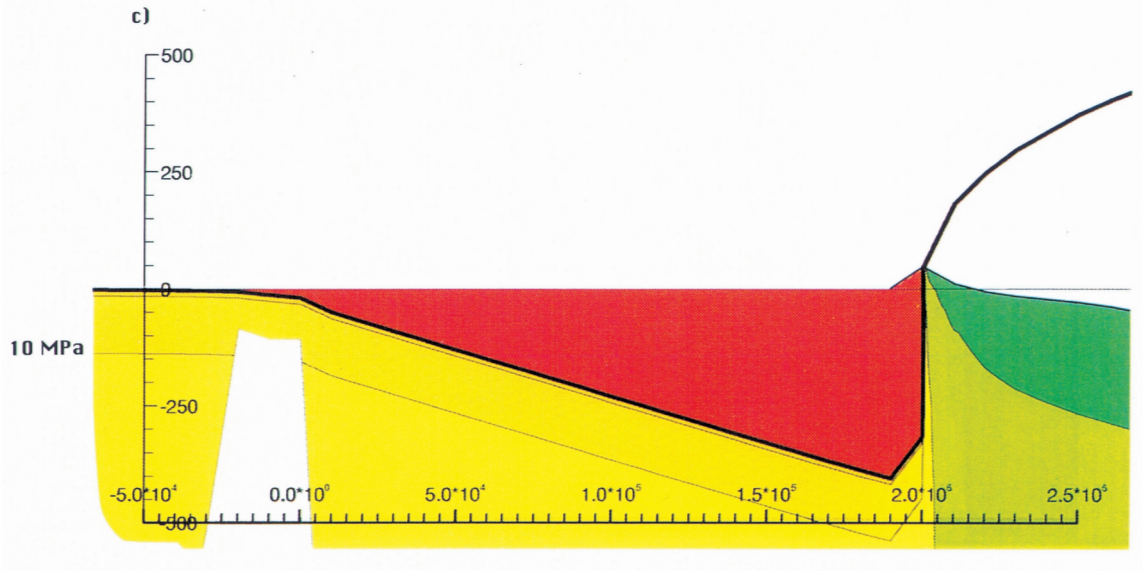

Figure 7-2 c. *Magnitude of the maximum principal stress in the subglacial and proglacial zone. Stresses are tensile above the heavy line and compressive below it. Note that although there are water overpressures beneath the glacier terminus the maximum stress is compressive.*

The ice sheet induces failure in the substratum in three ways:

By movement

- shear failure in response to the drag on the substratum imposed by the movement of the ice sheet.

By loading

- tensile fracturing parallel to the direction of maximum stress when the minimum stress is tensile;
- shear fracture when the deviatoric stress exceeds rock or sediment strength.

By hydraulically induced stresses

We now examine the theoretical distribution of these modes of failure and some of their geological expressions.

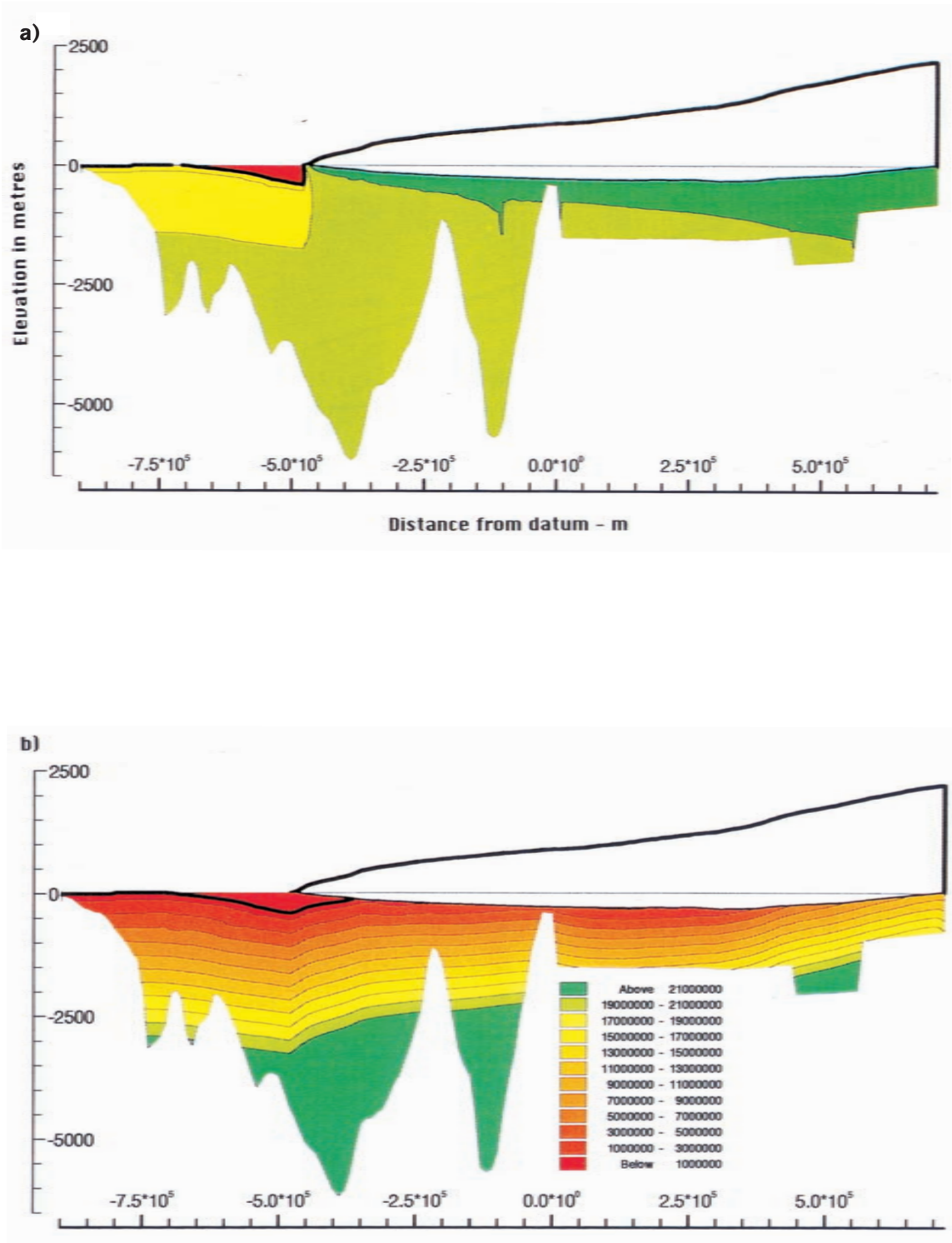

Figure 7-3 a-b. *An ice sheet terminating along the transect at the late Saalian, Warthe maximum position showing: (a) the computed magnitude of principal stresses. (b) Minimum stresses beneath and beyond an ice sheet. Stresses above the heavy line are tensile and below it compressive. The zone where minimum stresses are tensile is one of hydrofracturing.*

7.2 Failure due to drag of the ice sheet over its bed

This process has been described and analysed previously /Boulton, 1987; Boulton and Hindmarsh, 1987/. The shear strength (S) of a material under a given effective pressure p' is given by:

$$S = C + p' \tan \phi \tag{7.1}$$

where C is cohesion (tensile strength) and ϕ is the angle of internal friction. The depth to which shear deformation will occur (t_A) will be:

$$t_A = \frac{\frac{\tau - C}{\tan \phi} - p'_0}{\frac{\delta p'}{\delta z}} \tag{7.2}$$

where (τ) is the shear stress at the base of an ice sheet, $\frac{\delta p'}{\delta z}$ is the vertical effective pressure gradient from equation (7.1) (assuming no significant vertical potential gradient), and p'_0 is the effective pressure at the glacier sole. For a sediment with $\phi = 30^o$ and C = 0, beneath an ice sheet where p'_0 is zero and with a typical value of $\frac{\delta p'}{\delta z}$ of about 10 kPa/m for the sediment, the depth to which pervasive shear deformation will occur is only about 17 m. It is an essentially shallow, thin-skinned phenomenon, although it could occur at considerable depth if very high pore water pressures are attained.

7.3 Shear failure due to ice sheet loading

The orientations of principal stresses induced by ice sheet loading in the terminal zone of the ice sheet are shown in Figure 7-1. The angle (θ) between the principle stress orientation and the plane of failure is given by

$$\theta = 45^0 + \frac{\phi}{2} \tag{7.3}$$

The shear stress along the plane of shear (τ_s) and the effective normal stress across the plane of shear (σ'_n) are given by

$$\tau_s = \frac{\sigma'_1 - \sigma'_3}{2} \sin 2\alpha \tag{7.4}$$

$$\sigma'_n = \frac{\sigma'_1 + \sigma'_3}{2} + \frac{\sigma'_1 - \sigma'_3}{2} \cos 2\alpha \tag{7.5}$$

Failure will occur when

$$\frac{\tau_s - C}{\sigma'_n} \geq \tan \phi \qquad (7.6)$$

Figures 7-4 and 7-5 show values of $\frac{\tau_s - C}{\sigma'_n}$ along planes of principal stress beneath the ice sheet at different stages of advance along the transect for beds with different mechanical properties. In the bed in Figure 7-4, C = 0 and $\phi = 35^o$, representing a cohesionless sediment with a very high angle of friction. In the bed in Figure 7-5, C = 20 MPa and $\phi = 45^o$, representing typical strength parameters for intact granitic bedrock /Birch, 1966/.

The areas within which $\frac{\tau_s - C}{\sigma'_n} > \tan \phi$, and within which shear failure will therefore occur are shown by heavy lines. It can occur area beneath the ice sheet, but not beyond it.

In unlithified rocks (Figure 7-4), it is suggested that shear fracturing can occur to depths in excess of 1 km. Even in intact basement rocks (Figure 7-5), we suggest that beneath the ice divide region, where very large effective stresses can occur (Figure 7-3) because of low water pressure heads /see Boulton, Caban and van Gijssel, 1995; Figure 7-5/, shear fractures can be expected to depths of about 500 m. Beyond this zone (500 km), we expect shear fractures to depths of 100–200 m.

There are relatively few observations which can be used to test these predictions because of the difficulty of establishing the age and origin of the ubiquitous fractures in rocks and sediments. There are numerous observations, however, in basement regions of Sweden which suggest very high fracture frequencies within the topmost 100 m /Ahlbom et al, 1991; Gustafson et al, 1989/. We suggest the possibility that these high near surface joint frequencies are a consequence of shear failure induced by glaciation.

The ice margin is a zone in which the magnitude and direction of shear stresses changes rapidly. Figure 7-1 shows the directions of principal stress in this zone. Shear failure can theoretically occur along conjugate planes which lie at angles of (θ) on both sides of the principle stress axis. In practise, fracture will only occur along planes on which displacement can occur readily. Thus, beneath ice sheet, only shear planes with a down-glacier dip will tend to form (Figure 7-1), permitting shear displacement to occur in a down-glacier direction. As the principal stress axis flattens beneath the glacier margin, and the conditions for failure are still achieved, the dip of failure planes decreases and then reverses, until, in the outermost part of the zone of failure, they dip up-glacier. This general pattern was qualitatively deduced by Rotnicki /1976/.

Figure 7-1 shows the predicted orientation of planes along which the deviatoric stresses (difference between the shear stress along the plane of fracture and the stress normal to the plane) will be a maximum, and which therefore give the most probable orientations of failure planes. In this simulation we assume unlithified sediments with comparatively slight cohesion, and a value of $\phi = 35^o$. The zone in which the failure criterion (equation 7.6) is satisfied is that shown inside the dashed line, and is restricted to the subglacial area. Whilst local shear failure can be expected to occur in the direction indicated within the zone of failure, relative movement across shear planes within the zone of failure far from the margin can only be slight as it must be taken up by compaction of the materials above the shear plane, as the planes pass into a broad zone of strong sediments.

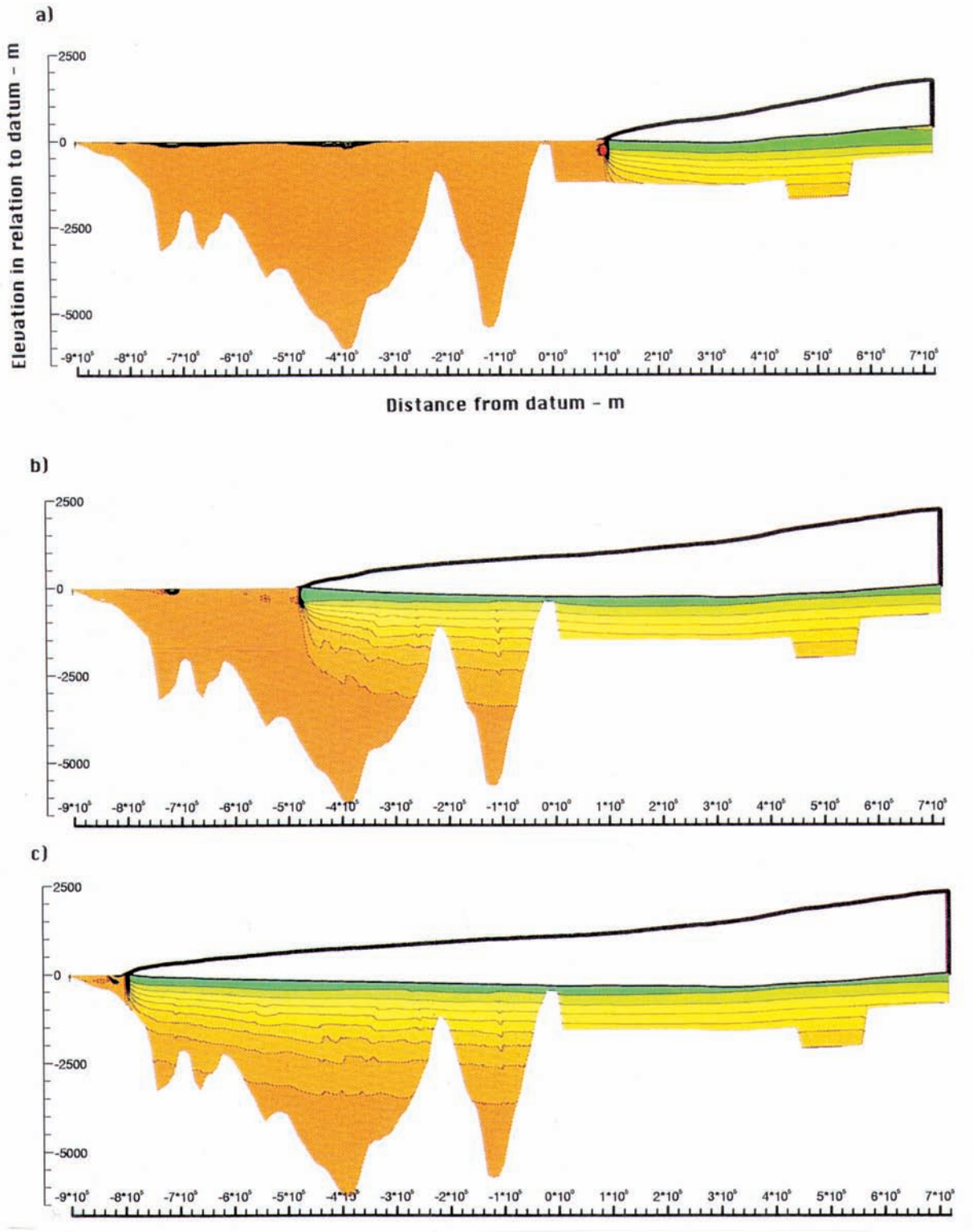

Figure 7-4 a-c. *Zones in which there will be a tendency to shear failure due to ice sheet loading for a modelled ice sheet extending along the transect into (a) southern Sweden; (b) the Warthe maximum position in northern Germany; and (c) the Saalian maximum (Drenthe) position in the southern Netherlands. Sub-surface rocks are modelled as frictional materials (sands) in which $\phi = 35^{o}$ and $C = 0$. Green colours are those in which the tendency to failure is greatest.*

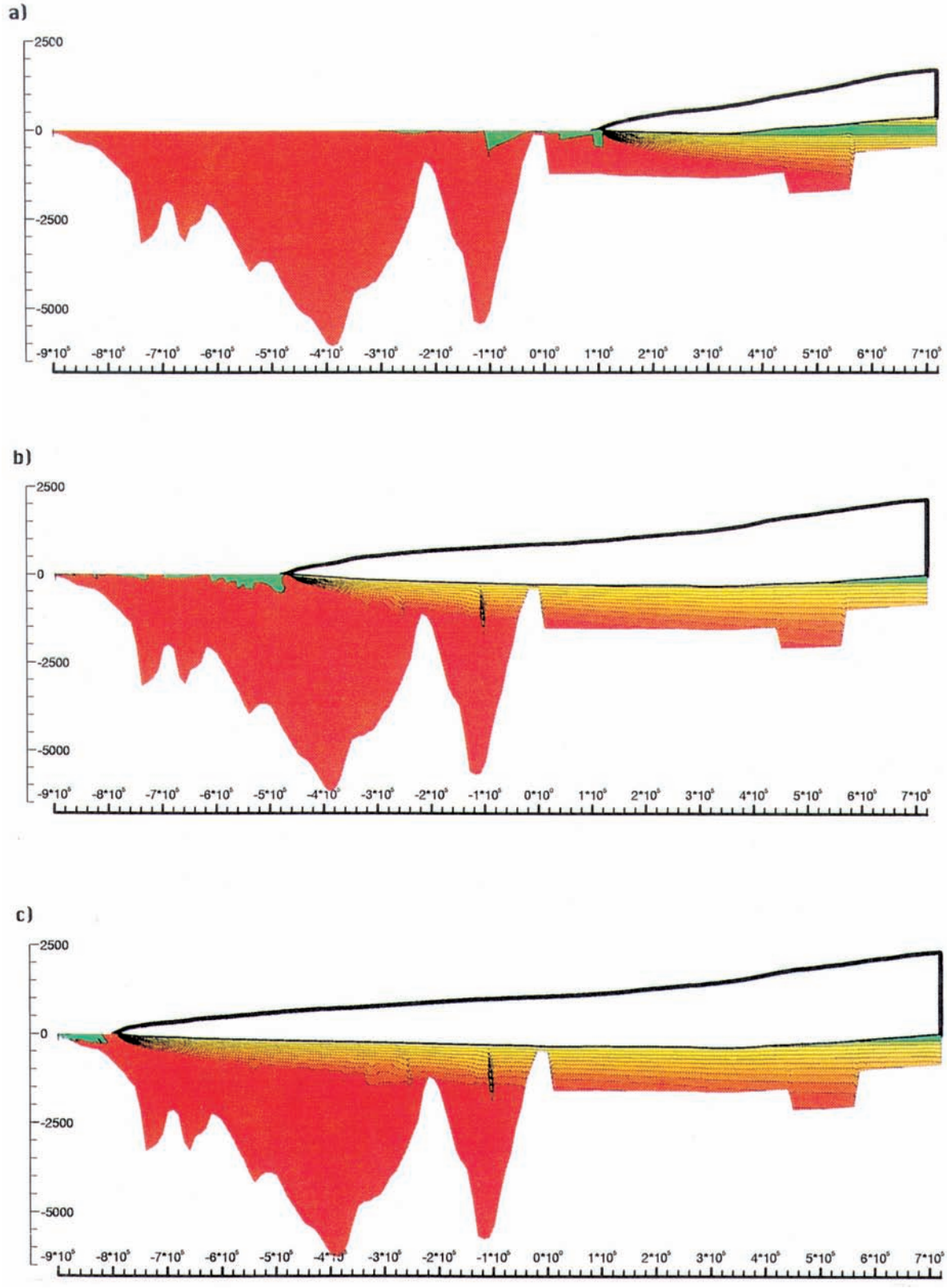

Figure 7-5 a-c. *As for Figure 7-4, but with a lithified rock bed in which the angle of friction, ϕ = 45° and the tensile strength, C = 20 MPa, values typical of intact granite. We conclude that failure of shield rocks is possible in the ice divide region of stagnant subglacial groundwater (see Figure 7-2b).*

The fact that shear trajectories pass from the zone of failure to the passive zone beyond does not necessarily mean, however, that extensive shear movement cannot occur. Along shear planes in the zone of failure, the stress is greater than the shear resistance. Along their continuations beyond the zone of failure, the reverse is true. If we add stresses along the shear trajectories to produce a total tractive force, and compare them to the total drag, we can estimate a safety factor $\left(\frac{\text{drag force}}{\text{tractive force}}\right)$. Failure occurs if the safety factor is less than 1.

In the case shown in Figure 7-1, a shear plane descending to –94 m at 798.8 km, has a safety factor of 1, and of less than 1 for all planes above it. 94 m is therefore the maximum depth to which long tectonic transport will occur along an extensive shear plane, and so to generate a gliding nappe. The sediments above the leading edge of the shear plane, where local conditions for failure are not satisfied, will be subject to a larger basal drag than those in the zone of failure. We therefore expect internal deformation to develop folds more readily in the nose area of the sliding nappe.

7.4 Hydrofracturing due to ice sheet loading

It has long been known that tensile fracturing of rocks can occur even when the overburden pressure is greater than the fluid pressure in the rock /e.g. Clark, 1949/. This occurs because stresses in rocks need not be geostatic. Tectonic forces, or forces due to irregular ground surface topography may be such as to ensure that, in a given plane, the maximum stress is greater than the minimum stress ($\sigma_1 > \sigma_3$). In these circumstances, it is found that even if the water pressure is less than σ_1 but greater than σ_3, tensile fractures tend to develop parallel to σ_1 and normal to σ_3. This is the process of hydrofracturing.

If fluid pressure just exceeds σ_3, it is generally supposed /e.g. Hubbert and Willis, 1957/ that an old rock with a long and complex stress history has a sufficient number of incipient fractures of varied orientation within it, that some are oriented normal to σ_3 and will open up. It implicitly assumes that a sufficiently large rock mass will have no tensile strength.

Whilst this may be true of most or many rock masses on a large scale, it may not be true of all and is not true of fine grained sediments, such as tills, which have been recently deposited in a glacial environment. In such cases, we assume that the water pressure must also exceed the tensile strength or cohesion of the rock or sediment.

The threshold at which open hydrofractures occur in materials with zero tensile strength is:

$$p_w \geq \sigma_3 \quad \text{or} \quad p_1 \leq 0 \tag{7.7}$$

or, in materials with tensile strength/cohesion (C):

$$\sigma_3 - p_w = -C \quad \text{or} \quad p_w \geq \sigma_3 + C \quad \text{or} \quad p' = -C \tag{7.8}$$

If we make the same assumption as Hubbert & Willis /1957/, the zones in which minimum stresses (σ_3) are tensile (Figures 7-2, 7-3) will be zones of hydrofracturing, in which tensile fractures will develop parallel to the axes of maximum stress shown in Figure 7-1. The orientation of these hydrofractures and the area within which they will occur is shown in Figure 7-1. They are almost vertical immediately beneath the glacier sole, apart from within the terminal km or so where they dip up-glacier. Even up-glacier of this zone they begin to dip up-glacier below 10–20 m below the glacier sole. Figure 7-1 shows hydrofracturing to a depth of up to 165 m below the glacier sole beneath the ice sheet margin. It is suggested that most hydrofracturing will preferentially occur subglacially, as a tensile minimum stress is associated with a compressive maximum stress, whilst beneath the proglacial zone, the maximum stress is also tensile.

Where continuous proglacial permafrost extends much further beyond the ice sheet than the 1.5 km shown in Figure 7-1, as in Figures 7-2 and 7-3, much larger groundwater potentials develop and models show a zone of vertical hydrofractures up to 250–400 m in thickness beneath the margin of the ice sheet, and horizontal hydrofractures beyond the margin. Where a gap occurs in the permafrost at the precise margin of the ice sheet, release of water pressure may inhibit hydrofracturing or produce vertical hydrofractures.

It should be noted, however, that the upper part of the zone of hydrofracturing in Figure 7-1 is frozen as permafrost. Rheological tests on permafrost /e.g. Vialov, 1965/ suggest instantaneous tensile strength values of between 200 and 2000 kPa. As this is well within the range of tensile stresses generated by water overpressuring (Figures 7-1, 7-3), we suggest that hydrofracturing of permafrost will occur in this case.

Hydrofractures can be generated because of potentials set up either by upward or downward movement of groundwater. In Figure 7-2, water pressures exceed the magnitude of the minimum stress for a distance of about 100 km from the ice sheet margin, primarily because of a very extensive proglacial permafrost sheet. Conditions for hydrofracturing are therefore met in this zone. However, in the outermost zone, hydrofracturing occurs either because of water overpressures beneath permafrost or, beyond permafrost or beneath holes in the permafrost, because an upward potential gradient between overpressured water at depth and the free surface. In the proximal zone, it occurs because of a downward gradient from a high pressure at the glacier sole and a lower pressure in underlying permeable beds. Two of these conditions are illustrated in Figures 7-6 and 7-7.

a) *Hydrofractures generated in a subglacial zone of downward groundwater flow (Figure 7-6a-b).*

   Figure 7-6 a shows an aquitard, such as a till, overlying a relatively permeable stratum. If it were not for the aquitard, the water pressure at the glacier sole would be lower than the minimum stress, and hydrofracturing would not occur. However, water draining downwards from the sole into the extensive permeable unit generates a large potential gradient in the aquitard, so that the water pressure at the ice/bed interface is larger than the minimum stress. Hydrofractures therefore develop downwards to a depth at which σ_3 begins to exceed the water pressure, and with an up-glacier dip as shown in Figure 7-1. If water pressures in the underlying permeable stratum were to increase from $p_w(2)$ to $p_w(3)$, thus driving water pressures up in the till, the depth of hydrofracturing would increase as shown in Figure 7-6a-b. Figure 7-6b shows how hydrofracturing develops in and adjacent to an aquitard which lies at some depth below the glacier sole.

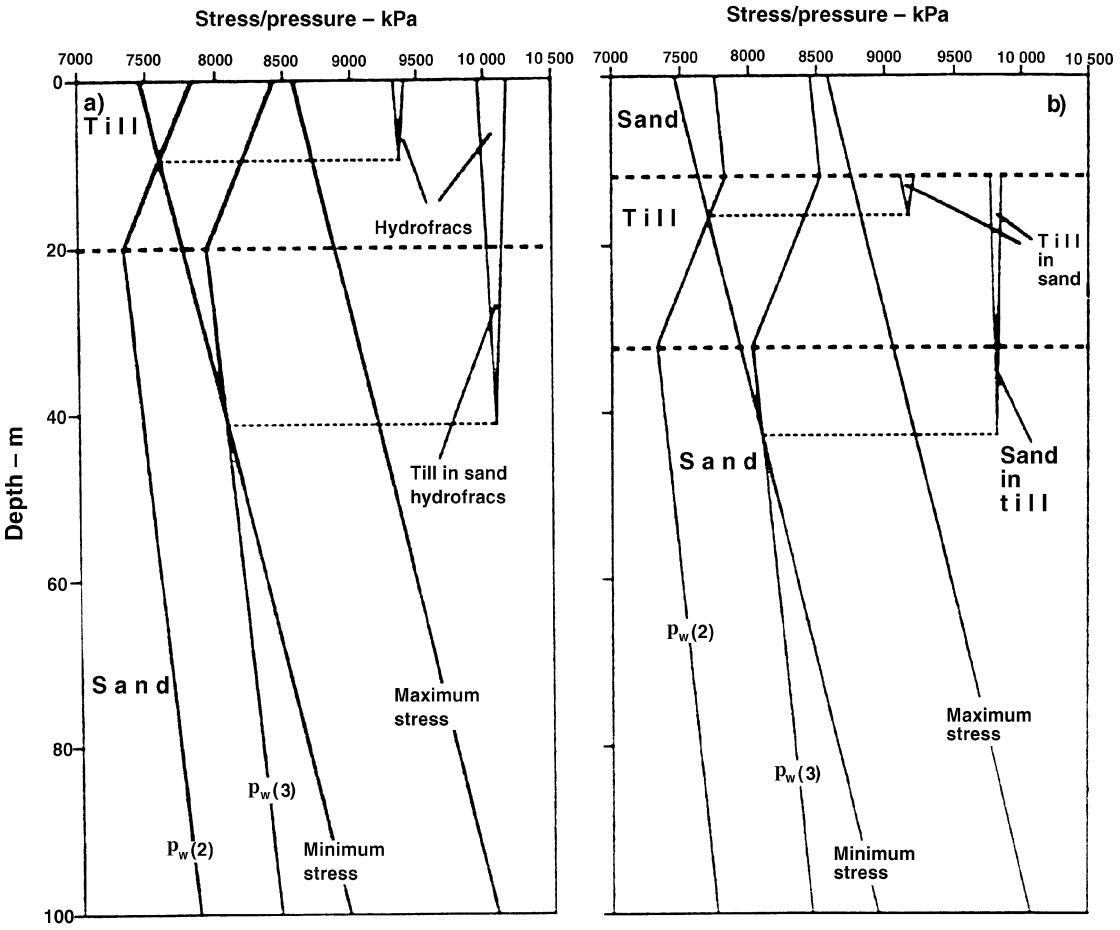

***Figure* 7-6.** *Conditions for hydrofracturing and associated liquifaction due to downward flow of basal meltwater through sub-glacial sediments. Hydrofracturing occurs when the water pressure (p_w) exceeds the minimum stress (σ_3). A sandy (or relatively permeable stratum) drains water relatively well, but large potential gradients through the till drive up water pressures so that in the case $p_w(2)$ (a) hydrofracturing occurs above -9 m. If the pressure in the relatively permeable bed is increased, hydrofracturing extends to -40 m and associated liquifaction results in injection of till into sand. In (b), a sandy horizon occurs above the till, resulting in injection of sand from above into till.*

b) Hydrofractures developed in a zone of upward groundwater flow (Figure 7-7c-d).

Figure 7-7c-d shows the consequences of upward groundwater flow in the proglacial zone of a glacier through the same stratigraphy as that in Figure 7-6a-b. If there were no aquitard, groundwater pressures would not exceed the minimum stress and there would be no hydrofracturing. The aquitard induces a large upward potential gradient through it, with the consequence that water pressures are driven up to exceed the minimum stress within the lower part of the aquitard and in the lower high permeability bed. Vertical hydrofractures will therefore develop in the zone within which water pressures exceed σ_3.

In both the above cases, the place of the low permeability stratum could be taken by subglacial or proglacial permafrost, in which hydrofractures could also be expected to develop. Hydrofractures beneath or within proglacial permafrost, will tend to be horizontal.

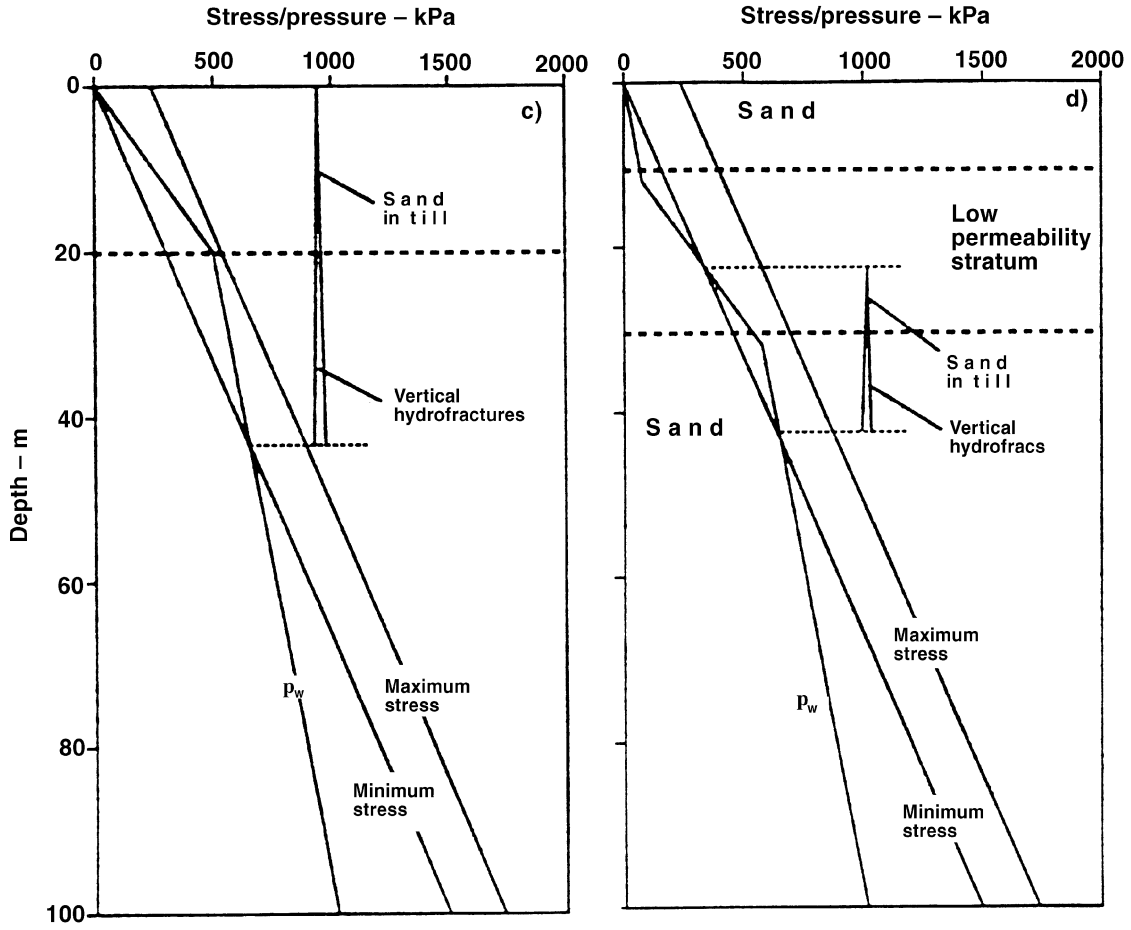

Figure 7-7. *Conditions for hydrofracturing and associated liquifaction during upward flow of meltwater in the marginal and proglacial zone. Hydrofracturing occurs when the water pressure (p_w) exceed the minimum stress (σ_3). Although beneath permafrost principal stresses are horizontal and produce horizontal hydrofractures, a strong vertical water pressure gradient where there are holes in permafrost or at the outer margins of permafrost cases vertical hydrofractures to develop along which upward sediment flow may occur.*

Patterns of fracturing which we would ascribe to hydrofracturing have been described from the Peelo Clays of the Netherlands by Schokking /1990/. The Peelo Clay is a homogeneous late Elsterian clay of very low permeability and a maximum thickness of about 100 m, which was overridden during the Saalian glaciation. Schokking described patterns of fractures from borehole cores which were vertical near to the top of the clay and took on a progressively shallower up-glacier dip with depth. He ascribed this pattern to subglacial shearing in the direction of ice flow. The clays show no signs of thin-skinned shear deformation and the pattern is unlike that which we expect from glacier loading (Figure 7-1). It is, however, very similar to that which would be produced by hydrofracturing (Figure 7-1).

It is common to find till and other sediments in fractures within bedrock, in a setting which suggests that they were injected subglacially. Pusch and others /1990/, for example, found both vertical and horizontal fractures in crystalline rocks at Forsmark in Sweden filled by surface-derived sediment to a depth of 30 m below surface. They

suggested that these were pre-existing fractures which had been opened hydraulically by glacially overpressured groundwater. Our model would suggest that pre-existing vertical fractures would tend to be opened by hydrofracturing subglacially (Figure 7-1), where σ_1 is predominantly vertical. They would be filled by forcing of overlying sediment into the vertical joints as a consequence of seepage forces generated by the downward potential gradients associated with infiltration of basal meltwater, a process which will be discussed in section 7.6. We suggest that as the glacier retreated, horizontal joints began to open under hydrofracturing conditions as σ_1 became horizontal (Figure 7-1). Sediment was injected along them to form the horizontal components of sediment filled fracture networks.

The results illustrated in Figures 7-1 and 7-2 show clearly how the existence of permafrost in the proglacial zone can help to generate excess fluid pressures and produce buoyant forces which will dilate intergranular voids and fractures and suck in water. A condition is created whereby hydraulic jacking can occur of rock or sediment blocks by dilation of horizontal joints so as to produce sediment filled joints in the way described from Sweden by Stephansson and Ericsson /1975/, Pusch et al /1990/ and Talbot /1990/.

7.5 Summary of subglacial failure / folding geometries

Figure 7-8 summarises the combinations of fracture orientations and associated fold styles which would be produced during a glacial cycle in relation to depth. Note that we have only included primary fractures and folds and not secondary fractures or folds developed as a consequence of secondary stresses produced by primary movement. Such systems of secondary fractures have been recently reviewed by Einstein and Dershowitz /1990/.

a) Glacier sole drag

The geological results of this process have been described in detail by Boulton /1987/. We expect flow folding to relatively shallow depths of up to a maximum of a few metres to be its principal effect. Small strains tend to be associated with overturned synclinal folds, with axial planes striking normal to glacier movement, often of conical form, and closing in an up-glacier direction. Larger strains produce fold attenuation and tectonic lamination, and extreme strain can produce homogenisation. Boulton /1987/ suggested that most lowland tills have this origin. Active deformation tends to be shallow, but the sediments can be depositionally stacked to greater thicknesses.

b) Shear fracture due to loading

As an ice sheet moves over a particular site, the fracture geometries illustrated in Figure 7-1 will be superimposed upon each other. However, in the case illustrated, it is only those failure planes which lie above a failure trajectory reaching its lowest point at 94 m at about 799 km (shaded) which will show large displacements. Others in the subglacial zone may show small displacements depending on compaction on the active side of the failure plane. Those planes lying beyond the zone of failure and beneath the shaded zone will not experience failure. In the 1–10 m range we expect steep, distally dipping fractures formed subglacially to be succeeded by shallower proximally dipping fractures formed proglacially. At greater depths (10–100 m), fracture dips decrease, whilst below 100 m in the case modelled, we only expect shallow distally dipping fractures.

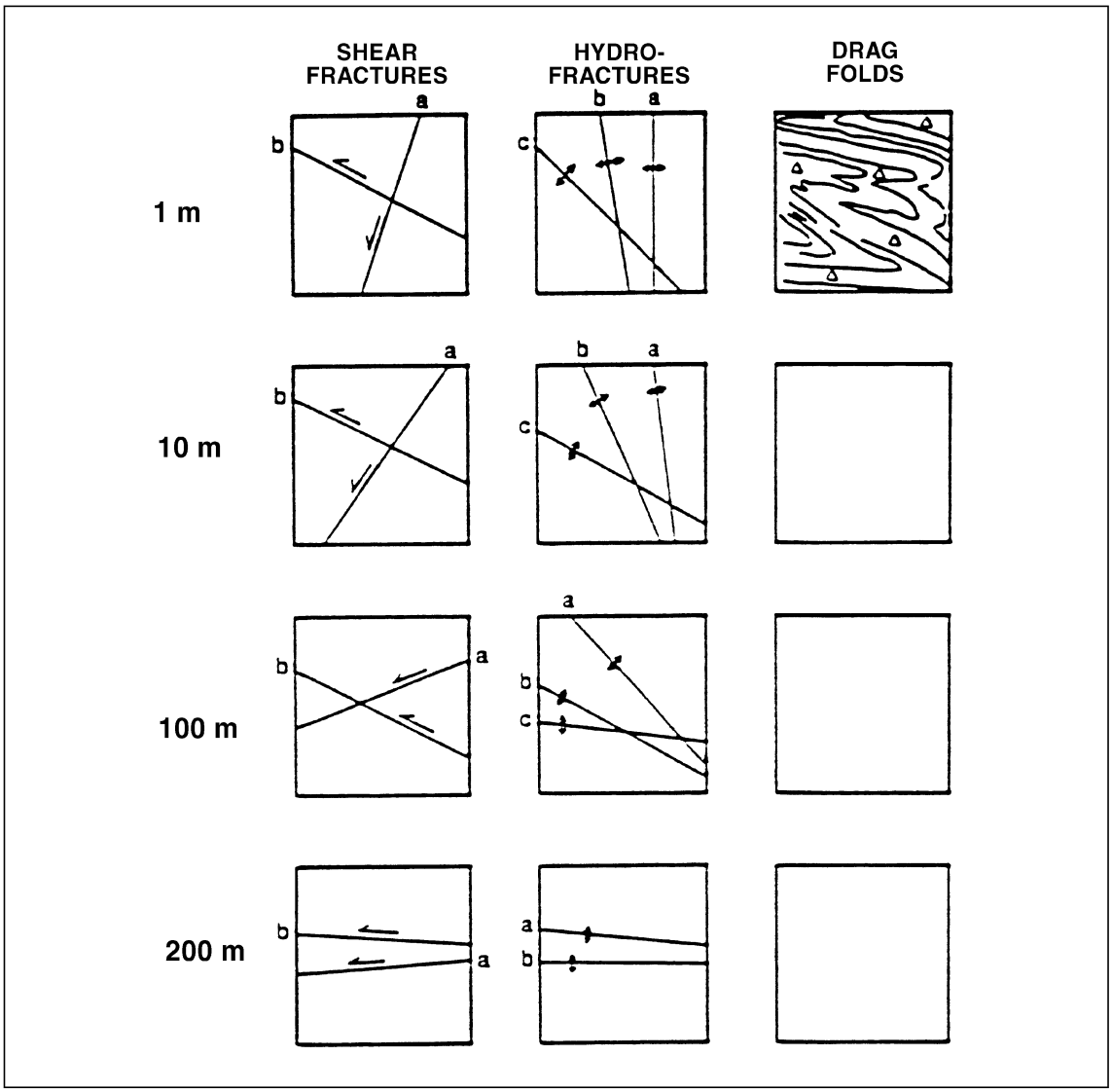

Figure 7-8. *Summary of the expected patterns of small scale failure generated during deglaciation at a given locality and at depths of 1 m, 10 m, 100 m and 150 m for the simulation shown in Figure 7-1. Shear fractures and hydrofractures from sub-glacial and proglacial environments are superimposed. a-b-c shows the time sequence. At a depth of 10 m for example, near vertical hydrofractures (a) are formed relatively far beneath the glacier, low angle fractures dipping up-glacier (b) form sub-glacially but near to the ice sheet margin, whilst relatively flat-lying fractures (c) form proglacially. These features may however be rotated as parts of large fold structures. Drag folding due to the movement of the glacier sole only occur at relatively shallow depths.*

c) Hydrofractures

At shallow depths between 1 and 10 m (Figures 7-1, 7-8), we would expect vertical hydrofractures developed in the subglacial zone to be superimposed by up-glacier dipping fractures formed in the marginal zone and horizontal hydrofractures generated in the proglacial zone. These tensile fractures will show a tendency to be filled by sediment mobilised by liquefaction at the up-pressure extremity of the fracture, and injected in the direction of the potential gradient. Beneath permafrost in the proglacial zone, hydraulic jacking of large bedrock masses along

pre-existing fractures may also lead to sediment injection by the same mechanism. With increasing depth, we expect the vertical fracture set to adopt a lower, up-glacier, inclination and for fractures to contain less surface-derived sediment. At 100 m we would expect low angle up-glacier dipping subglacial fractures to be overprinted by weak, horizontal, proglacial fractures. At 150 m we would, in this simulation, expect only horizontal fractures formed in the ice marginal zone.

Note that in this simulation, structures at depths down to about 100 m could be effected by large scale fold structures generated by forces due to ice loading.

7.6 Self organisation of permeability

Hydrofracturing occurs when groundwater pressures exceed the value of the minimum stress. High groundwater pressures occur when low permeabilities mobilise potential gradients in groundwater up to the magnitude of the limiting potential gradient set by the ice sheet surface /see Boulton, Caban and van Gijssel, 1995/. The tensile fractures produced by hydrofracturing increase the permeability of the rock or sediment and thereby reduce potential gradients and groundwater pressures. Hydrofracturing will therefore continue until increasing fracture permeability leads to a decrease in water pressure below the value of the minimum stress. It is therefore a transient process which acts to increase permeability to the point where water pressures are drawn down below the threshold for hydrofracturing.

Consider, for example, a case in which there is downward, subglacial water flow, in which the large potential gradients required to maintain the downward flow of meltwater through an aquitard drive up water pressures to exceed the minimum stress and thereby generate hydrofractures. If we assume a downward meltwater flow rate of 1–10 $cm.yr^{-1}$ ($0.33x10^{-9}$ to $0.33x10^{-8}$ $m.yr^{-1}$), a permeability of between 10^{-8} to 10^{-9} $m.yr^{-1}$ is required to avoid development of a significant potential build up in the stratum. If therefore the sediment were an unfractured clay with a nominal permeability of 10^{-11} to 10^{-12} m/sec, hydrofracturing would continue until the permeability increased by about three orders of magnitude.

We should not therefore regard permeability as an intrinsic property of the rock moderated by the load to which the rock is subject, but, in the glacial case, to be a largely externally determined property, a product of ice sheet thermodynamics and hydrogeological setting.

8 References

Ahlbom K, Andersson J-E, Nordqvist R, Ljunggren C, Tiren S, Voss C, 1991. Fjällveden study site. Scope of activities and main results. SKB TR 91-52.

Bear J, Verruit A, 1987. Modelling groundwater flow and pollution. D Reidel, Hingham, Massachusetts.

Berger A, Guiot J, Kukla G, Pestiaux P, 1981. Long term variations of monthly insolation as related to climate change. Geologischen Rundchau, Bd. 70 (2), 748–758.

Berger A, Loutre M F, 1991. Quaternary Science Reviews, 10(4), 297–318.

Birch F, 1966. Handbook of Physical Constants. Geol. Soc. Am. Mem. 97, 1966.

Boulton G S, 1987. A theory of drumlin formation by subglacial deformation. In: Drumlins: a Symposium. (Eds. Rose J and Menzies J) Balkema, Rotterdam.

Boulton G S, Hindmarsh R C A, 1987. Sediment deformation beneath glaciers: rheology and geological consequences. J. Geophys. Res., 92, 9059–82.

Boulton G S, Caban P E, 1995. Groundwater flow beneath ice sheets: Part II – Its impact on glacier tectonic structures and moraine formation. Quaternary Science Reviews 14, 563–587.

Boulton G S, Caban P, Punkari M, 1995. Sub-surface conditions produced by climatic change, including glaciation: sensitivity and model tests. SKB AR 95–42.

Boulton G S, Caban P E, van Gijssel K, 1995. Groundwater flow beneath ice sheets: Part I – Large scale patterns. Quaternary Science Reviews 14, 545–652.

Boulton G S, Dobbie K E, 1993. Consolidation of sediments by glaciers: relations between sediment geotechnics, soft-bed glacier dynamics and subglacial groundwater flow. J. Glaciol., 39, 26–44.

Boulton G S, Hulton N, Vautravers M, 1995. Ice sheet models as tools for palaeoclimatic analysis – the example of the European ice sheet through the last glacial cycle. Ann. Glaciol.

Boulton G S, Payne A, 1992a. Simulation of the European ice sheet through the last glacial cycle and prediction of future glaciation. SKB TR 93-14, 1–38.

Boulton G S, Payne A, 1992b. Reconstructing past and predicting future regional components of global change: the case of glaciation in Europe. In: Waste Disposal and Geology. International Geological Congress Proceedings Workshop 21, Tokyo. 51–134.

Boulton G S, Payne A, 1994. Northern hemisphere ice sheets through the last glacial cycle: glaciological and geological reconstructions. In: Duplessy, J-C. ed. Long term climatic change: data and modelling. Nato ASI Series, 122. Springer-Verlag, Stuttgart, 177–212.

Boulton G S, Slot T, Blessing K, Glasbergen P, Leijnse T, van Gijssel K, 1993. Deep circulation of groundwater in overpressured subglacial aquifers and its geological consequences. Quat. Sci. Revs., 12, 739–745.

Boulton G S, Smith G D, Morland L W, 1984. The reconstruction of former ice sheets and their mass balance characteristics using a non-linearly viscous flow model. J. Glaciol. 30 (105), 140–152.

Clark J B, 1949. A hydraulic process for increasing the productivity of wells. Transactions of the American Institute of Mechanical Engineers, 186, 1–8.

Coope G R, 1977. Fossil Coleoptera as sensitive indicators of climatic change during the Devensian cold stage. Philos. Trans. R. Soc. London, Ser. B, 280, 313–340.

de Beaulieu J L, Guiot J, Reille M, 1991. Long European pollen records and quantitative reconstructions of the last glacial cycle. In: Goodess and Palutikof (eds.), Future Climate Change and Radioactive Waste Disposal, NIREX NSS/R257, 116–136.

Einstein H H, Dershowitz W S, 1990. Tensile and shear fracturing in predominantly compressive stress fields. Engineering Geology, 29, 249–172.

Frenzel B, Pesci M, Velichko A A, 1992. Palaeoenvironments of the Northern Hemisphere. Fischer Verlag, Stuttgart.

Glasbergen P, 1990. The interaction between diapirism, caprock growth and salt solution in The Netherlands as an example of a sedimentary basin. Proceedings of the Geological Survey of Iran, 191–210.

Guiot J, 1990. Methodology of the last climatic cycle reconstruction in France from pollen data. Palaeogeography, Palaeoclimatology, Palaeoecology, 80, 49–69.

Guiot J, Reille M, de Beaulieu J L, Pons A, 1992. Calibration of the climate signal in a new pollen sequence from La Grande Pile. Climate Dynamics 6, 259–264.

Guiot J, Pons A, de Beaulieu J L, Reille M, 1989. A 140,000 yr climatic reconstruction from two European pollen records. Nature 338, 309–311.

Gustafson G, Liedholm M, Lindbom B, Lundblad K, 1989. Groundwater flow calculations on a regional scale at the Swedish Hard Rock Laboratory. SKB PR HRL 25-88-17.

Hassanizadeh S M, Gray W G, 1980. General constitutive equations for multi-phase systems: constitutive theory for porous media flow. In: Pinder, G.F. (ed.) Flow Through Porous Media. CML Publications, Southampton, 17–29.

Hubbert M K, Willis D G, 1957. Mechanics of hydraulic fracturing. Petroleum Transactions of the American Institute of Mechanical Engineers, 210, 153–169.

Imbrie J, Hays J D, Martinson D G, McIntyre A, Mix A C, Morley J J, Pisias M G, Prell W L, Shackleton N J, 1984. The orbital theory of Pleistocene climate: Support from a revised chronology of the marine $\delta^{18}O$ record. Berger A L et al Eds., Milankovitch and Climate, Part 1, 269–305. Reidel Publishing Company.

Kukla G, Berger A, Lotti R, Brown J P, 1981. Orbital signature of interglacials. Nature, 290(5804), 295–300.

Labeyrie L D, Duplessy J C, Blanc P L, 1987. Variations in mode of formation and temperature of oceanic deep waters over the past 125,000 years, Nature, 327, 447–482.

Mangerud J, 1991. The Scandinavian ice sheet through the last interglacial/glacial cycle. In: Frenzel, B. (ed.). Klimageschichtliche, Probleme der Letzten 130,000 Jahre. G Fisher, Stuttgart, 307–330.

Mörner N-A, 1980. A 10,700 years' palaeotemperature record from Götland and the Pleistocene/Holocene boundary events in Sweden. Boreas 9, 283–287.

Orvig S (ed.), 1970. Climates of the polar region. Amsterdam, Elsevier. (World Survey of Climatology, Vol. 14).

Paterson W S B, 1984. The Physics of Glaciers. Pergamon Press.

Prell W L, 1985. The stability of low-latitude sea-surface temperatures: an evaluation of the CLIMAP reconstruction with emphasis on the positive SST anomalies, Rep. TR 025, U.S. Department of Energy, Washington.

Pusch R, Börgesson L, Knutsson S, 1990. Origin of silty fracture fillings in crystalline bedrock. Geologiska Föreningens i Stockholm Förhandlingar, 112, 209–213.

Rotnicki K, 1976. The theoretical basis for and a model of the origin of glaciotectonic deformations. Quaestiones Geographicae, 3, 103–139.

Sauter F J, Hassanizadeh S M, Leijnse A, Glasbergen P, Slot A F M, 1990. Metropol: A computer code for the simulation of contaminants with groundwater. Report of the European Communities, EUR 13073 EN, Luxembourg.

Schokking F, 1990. A sub-glacial sediment deformation model from geotechnical and structural properties of an over consolidated lacustro-glacial clay. Geologie en Mijnbouw, 69, 291–304.

Seret G, Guiot J, Wansard G, de Beaulieu J L, Reille M, 1992. Tentative palaeoclimate reconstruction lining pollen and sedimentology in La Grande Pile (Vosges, France). Quat. Sci. Rev., 11 (4), 425–430.

Smellie J, Laaksoharju M, 1992. The Äspö hard rock laboratory: final evaluation of the hydrogeochemical pre-investigations in relation to existing geologic and hydraulic conditions. SKB TR 92-31, 239 pp.

Stephansson O, Ericsson B, 1975. Pre-Holocene joint fillings at Forsmark, Uppland, Sweden. Geologiska Föreningens i Stockholm Förhandlingar, 97, 91–95.

Talbot C J, 1990. Problems posed to a bedrock radwaste repository by gently dipping fracture zones. Geologiska Föreningens i Stockholm Förhandlingar, 112, 355–359.

Vialov S S, 1965. Rheology of frozen soils. In: Permafrost. Proceedings of an international conference, National Academy of Sciences, Washington, National Research Council of Canada, 332–337.

Wallroth T, Gustafson G, 1993. Sub-surface conditions produced by future climate changes, including glaciations: data support for modelling. SKB AR 92-77.

West R G, 1988. The record of the cold stages. Phil. Trans. R. Soc. Lond. B318, 409–688.

Wikberg P, Gustafson G, Rhen I, Stanfors R 1991. Äspö Hard Rock Laboratory. Evaluation and conceptual modelling based on the pre-investigations 1986–1990. SKB TR 91-22.

Appendix I

The computer model

The model is written in Fortran and consists of a suite of subroutines which can be compiled and linked with a UNIX makefile. We have used this particular model only on UNIX workstations, but it could be moderately easily ported to other platforms. The code has substantial dependencies between subroutines so the task of substituting routines is not straightforward. The input data are converted for calculation purposes in different subroutines which also makes debugging and tracing potentially hazardous. The code is poorly commented so far but we are in the process of making some upgrades to address this problem. Largely speaking a user would not have to alter substantial parts of the code unless they wanted to make significant changes to the ice dynamics solution method or put in a different climate drive. In essence, after initialisation routines are called, the program loops through a single time loop, performing one calculation iteration per time step with checks to see if output data need to be written. The model is run by typing 'budd' at the command line, but can be run in background of batch modes. Care needs to be taken that the correct files paths are specified. The model runs until the desired time stop is reached or if it exceeds its specified 'grow-to' size. Occasionally the model will produce a numerical instability which will halt processing.

Input and output files

Input files are in three forms:

a) *Distance-quantity files*. These have two formatted records. The first record lists the distances along the flowline at which each quantity is held. The second record specifies the values of the quantity at each point. These files are used to specify the basal elevations, the relaxed bedrock elevations and the ELA heights along the flowline. Each field is a 6 character integer followed by a comma.

b) *Time series files.* These files are used to drive the model through time. They have as many records that there are discrete model driving periods. In each record the first value is the model time in years and the second value is the value that will apply to the model at that time. They are used to specify the ELA and temperature deviations that will apply through the model run.

c) *Parameter files.* These contain a listing of all the parameters to both run the file and control the nature of the run sequence and the output files. They have the name 'FLOWLINE'.

An example listing is shown later in this appendix.

There are two important output files:

a) 's' files: These contain output for the whole ice sheet – usually volume, area, total melt rate plus others selected. They contain one formatted record for each time series output. The first record is a title header for the rest of the data. The first field in each record is the model time, followed by volume and area. These are comma-separated variable fields (CSV).

b) 'x' files: These contain cross sectional information for the whole ice sheet. Usually they contain the basal elevation and ice thickness at each grid cell, but they frequently also contain the temperature at each altitude plus basal temperature and melt rates. These files can become quite large. One set of records is written for each predefined time period in the 'budd.p' input file. The first record gives a list of the distances that the subsequent values are located. Subsequent records list a code describing the variable being recorded, the time for that variable, and, if relevant, the vertical level in the ice sheet that it is for. These are comma-separated variable files (CSV).

Sample input TO FLOWLINE file

The right-hand comments explain the function of the input fields.

This file contains the parameters etc. needed to run the FLOWLINE model.
The format of data is as follows –
parameters description (including keywords and units) = parameter value
*** all parameters are real

——> numbers of things in file

---

number of parameters = 36.0
number of names = 12.0

——> names of files temp5.dat

---

name of initial topography file = ../../data/xs5_topx.dat
name of mass initial balance topography file = none
name of relaxed topography file = ../../data/xs5_topx.dat — *This defines the relaxed topography for the isostatic adjustment*
name of aquifer depth file = none
name of aquifer conduct file = none — *These files are presently unused*
name of aquifer storage file = none
name of ela file = ../../data/xs4_elax.dat — *This gives ELA along the transect*
name of ela forcing time file = ../../data/f3_ela.dat — *This is the time-forcing of the ELA's*
name of air temperature time file = ../../data/f3_tmp10.dat — *This is the time-forcing of temperature*
name of initialization file = none — *This allows a model 'hot start from a previous 'dump'*
name of data dump file = none
root name for output files = flj0001 — *This defines files output name parts*
eg scn0000 – first 3 letters for area, then 4 alphanumeric for run

---

——> basic run controls

---

model start time in years = 0.0

model end time in years = 117000.0

interval between time-series output = 500.0 *How frequent records in the 's' files*

model time step in years = 10.0 *are dropped*

model grid spacing in m = 20000.0

run to stop at size in km = 1700.0

sea level difference (fall is -ve) = 0.0

——> times for output of thickness and topography

---

drop at time in years = 0.0 *When 'x' files are to be dropped*

drop at time in years = 1000.0

drop at time in years = 2000.0

drop at time in years = 3000.0

drop at time in years = 4000.0

drop at time in years = 5000.0

——> points for time-series output, format location = ew_pt ns_pt

---

output at location = 60.0

——> variables to be output (H,h,u,w,q,b,T,t,S,D,G,d,r,o)

---

time series output variables = H

gridded output variables = H h s

——> physical constants for isostasy 400.0 1.0e8

---

diffusivity of asthenosphere in square m per year = 0.1e8 *This changes asthenospheric viscosity*

density of mantle in kg per cubic m = 3300.0

thermal conductivity of rock in J per m K year = 1.041e8

bedrock temperature step size in m = 0.0

sea water temperature in degrees C = 0.0

specific heat capacity rock in J per kg K = 1000.0

——> physical constants for ice shelves

---

density of water in kg per cubic m = 1000.0

density of seawater in kg per cubic m = 1028.0

bathymetric limit m = -500.0

——> physical constants for ice flow 3.0e-24

---

flow law multiplier in Pa ** -n per s = 4.60e-23

flow law exponential = 3.0

acceleration due to gravity in m per s ** 2 = 9.81

density of ice in kg per cubic m = 910.0

gas constant in J per mol per K = 8.314

activation energy high in J per mol = 60.0e3

activation energy low in J per mol = 139.0e3

arrhenius multiplier high in Pa ** -n per s = 7.230e-12

arrhenius multiplier low in Pa ** -n per s = 3.469e4

——> physical constants for thermodynamics 6.62e7 1.0e-3

---

thermal conductivity of ice in J per m K year = 6.62e7

specific heat capacity ice in J per kg K = 2009.0

latent heat capacity of ice in J per kg = 3.35e5

geothermal heat flux in W per m ** 2 = 4.2e-2

pressure melting factor in K per Pa = 9.8e-8

roughness m ** 3 per N yr = 2.5e-3 *This alters the sliding rate*

——> parameters for environment 0.69

---

temperature / isotope multiplier in ppt per degree C = 0.69

temperature / isotope intercept in ppt = -13.6

mass balance multiplier = 1.0

lapse rate in degrees C per m = 0.010

sea level air temperature in degrees C = -5.0

——> end of file

Data visualisation and hardcopy

The CSV files can be read directly into EXCEL for preliminary investigation of the model output, though the change of computer platforms makes this awkward. We have a limited suite of program based around UNIRAS which tackle some of the mode complex data visualisation and hardcopy production. The two most important of these are CROSS which draws up cross sectional data and TIMESER which plots time-space diagrams of the cross sectional data. However, these need to be recompiled should the model domain size or run period be altered.

Appendix II

1. Stress axes in two-dimensions

For any planar stress tensor, the state of stress at a point is completely described by three stress components, the two normal stresses, σ_{xx} and σ_{zz}, and the shear stress σ_{xz} (by convention, these are normally given in the cartesian plane).

The principal stress axes can be defined as a pair of perpendicular axes along which there is no shear stress, i.e.:

$$\sigma_{xz} = 0 \tag{II.1}$$

at an angle ß to the x-axis, which satisfies

$$\tan(2\beta) = \frac{2\sigma_{xz}}{\sigma_{xx}-\sigma_{zz}} \tag{II.2}$$

with the value of the two normal stresses to these planes, σ_1 and σ_3 given by

$$\begin{aligned}\sigma_1 &= \frac{\sigma_{xx}+\sigma_{zz}}{2} + \left\{\frac{(\sigma_{xx}-\sigma_{zz})^2}{4} + \sigma_{xz}^2\right\}^{\frac{1}{2}} \\ \sigma_3 &= \frac{\sigma_{xx}+\sigma_{zz}}{2} + \left\{\frac{(\sigma_{xx}-\sigma_{zz})^2}{4} + \sigma_{xz}^2\right\}^{\frac{1}{2}}\end{aligned} \tag{II.3}$$

Knowing the magnitude of the principal stresses, and direction of the principal stress axes, the stress tensor along any plane inclined at an angle γ to the principal stress axes can be defined by

$$\begin{aligned}\sigma_{xx} &= \frac{\sigma_1+\sigma_2}{2} + \frac{(\sigma_1-\sigma_2)}{2}\cos(2\gamma) \\ \sigma_{xz} &= -\frac{\sigma_1-\sigma_2}{2}\sin(2\gamma)\end{aligned} \tag{II.4}$$

2. Definition of stress components

The total gravitational stress, or overburden, σ_T at a depth z, is defined by

$$\begin{aligned}\sigma_{T,\,ii} &= \rho_{ice} + \rho_{self\ weight} \\ &= \rho_{ice} g h_{ice} + \int_{z=0}^{z} [n\rho_{water} + (1-n)\rho_{soil}] g \, dz \\ \sigma_{T,ii} &= 0 \qquad i \neq j\end{aligned} \tag{II.5}$$

where n is porosity, and ρ is density.

The pore water pressure, p, at a depth, z, is defined by

$$\rho = \rho_{\Psi} + \rho_{\text{self weight}} = [\rho_w g\phi + [(1-n)\rho_w]gz] \quad \text{(II.6)}$$

where Ψ is the head.

The effective stress, $\sigma'_{g,ij}$ is the difference these two stress components

$$\sigma'_{g,ij} = \sigma_{T,ij} - p\delta_{ij} \quad \text{(II.7)}$$

where δ_{ij} is the Kronecker delta.

The effective stress, σ', includes the contributions from concentrated loading stresses (σ_{cl}) and tectonic stress and is given by

$$\sigma'_{ij} = \sigma'_{g,ij} + \sigma_{tec,ij} + \sigma_{cl,ij} \quad \text{(II.8)}$$

In practice, tectonic and gravitational stresses cannot be distinguished. In applications we assume a known background tectonic stress or no such background stress.

For any stress tensor, the deviator, D, is given by

$$D_{ij} = \sigma_{ij} - \frac{1}{3}\sigma_{kk}\delta_{ij} \quad \text{(II.9)}$$

and represents differences from the background, pressure dependent stress field.

3. Boussinesq theory of concentrated loading

The state of stress in any elastic, deformable body must satisfy the three equilibrium equations, expressed here in cartesian co-ordinates:

$$\frac{\delta\sigma_{ij}}{\delta x_j} = F_i \quad \text{(II.10)}$$

where σ_{ij} is a stress component, F_i is an inertial or body force and the summation convention applies over repeated indices.

The principle of superposition of stress allows the problem of self-weight of the earth to be solved separately. Hence, removing body forces and making the assumption that inertial effects are negligible, reduces equation (II.10) to

$$\frac{\delta\sigma_{ij}}{\delta x_j} = 0 \qquad \text{(II.11)}$$

For consistency and continuity within the body, the equations of compatibility must also be satisfied

$$\varepsilon_{ij}\ \frac{1}{2}\left[\frac{\delta u_i}{\delta x_j} + \frac{\delta u_j}{\delta x_i}\right] \qquad \text{(II.12)}$$
$$\varpi_{ij}\ \frac{1}{2}\left[\frac{\delta u_i}{\delta x_j} + \frac{\delta u_j}{\delta x_i}\right]$$

where ε is a strain component, ϖ is a whole body rotation and u a displacement.

Assuming plane strain in the out-of-plane (y direction), and recasting into plane polar co-ordinates, the nine equations in equations (II.11) and (II.12) can be reduced to (in expanded form)

$$\frac{\delta\sigma_r}{\delta r} + \frac{1}{r}\frac{\delta\sigma_{r\theta}}{\delta\theta} + \frac{\sigma_r - \sigma_\theta}{r} = 0$$

$$\frac{1}{r}\frac{\delta\sigma_\theta}{\delta\theta} + \frac{\delta\sigma_{r\theta}}{\delta r} + \frac{2\sigma_{r\theta}}{r} = 0 \qquad \text{(II.13)}$$

$$\left(\frac{\delta^2}{\delta r^2} + \frac{1}{r}\frac{\delta}{\delta} + \frac{1}{r^2}\frac{\delta^2}{\delta\theta^2}\right)(\sigma_r - \sigma_\theta) = 0$$

where r is the distance from the point of application of the load and θ is the angle between the line through which the load is applied and the point. For the particular application of surface load of magnitude P per unit width to the surface of a half-space, the stress distribution (from equation II.10) is given by

$$\sigma_{r\theta} = \frac{2P}{\pi r}\cos(\theta)$$
$$\sigma_{r\theta} = 0 \qquad \text{(II.14)}$$
$$\sigma_{r\theta} = 0$$

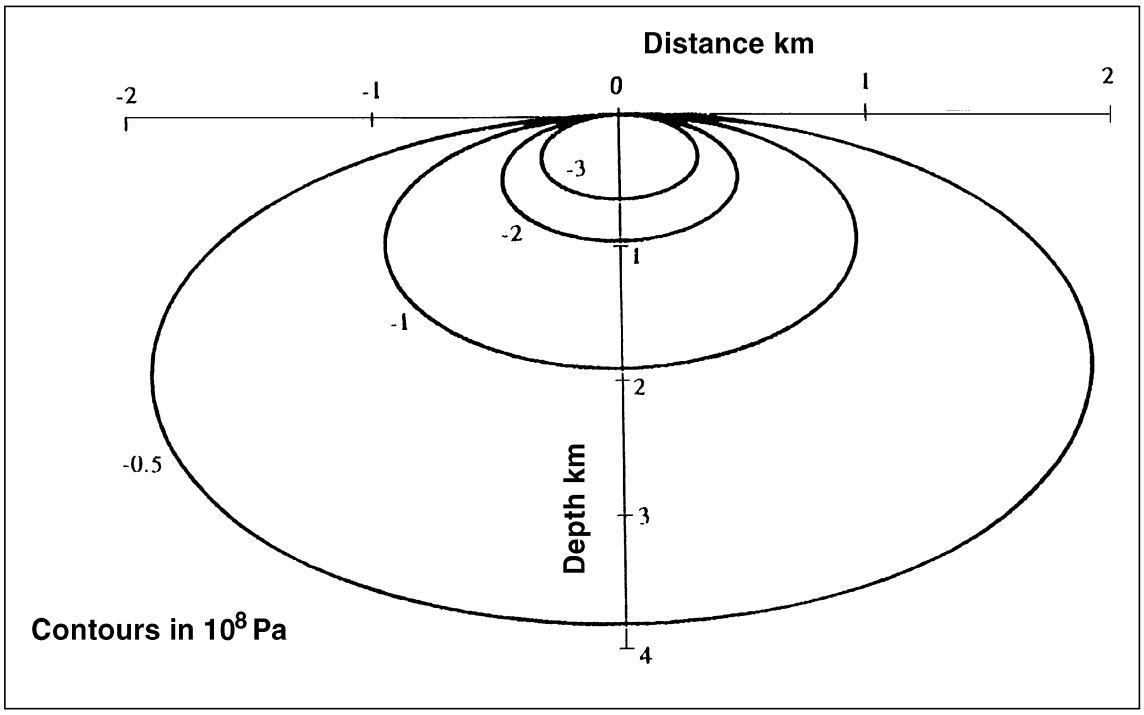

Figure II-1. *Radial stress magnitude distribution in relation to the point of application of a point load (at 0).*

The stress distribution is purely radial. Stress contours are sets of circles touching the surface at the point of application of the load. This is illustrated in Figure II-1 for a point load of $3x10^{11}$ Nm^{-1}, the approximate point load equivalent to a block of ice 10 km wide and 3 km high. It can be seen from the Figure (and equation II.13) that the magnitude of the stress falls away with increasing distance, and hence it is likely that the importance of the concentrated load relative to other stress sources will quickly become trivial away from the loading point. For example, the overburden stress at 4 km depth is of comparable magnitude to concentrated loading stress, and with increasing depth, the overburden quickly becomes the dominant component of the effective stress field.

It should be noted that the magnitude of the radial stress component is indeterminate at the point of load. Mathematically, the solution to the governing differential equations are violated when both r and q are both zero. Moreover, it is likely that inelastic deformation will dominate elastic deformation in the vicinity of the load, and hence the governing equations are not valid.

Using the principle of axes rotation, the cartesian stress co-ordinates for this problem are given by

$$\sigma_{xx} = \frac{2P}{\pi} \frac{z^3}{(x^2 + z^2)}$$

$$\sigma_{xz} = \frac{2P}{\pi} \frac{xz^2}{(x^2 + z^2)} \qquad \text{(II.15)}$$

$$\sigma_{zz} = \frac{2P}{\pi} \frac{x^2 z}{(x^2 + z^2)}$$

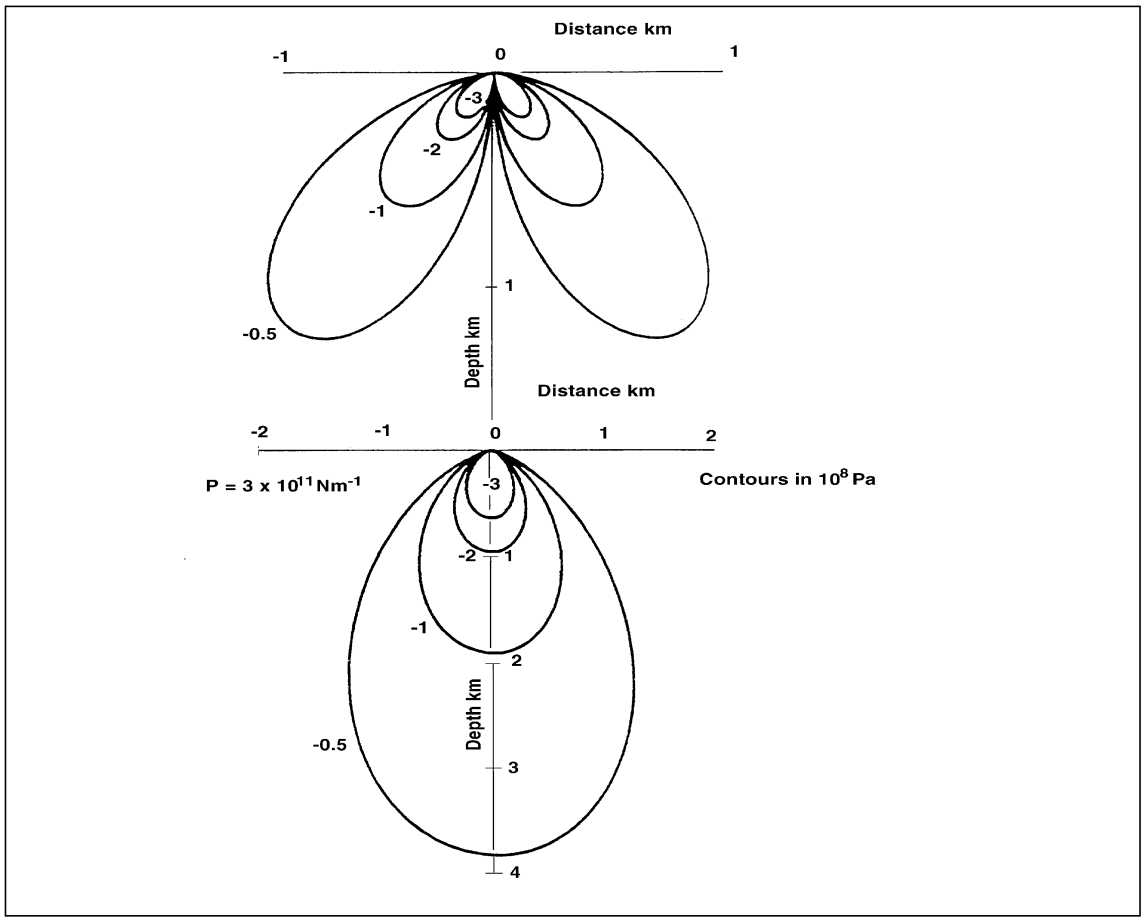

Figure II-2. *The σ_{xx} and σ_{zz} stress components in relation to the point load shown in Fig. II-1.*

The σ_{xx} and σ_{zz} stress components are plotted in Figure II-2 for the same load as in Figure II-1. The vertical normal stress is greater in magnitude immediately beneath the load, although laterally it is the horizontal normal stress which is greater. The shear stress is also zero directly beneath the point of load, and changes sign as the load axis is crossed.

Applying the principle of superposition of stress, stress distributions for some special cases of distributed two-dimensional line loads may be found by integrating the appropriate results of equation (II.12). For more complicated or irregular loads, however, numerical techniques must be employed to evaluate the concentrated loading stress distributions.

4. Application of Boussinesq theory to discretised problems

The application of Boussinesq theory to numerical problems requires a careful use of discretisation methods. In order to effect the integration correctly, care must be taken that the discretisation interval is appropriate to ensure that the very short range of the concentrated loading stresses is accounted for. Rather than solve the problem using the fast Fourier transform method, we have used a convolution summation

$$R(x,z) = \Sigma\, f(x,z-\zeta)\, g(\xi)\delta\zeta \qquad \text{(II.16)}$$

where R is the response, f is the response of the applied line load and g is the magnitude of the line load and ζ is the convolution variable.

The method copes easily with irregular grids, allowing the same grid to be used for both loading stress calculations and groundwater modelling. Its principal disadvantage is that it is more time consuming and computationally inefficient than a fast Fourier transform method. The finite-element grid used for the groundwater model does not lend itself to concentrated loading problems. The difference in grid node spacing between the x-direction (10 km) and z-direction (on average about 500 m, but a minimum of <100 m), makes it hard to achieve consistency for the stress distribution throughout the grid domain. The x-direction resolution is inadequate for accurate modelling of a distributed load as a series of discrete loads. It was therefore found necessary to subdivide each line load into twenty smaller loads, whilst still performing the convolution on the groundwater grid in order to improve accuracy.